UNIVERSITÀ
DEGLI STUDI
DI PADOVA

Università degli Studi di Padova

Dipartimento di Ingegneria Industriale

SCUOLA DI DOTTORATO DI RICERCA IN
SCIENZA E INGEGNERIA DEI MATERIALI
CICLO XXVIII

Tesi di Dottorato

GAS SENSING PROPERTIES OF CARBON NANOSTRUCTURES

‘

Direttore della Scuola : Ch.mo Prof. Gaetano Granozzi

Supervisore :Ch.mo Prof. Alessandro Martucci

Dottorando : Marco Angiola

Abstract

This work is aimed to evaluate the optical gas sensing properties of carbon nanomaterial. In particular it is focused on two materials, Carbon Nanotubes (CNTs) and Graphene Oxide (GO).

The comprehension of the mechanisms of interaction of these materials with the gas molecules is fundamental for a future application of these materials as sensors targeted to a specific specie or capable to distinctly detect several dangerous species. On this purpose nanostructures based on GO and CNTs have been produced and tested as optical gas sensors toward oxidizing/reducing gases (H_2, CO, NO_2) and aromatic volatile Organic Compounds (benzene, toluene, xylene).

Gold nanoparticles (Au NPs) have been used as optical probe thanks to the peculiar Localized Surface Plasmon Resonance feature in the visible range, which is extremely sensitive to the variation in optoelectronic properties of the surrounding media, such as refractive index and the variation in charge carrier involved in plasmonic excitation in the Au NPs.

Not only amplify the Au NPs the variation in optoelectronic properties of the layer of carbon nanomaterial, but also the electromagnetic coupling with carbon nanomaterials may induce an enhancement in response and a lowering of the limit of detection of the sensors to the target species.

Moreover, the GO and CNTs are provided of a large possibility of functionalization, which can be used to tailor the gas sensing properties of the nanostructures toward specific species.

CNTs have been combined with the Au NPs, Pd NPs, Ni NPs and fullerenes. Pd and Au NPs increase the response toward H_2, meanwhile Ni NPs and fullerenes appear specific to CO. It is also suggested the opportunity to monitor the features of the absorbance plot of fullerenes and CNT in the NIR as optical probes, with the carbon nanomaterials playing both the role of sensing element and optical probe.

The presence of the different functional groups in GO was investigated. The increase in sp^2 conjugation has a profitable effect for the sensing of H_2. Instead, the removal of the oxidized functional groups hinder the response of the films toward CO and NO_2.

The reduction and functionalization of the GO with para- Phenylene Diamine induces the detection of NH_3 without Au NPs as optical probe.

The sensors produced are characterized by high transparency in the visible range and may be incorporated as non-invasive sensors on transparent surfaces.

Most of the sensors worked at 150°C and 300°C. Test of gas sensing have been conducted at low temperatures, at 80°C for CNTs in fullerene matrix and good results were achieved. The possibility of sensors active at room temperature is suggested by the positive tests conducted with CMG, paving the way for future developments in active optical material sensitive to gases at room temperature.

Abstract

Il presente lavoro è focalizzato sullo studio di sensori ottici basati su nanomateriali di carbonio, nell'ottica di un'applicazione di questi materiali come sensori di gas. Il lavoro prende in analisi due materiali, i nanotubi di carbonio (CNTs) e il grafene ossido (GO).

La comprensione dei meccanismi di interazione di questi materiali con le molecole di gas è fondamentale per le applicazioni future di questi materiali nel rilevamento di diverse specie nocive di gas. A tal proposito, nanostrutture a base di GO e CNTs sono state sviluppate e studiate come sensori ottici verso gas ossidanti-riducenti (H_2, CO, NO_2) e nei contronti di composti volatili organici aromatici (benzene, toluene, xylene).

Le nanoparticelle di oro sono state utilizzate come sonde ottiche grazie alla loro peculiare caratterista di risonanza plasmonica di superficie localizzata, la quale è estremamente sensibile alle variazioni di proprietà ottico-elettroniche del mezzo che le circonda, come l'indice di rifrazione, e alle variazione di densità di portatori di carica che sono coinvolti nell'eccitazione plasmonica nelle nanoparticelle di oro.

Quindi, le nanoparticelle di oro, non solo amplificano le variazioni optoelettroniche del film di nanomateriali di carbonio a cui sono state accoppiate, ma interagiscono con questi inducendo un miglioramento della risposta ai gas e un abbassamento del limite di rilevamento ai gas in analisi.

Inoltre, GO e CNTs presentano una vasta gamma di possibili funzionalizzazioni, che, possono essere sfruttate per una progettazione mirata delle proprietà di gas sensing delle nanostrutture di carbonio.

I CNTs sono stati abbinati a nanoparticelle di Au, Pd, Ni e a fullereni. Pd e Au portano ad un miglioramento delle prestazioni dei sensori verso il gas H_2, nanoparticelle di Ni e fullereni sembrano avere un'azione specifica verso il gas CO.

In questo lavoro viene anche suggerita la possiblità di monitorare le proprietà di assorbanza di fullereni e CNTs nel range del vicino IR. I CNTs, in tal caso, avrebbero la duplice funzione di sonde ottiche e di materiale sensibile.

Oltre all'effetto delle nanoparticelle di oro sulle proprietà di gas sensing del GO, è stata valutata l'influenza dei diversi gruppi funzionali. L'estensione dei domini sp2 sembra favorire il rilevamento di H_2, mentre una forte rimozione di gruppi funzionali inibisce la risposta del GO verso CO e NO_2.

La riduzione e funzionalizzazione del GO con para - fenilene diammina induce proprietà di gas sensing verso NH_3 senza la necessità di utilizzare nanoparticelle di oro come sonde ottiche.

I sensori prodotti sono caratterizzati da elevata trasparenza nel campo del visibile e possono essere incorporati come sensori non invasivi su superfici trasparenti.

La maggior parte dei sensori sono opertivi a 150 ° C e 300 ° C. Test di gas sensing sono stati condotti a basse temperature, a 80°C per CNT in matrice fullerene e buoni risultati sono stati raggiunti. La possibilità di sensori attivi a temperatura ambiente è suggerita dai test positivi condotti con CMG, aprendo la strada per i futuri sviluppi in materiale ottico attivo sensibile ai gas a temperatura ambiente.

Preface

This doctoral project has generated some results that have been published or presented at international conferences. Presentations and publications (also papers in preparation) are listed in the following list. Moreover, a part of the work has been conducted at overseas facilities.
The experimental part have been reported in Appendix A.2 ; the techniques used for characterization and the gas sensing set-up and procedure of the thin films are illustrated respectively in Appendix A.1 and Appendix A.3. This has been done to avoid repetition at every paragraph.

Refereed Journal Publications

E. Czerwosz, E. Kowalska, M. Kozłowski, J. Radomska, H. Wronka, M. Angiola, A. Martucci, W. Włodarski. "CNT-Ni-Pd Nanocomposite Films for Optical Gas Sensor".

M. Angiola, M. MYA Alsaif, K. Kalantar-zadeh, A. Wisitsoraat, W. Wlodarski, A. Martucci. "Optical Hydrogen Sensing Based on Hybrid 2D MoO3/Au Nanoparticles".

Marco Angiola, Christopher Rutherglen, Kos Galatsis, Alessandro Martucci. "Transparent carbon nanotube film as sensitive material for surface plasmon resonance based optical sensors". *In preparation.*

Presentations during National and International Conferences

SPIE Optics+Photonics 2015 Convention. 9^{th} -13^{th} August 2015 at the Convention Center of San Diego. Transparent carbon nanotube film as sensitive material for surface plasmon resonance based optical sensors (oral presentation).

Plasmonica 2015 Convention, 2^{nd} July2015 at Palazzo Moroni, Padova. Transparent carbon nanotube film as sensitive material for surface plasmon resonance based optical sensors (poster presentation).

Visit overseas

20th March 2014-30th May 2014 at California NanoSystem Institute, UCLA, Los Angeles.. Host: prof. Kos Galatsis.

Acknowledgment

The first person I'd like to acknowledge and deeply thank is my supervisor, prof. Alessandro Martucci, without whom my research activity wouldn't have been satisfactory and rewarding. Thank you for always being keen on answering all my questions, the professional support and the fruitful and open-minded discussions.

A grateful acknowledgement goes to prof. Kos Galatsis, for giving me the opportunity to spend a period of my pHD activity at UCLA in Los Angeles. A thank also to Chris Rutherglen for the help with and the teaching of the deposition and characterization of carbon nanotubes. I'd like to thank both for the useful discussions and precious suggestions.

The NanoEng Group, with prof. Guglielmi, Marco Sturaro, Andrea Paduano, Gianmarco Giordano, Elena Colusso is all acknowledged for the productive discussions and the sharing of the research experiences.

An acknowledge goes to Marco Bersani for the TEM images the precious suggestions and discussions.

Contents

Chapter 1 - Overview on optical gas sensors

1.1 Introduction

The interest in the detection of gases is increasing and involving many areas of application. In industrial processes, gas like CO and H_2S can be emitted in process stream and pipeline, methane in refinement of oil, and their concentration is a key parameter to be monitored.
In the medical field, the breath analysis is a non invasive technique to acquire information on the clinical condition of a person by simply recording the concentration of Volatile Organic Compounds (VOC) like ethanol, acetone,carbon dioxide and urea. This instrument allows the diagnosis of disease due to a direct correlation of the substance in the blood.
Another application of gas sensing is the monitoring of air in public spaces or also in private houses or cars considering the concentration of gases in the view of comfort (i.e. with the control of humidity).
Keeping in mind the peculiar condition for each application the sensor device has to be very precise and has to be operative in situ with adequate resistance to the specific operating conditions, such as temperature and without interference from other species.
A gas sensor has two fundamental components at the base of its functioning. Basically, the sensor convert a variation in a physical or chemical property into a processable signal. Hence, a sensing element interacts with the gas molecules and such interaction can be of different nature, like charge transfer, swelling, adsorption or chemisorptions of the molecules. The transducers converts the modification in properties of the sensing elements in a clear and distinguishable signal, like a change in resistance or in light beam intensity.
Different types of transducer can be employed like resistive[1] , Field Effect Transistors[2] [3] , acoustic[4] , mass sensitives[5] and optical[6] [7] .
Optical sensors operate thank to a modification of an optical property of the sensitive element induced by the interaction with the gas molecules. Meanwhile, in largely diffused resistive sensors a scalar quantity is varied by the gas molecules, optical sensors can rely on several parameters, such as light intensity, wavelength, light polarization and phase of transmitted or reflected beam. This wide range of operating parameters confer an extraordinary flexibility and selectivity of the optical sensors: the variation in intensity of the

light beam is dependent on the wavelength of analysis, so picking the proper wavelength a selective response to the target specie can be achieved.

The exploitation of the different parameters carried to the possibility of different modality of optical gas sensing. The absorbance-based, emission-based and surface-plasmon resonance-based are the most studied among them.

1.2 Absorbance-based sensors

In the absorbance based sensors the target molecules provoke a variation of the optical absorbance of the sensor. The light beam can be acquired in the transmission or in the reflection mode depending on the position of the detector and whether the sensor is deposited on transparent or reflective substrate.

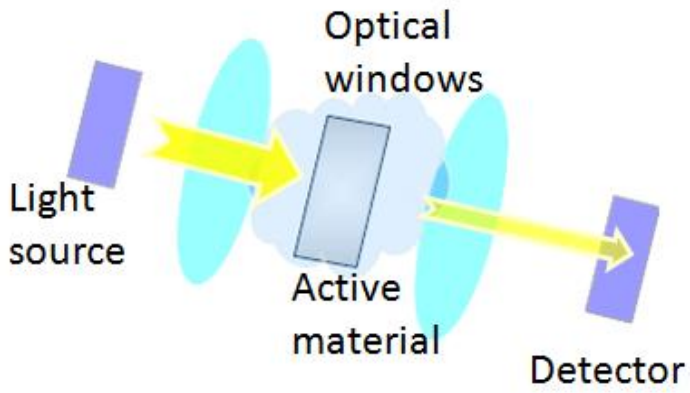

Figure 1.1 – Scheme of operation in transmission mode of an optical gas sensor.

In the transmission mode light (see figure 1.1)is emitted by a source (LED, light bulb, etc). The light beam intensity is affected by the variation in absorbance of the sensor when exposed to the gas target. The detector records the change in optical transmission, which is generally dependent on the wavelength. The selection of a proper wavelength may render the sensor selective to a specific specie even if it may be responsive to more gases at others wavelength, depending on the specific properties of the sensing element.

In the reflective mode the sensor is on reflective substrate and the reflected beam is acquired by a sensor at a fixed angle and the mechanism is the same as for the transmission mode. The main advantage is the possibility of applying the sensing element on an optical fiber. The fiber has the double function of illumination of the sensing element and collection of the light beam to the detector at the same time.

The emission based sensors employ the excitation of the electrons of the sensing element and their photoemission once they return to the ground base. Depending on the origin of the light emission from the material, the phenomenon at the ground of the gas sensing can be photoluminescence or chemoluminescence.

In photoluminescence the electrons are excited by the incident light and then the electrons emit light at higher wavelength, meanwhile in the chemoluminescence the emitting properties of the material are activated by a chemical reaction.

The core of this work focus on the Localized Surface Plasmon (LSPR) resonance sensors for the detection of reducing/oxidizing gases and aromatic-VOC (a-VOC).

1.3 Localized Surface Plasmon Reseonance sensors

The surface plasmon is a coherent oscillation of the conduction electrons of a material due to excitement with electromagnetic radiation. This is possible at the surface of a material with a negative real refractive index and small positive imaginary dielectric coupled with a dielectric material with positive dielectric constant[8] . Plasmonic is the study of the interaction of such matter-light interaction and is applied in this work for developing optical gas sensors.

The Surface Plasmon Resonance (SPR) has been exploited for the production of thin metal films for sensing application[9] . The plasmon resonance can propagate on the surface for distances of tens or hundreds of microns and is defined surface plasmon polariton. The polariton decays evanescently in the direction normal to the surface on length in the order of 200nm and is extremely sensitive to variation of the refractive index of the surrounding media [8] .

When a surface plasmon is localized in a particle of size comparable with the wavelength of the incident light beam, the free electrons of the particles participate to the collective oscillation, and it is termed Localized Surface Plasmon Resonance (LSPR).

As for flat surfaces, this phenomenon causes a strong localized amplification of the electric field close to the particles and the particle's optical extinction has a maximum at the plasmon resonant frequency, which occurs at visible wavelengths for noble metal nanoparticles[10] .

LSPR is influenced by the size and shape of the particles. The extinction spectrum of the particles is given by:

$$\sigma(\lambda) = \frac{24\pi N a^3 \varepsilon_d^{3/2}}{\lambda \ln(10)} \left[\frac{\varepsilon_i(\lambda)}{(\varepsilon_r + \chi\varepsilon_d)^2 + \varepsilon_i(\lambda)^2} \right] \quad (1)$$

Here, ε_r and ε_i are the real and imaginary components of the metal dielectric function, respectively. E_d is the dielectric constant of the external environment. N are the finite polarizable elements, each of which can interact with the applied electric field.

The function is dependent on the wavelength and on χ. χ is 2 for the case of a sphere, but it takes on values as large as 20 to account for particle geometries with high aspect ratios.

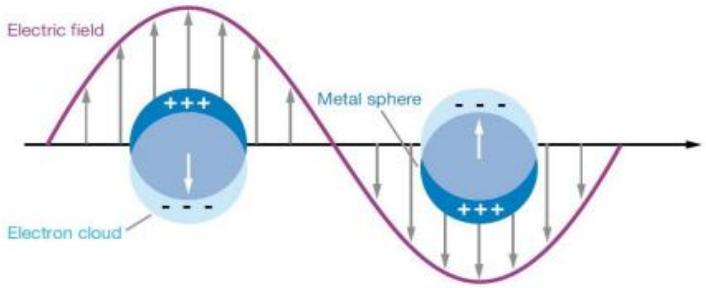

Figure 1.2 - Schematic diagrams illustrating a localized surface plasmon.

This extinction peak depends on the refractive index of the surrounding medium and is the basis for the sensing application.

The wavelength of the LSPR maximum is sensitive to the optoelectrical properties, i.e. the refractive index of the surrounding media:

$$\lambda_{LSPR} = \lambda_b \sqrt{2n_d^2 + 1} \quad (2)$$

Here n_d is the bulk refractive-index of the dielectric, λ_{LSPR} is the LSPR peak wavelength and λ_b is the wavelength corresponding to the plasma frequency of the bulk metal.

As mentioned above in equation (1) the LSPR absorbance peak is also affected by the variation in electron density, according to Drude theory[11]:

$$\omega_{LSPR} = \sqrt{\frac{Ne^2}{m_e \varepsilon_0 (\varepsilon_\infty + k\varepsilon_d)}}$$

With m_e the effective mass of the electron, N the number of free electrons in the particle, further tuned by the geometry of the nanostructure (k) and the medium surrounding the particle ε_d, ε_∞ is a high-frequency contribution of dielectric function to Drude theory [12].

References

[1] Wan Q, Li QH, Chen YJ, Wang TH, He XL, Li JP, Lin CL. Fabrication and ethanol sensing characteristics of ZnO nanowire gas sensors. Applied Physics Letters 2004;84:3654.
[2] Star A, Joshi V, Skarupo S, Thomas D, Gabriel J-CP. Gas Sensor Array Based on Metal-Decorated Carbon Nanotubes. The Journal of Physical Chemistry B 2006;110:21014–21020 .
[3] Morita Y, Nakamura K, Kim C. Langmuir analysis on hydrogen gas response of palladium-gate FET. Sensors and Actuators B: Chemical 1996;33:96–99
[4] Ricco AJ, Martin SJ, Zipperian TE. Surface acoustic wave gas sensor based on film conductivity changes. Sensors and Actuators 1985; 8:319-33.
[5] Jensen K, Kim K, Zettl A. An atomic-resolution nanomechanical mass sensor. Nature Nanotechnology 2008;3:533-537.
[6] Ando M, Kobayashi T, Haruta M. Combined effects of small gold particles on the optical gas sensing by transition metal oxide films. Catalysis Today 1997;36:135–141.
[7] Hodgkinson J, Tatam R. Optical gas sensing: a review. Measurement Science and Technology 2013;24:012004.
[8] Willets K, Duyne R. Localized Surface Plasmon Resonance Spectroscopy and Sensing. Annual Review of Physical Chemistry 2007;58:267–297.
[9] Homola J, Yee SS, Gauglitz G. Surface plasmon resonance sensors: review. Sensors and Actuators B: Chemical 1999;54:3-15.
[10] Mayer KM, Hafner JH. Localized surface plasmon resonance sensors. Chemical Reviews 2011;111:3828–3857.
[11] Kreibig U, Vollmer M. H. Optical Properties of Metal Clusters. Springer Series in Materials Science 1995.
[12] Jain K, El-Sayed M. Plasmonic coupling in noble metal nanostructures. Chemical Physics Letters 2010;487:153–164.

Chapter 2 - Carbon nanomaterials

2.1 Introduction

Carbon is the element at the base of life on earth and is extensively employed for drugs and technological production. Indeed, carbon can bind with almost all the elements of the periodic table conferring an incredible versatility of production of species with heterogeneous physical and chemical properties thanks to the organic chemistry.

The interest toward carbon materials has lively increased in the last decades with the discovery of fullerene in 1985 [1] and of carbon nanotubes in 1991 [2] and the synthesis of graphene in 2004 [3] .

The peculiar electronic, mechanical, thermal, optical and chemical properties render these material attractive for several application i.e. catalysis[4] [5] , biosensing[6] [7] and sensing application[8] [9] , electrical devices[10] [11] [12] .

The wide fashion of allotropies available, like 0D (fullerefene), 1D Carbon NanoTubes (CNTs) and 2D materials as graphene, have attracted most of the interest but also structures as nanoparticles, diamonds, fibres, cones, scrolls, whiskers, graphite polyhedral crystals and nanoporous carbon can be exploited for different applications. Differently to diamond, which is composed of sp^3 carbon, with a C-C bond distance of 3.57Å, graphite is a layered material composed of sheets with sp^2 carbon with C-C distance of 1.42 Å and stacking among sheets of 3.35 Å. The other allotropes mentioned above are composed of sp^2 and/or sp^3 carbon too.

The connection of the sp^2 carbons forming different networks leads to the nanostructures this chapter will focus on.

2.2 Fullerene

C_{60} was named buckminsterfullerene for its resemblance of the Buckminster Fuller' Geodesic dome architecture.

Fullerene can be visualized as an irregular graphene sheet curled to form a sphere, including pentagons in its structure and comes in various forms and sizes ranging from 30 to 3000 carbon atoms[9] .

Each molecule of fullerene consists of 12 pentagons and m hexagons, with $m=(n-20)*2^{-1}$.

C_{60} was the first of this class to be discovered, in 1985, by laser ablation of graphite in helium flow by Kroto et al[1].

Different synthesis techniques were set up for the synthesis including electric arc discharge, electron beam ablation[13] , sputtering[14] , plasma synthesis[15] and wet chemistry techniques[16] .

The synthesis of large quantity of material in 1990 and the discovery of superconductive behavior of an alkali-doped fullerenes, increased the interest for fullerene considerably.

Fullerenes can be considered a large molecules of sp^2 carbon. However, the curvature of the compound creates strong strains that causes a rehybridization with a partials sp^3 character, $sp^{2.278}$, and confer a minor thermodynamic stability of fullerene compared to graphite[17] .

The prevalent sp^2 character of the constituting carbon leads to a conjugated π-electron system. The delocalization of the electrons and the size of a molecule confer peculiar electrical structure to C_{60}, an electrical semiconductor nature with mobility edge of 2.25 eV and optical gap of 1.65 eV[18] .

The possibility of modification of the material can be used to tailor the final properties. Fullerene can be treated with the method of organic chemistry (arylation, halogenation, hydroxylation, alkoxylation, osmylation) [19] obtaining a substance with intermediate properties of the starting reagent. It can also be combined with metals in the synthesis process with the possibility of a fine-tuning of the electric properties of fullerenes[20] .

Fullerene demonstrated also interesting properties in the generation of photoinduced current[21] photocatalysis field[22] and as optical liming material[23]

2.3 Carbon nanotubes

The studies on the properties and synthesis of fullerenes led to an increasing interest toward accessible graphitic materials. In 1991 Ijima discovered carbon nanotubes (CNTs) with a technique derived from the synthesis of fullerenes[2] .

CNTs consist in a graphene sheet closed in tubular shape, that may be capped or not. They can be divided in Single Wall Carbon Nanotubes (SWCNTs) or in MultiWall Carbon Nanotubes (MWCNTs) if composed respectively of a single layer or more concentric sheets.

The science developed on the production of fullerene was transferred to carbon nanotubes leading to the synthesis based on evaporation of metal and graphite [24] and generation of a

plasma[25] . Later development allowed a higher yield using as starting materials metal embedded in graphite[26] [24] and the production of high quality Single Wall Carbon Nanotubes and Multiwall Carbon Nanotubes with Chemical Vapor Deposition (CVD) as vertical aligned arrays[27] [28] [9] .

Up-to-date the synthesis of carbon nanotubes reach commercial production, even if further development for a cheaper and larger production would be appreciable.

In addition to the synthesis, a procedure of purification is followed to remove impurities as metal catalysts and adducts on the surface of the CNTs. The procedure may require high vacuum annealing, air oxidation or be based on acid etching followed by thermal treatment to remove the oxygen defects formed by acid treatment[29] .

The advance in production techniques is amply justified by the extraordinary properties of CNTs, like elevated mechanical properties[30] thermal and electrical conduction [31,32] . The electrical properties were found to vary with the structure [32] . The diameter and the angle of wrapping give a measure of the helicity and small variations of this parameter can cause a variation from semiconductive to metallic behavior [33] .

In the next chapter the differences in properties of metallic and semiconductive SWCNTs and MWCNTs will be discussed.

2.3.1 Single Wall Carbon Nanotubes

SWCNTs are graphene sheets wrapped such that the two equivalent sides of the hexagonal lattice match each other. The wrapping vector C is defined with the pair of integer number (n,m) defining the relative position of these two points in respect of the relation $C=na_1+ma_2$. A tube is called armchair if n=m, zigzag for m=0. All the others are chiral tubes with a wrapping angle $0°<\varphi< 30°$[33] . A schematic of the possible wrapping vectors of a graphene sheet is visualized in Figure 2.1.

The correlation between the building structure of the CNTs and the electrical properties is observed with the electron bands of the CNTs related to the Fermi energy of the single type of SWCNT. The armchair have metallic behavior, meanwhile chiral and zigzag tubes are metallic if it is verified the relation n-m=3l, l integer number, otherwise they are semiconductive SWCNTs with a band-gap E_g~0.5eV [33] .

The electronic properties of carbon nanotubes presents unique properties due to the one dimensionality and short sizes with spike-like electron density states, called Van Hove

singularities [31,34] [35] . A third of the CNTs types are metallic carbon and exhibit a wider first energy gap between the spikes than first van Hove transition of semiconductor carbon nanotubes.

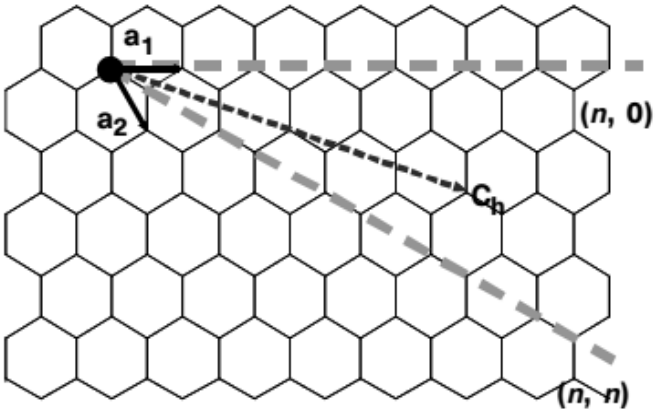

Figure 2.1 - Schematic of a two-dimensional graphene sheet illustrating lattice vectors a_1 and a_2, and the roll-up vector $c_h=na_1+ma_2$. The limiting cases of (n,0) zigzag and (n,n) armchair tubes are indicated with dashed lines. As represented here, the angle between the zigzag configuration and c_h is negative[36] .

The electron transitions between the singularities in the valence and conduction bands of SWCNTs produce the characteristic features of SWCNTs in UV/vis/NIR range. In the visible-NIR range the semiconductive SWCNTs present two electronic transition S11(~0,68eV), S22(~1,2eV), while metallic only one, M11(~1,7eV). The position of the optical transitions are dependent on the diameter and the chirality so that an experimental correlation between diameter and band position in the absorbance spectrum of CNTs can be traced with Kataura plots[37] .

Metallic SWCNTs present ballistic conduction[31] and also semiconductive SWCNTs, if sufficiently pure, can exhibit ballistic conduction of carriers in valence and conduction bands [38] .

To exploit this properties, CNT Field Effect Transistor (FET) have been studied. It was observed that the devices suffered of limited conduction due to Schottky barrier between the semiconductive SWCNTs and the metal electrodes. The absence of dangling bonds allows the coupling with dielectrics with high dielectric constant, k, value. Techniques of deposition at room temperature have been developed allowing the deposition of thin transparent film in non-aggressive condition and applicable on plastic, for flexible and stretchable devices[39] .

CNT transistors have been proved sensitive to low concentrations of gases observing changes in electrical resistance of the film [40] [41] .

The electrical conductivity of the SWCNTs can be degraded by the presence of a defect on the wall. Its 1D structure make CNT mechanical, electrical properties and chemical reactivity strongly sensitive to the presence of defects site on the wall .

Efforts are going in the direction of obtaining pristine carbon nanotubes [42] [43] and in the exploitation of the enhanced reactivity of the defect sites for specific applications, as gas detection [44]. Oxidation defects were induced on the surface of SWCNTs to enhance the sensing response toward H_2[45] . An alternative functionalization is the addition of metallic catalytic nanoparticles[46] [47] , metal oxide nanoparticles[48] and polymers with the target of exploiting the specific reactivity of the added material[49] [50] .

Several mechanisms have been proposed for the gas sensing with SWCNTs and they are mostly based on the electrical conductivity of semiconductive SWCNTs. A mechanism foresees the adsorption of the gas molecules on the walls of SWCNTs with a charge transfer, causing an alteration of the electrical conductance [51] . In a second possible mechanism a molecular gating of the polar molecules create a depletion area where the molecules are adsorbed with the modulation of the electrical resistance of the CNTs[52] . Another possible mechanism relies on the formation of a Schottky barrier between the CNTs and the electrodes or with the particles[47] used to increase the sensitivity of the SWCNTs film and alteration of the conductivity[53] .

2.3.2 Multi Wall Carbon Nanotubes

Multi Wall Carbon Nanotubes (MWCNTs) are constituted of a concentric shells of SWCNTs of various helicity. Hence, the electrical conduction depends on the coupling of the adjacent shells, but the outer shell is predominant to dictate the electrical properties of the whole MWCNT. The resistivity perpendicularly the tube is very high, layers insulated one by the other and consequently the conductance is related to the external tube because of the weak inter-shell interactions [54]. One third of the layers should conduct and the rest presents a band gap which inhibits the conduction. If the next to the outer shell is insulating, no contribution is carried by the inner layers to the conductivity of the whole MWCNT [54] .

Different studies report the MWCNTs as semimetallic 2D conductors when they have a large diameter [55] . In general, mats of MWCNTs are mainly composed of metallic MWCNTs with semiconductive tubes present amid the metallic.

For this reason their normalized response to gases has appeared less intense than with SWCNTs mats, that exhibit a stronger presence of semiconductive SWCNTs[53] . The gas sensing response is ruled by the change in p-conductivity in MWCNTs and the formation of Schottky barrier with the metallic ones in impendance sensors. The first step is the sorption of the gas molecules on the surface of semiconductive MWCNTs, occurring with a charge transfer from them to the CNTs. The capacitive sensors displayed superior performance since they better exploit the charge transfer and the presence of metallic and semiconductive CNTs composing the sensor[53,56] .

The sensing properties of MWCNTs has been investigated[57] , but they have been subjected to functionalization to improve their sensing performance. On this purpose , oxygen functional group [39] and metallic nanoparticles (Au, Pt) NPs[58] [59] have been exploited with encouraging results[50] .

2.4 Graphene oxide

Graphene is a 2-dimensional of sp^2 carbon that was isolated for the first time in 2004 by Novoselov and Geim [3] . Before their discovery, this material was not thought to be possible for thermodynamic reasons. The quasi-2D epitaxial material produced were stabilized by the substrate which also alters its electrical properties[60] . Exfoliated single- and few-layer graphene can be stable pinned on the substrate by simple Van der Waals interactions [61] .

Graphene was amply studied theoretically and practically and displayed new extraordinary properties[62] , paving the way for new concepts of electrical devices[61] .

Graphene is a zero band-gap semiconductor or semimetal, in which the Highest Occupied Molecular Orbital (HOMO) touches the Lowest Unoccupied Molecular Orbital (LUMO) in a single Dirac point, as depicted in Figure 2.2. The interaction of electrons with periodic carbon lattice give rise to quasiparticles, called Dirac fermions with an effective speed of light $v_f \approx 10^6 m^{-1}s^{-1}$. They can be seen as electron with no mass[62] .

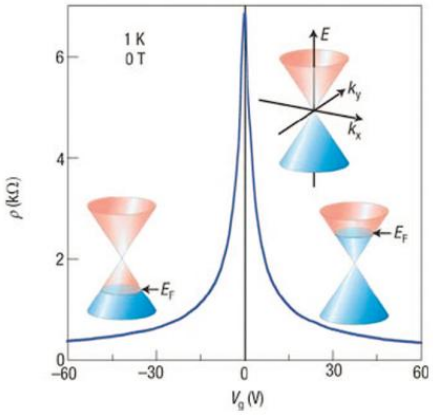

Figure 2.2 – Schematic diagram showing the band structure and resulting ambipolar field effect in graphene. Conduction and valence bands meet at the Dirac point without an external field. Under gate bias, the Fermi level moves above or below the Dirac point to introduce a significant number of free carriers[62] .

For stacking of multiple layers, the density of states (DOS) turns in an overlap of the conduction and valence band with a consequent metallic behavior.

The electrical properties of graphene are related to the high purity of the material and the 2D lattice[63–65] [66] , removing the scattering of the carriers, conduction values over 200000cm^2/(V s) can be achieved[67] .

A strong limit of graphene is the production. The highest purity is achieved by mechanical exfoliation of graphite. The routes for a large production of this nanomaterial leaded to the discovery of graphene oxide.

Graphene oxide (GO) was synthesized far before the interest in graphitic materials. the first synthesis were carried by Brodie[68] , Staudermeier[69] , in the XIX century and Hummers[70] in 1959.

The Hummer method was then replicated to obtain a precursor of graphene. The graphite stacks were etched in a solution of $KMnO_4$ and HNO_3. These two compounds form Mn_2O_7, which is more aggressive compound and attacks carbon double bonds. The final product is hydrophilic GO. The hydrophilic character is given by isolated graphitic clusters surrounded by oxygen functional groups, i.e. hydroxyls, lactones, carboxylic and epoxy groups[71] [72] . The disrupture of the sp^2 conjugation and the presence of oxidized groups render GO a new material with properties different than pristine graphene[73] [74] : he hydrophilic nature eases the manipulation of these compound with the wet chemistry techniques[75] , but the disrupture of the sp^2 conjugation renders GO an electrical insulator[73] [74] .

Hence, the different chemical structure is followed by new properties and GO can be considered a new distinct material from pristine graphene.

2.3.1 Reduced Graphene Oxide

In order to recover, at least in part, the properties of graphene different treatment of reduction of GO have been studied and reported in literature. They can be divided in thermal annealing in vacuum, chemical reduction in reducing atmosphere and elevated temperature and chemical reduction in a solution with a reducing agent.

The reduction by thermal annealing in vacuum leads to the removal of oxygen functional groups, but there is not a complete recovery of the sp^2 lattice. Residual functional groups remain, since they cannot be removed without heavily damaging the structure. Moreover, the removal of the functional groups leads to holes, Stonewales defects, and disorder in the lattice[76] .

An improvement in thermal reduction can be achieved using a reducing atmosphere: the employment of hydrogen may heal the structure of GO leading to a recovery of the sp^2 conjugation[76] [77] . Similar results were observed with NH_3 but the reduction was accompanied by N doping of graphene sheets[77] .

Treatments of chemical reduction have been carried with different reagents. The reduction with hydrazine is simple and it has been largely exploited[78]. The procedure is simply based on the addition of hydrazine to a water solution of GO and the batch may become scalable for industrial production. The reduced graphene oxide (rGO) so obtained tends to agglomerate because of the minor hydrophilic character of the rGO. $NaBH_4$ is the most efficient reducing agent but has low action on epoxy and hydroxyl groups, so other reagents have been tested. Ascorbic acid has been used as chemical reducing agent. C/O ratio of 12.5 can be achieved and the ascorbic acid stabilized the rGO in solution since no traces of aggregation were observed.

Among the advantages of the chemical reduction the process can be conducted at low or moderate temperature and the reagent may be selective toward specific functional groups[78] .

rGO was obtained also with photocatalytic reduction, electrochemical reaction and solvothermal treatment. The different methods of reduction can be combined to obtain the desired structure or a stronger reduction[78] .

Differently to graphene oxide, rGO is a semiconductor material. The band gap is related to the σ states of the sp^3 carbon still present after the reduction treatments.

Its properties of semiconductor material render it an interesting material for sensors and photocatalysis. Indeed, theoretical studies showed that photocatalytic behavior of rGO can be tailored with the chemical structure[39] .

Novoselov and co-workers reported graphene-based gas sensing devices for detecting single molecules [3]. This pioneering work inspired research on graphene based gas sensors and a large interest in graphene-based sensors has emerged [79] . rGO has proved an effective sensor alone or in combination with metallic nanoparticles [80] , semiconductors nanoparticles [81,82] and polymers with non-covalent functionalization [83] .

The GO offers a wide range of functionalization thank to the presence of defects as reactive sites. Molecules and polymer can be grafted with the organic chemistry techniques[84] [85] . The functionalization allows a higher and/or preferential sensitivity toward dangerous gas species or target molecules. The high possibility of functionalization of GO donates an incredible flexibility of tailoring the properties of the material toward a specific specie target or further applications[86] [85] [87] .

The production of thin film transistor with chemically rGO has been pursued too. A device with ambipolar characteristics were achieved in vacuum condition. However, the conductivity is affected by the scattering at defects sites and at junction among sheets and the device exhibit p-doping by oxygen adsorption on the surface[88] .

Thus, the possibility offered by rGO are extremely wide thank to the high freedom of tailoring this material toward the requirements of the desired application in several technological fields.

Refererence

[1] Kroto HW, Allaf AW, Balm SP. C60: Buckminsterfullerene. Chemical Reviews 1991;91:1213–1235.

[2] Iijima S. Helical microtubules of graphitic carbon. Nature 1991;354:56–58.

[3] Novoselov KS, Geim AK, Morozov SV, Jiang D, Zhang Y, Dubonos SVl. Grigorieva IV, Firsov AA. Electric field effect in atomically thin carbon films. Science 2004;306:666–669.

[4] Serp P, Corrias M, Kalck P. Carbon nanotubes and nanofibers in catalysis. Applied Catalysis A 2003;253:337–358.

[5] Yu D, Nagelli E, Du F, Dai L. Metal-free carbon nanomaterials become more active than metal catalysts and last longer. Journal of Physical Chemistry 2010;1:2165–2173.

[6] Yang W, Ratinac KR, Ringer SP. Carbon nanomaterials in biosensors: should you use nanotubes or graphene? Angewandte Chemie 2010;49:2114–2138.

[7] Vamvakaki V, Tsagaraki K, Chaniotakis N. Carbon nanofiber-based glucose biosensor. Analytical Chemistry 2006;78:5538–5542.

[8] Llobet E. Gas sensors using carbon nanomaterials: A review. Sensors and Actuators B 2013;79:32–45.

[9] Jariwala D, Sangwan VK, Lauhon LJ. Carbon nanomaterials for electronics, optoelectronics, photovoltaics, and sensing Chemjcal Society Review 2013;42:2824–2824.

[10] Liu S, Guo X. Carbon nanomaterials field-effect-transistor-based biosensors. NPG Asia Materials 2012;4:1–10.

[11] Snow ES, Campbell PM, Ancona MG. High-mobility carbon-nanotube thin-film transistors on a polymeric substrate. Applied Physics Letters2005;86:033105.

[12] Simon P, Gogotsi Y. Materials for electrochemical capacitors. Nature Materials 2008;7:845–854.

[13] Smalley RE. Self-assembly of the fullerenes. Account of Chemical Research 1992;25:98–105.

[14] Bunshah RF, Jou S, Prakash S, Doerr HJ. Fullerene formation in sputtering and electron beam evaporation processes. Journal of Physical Chemistry 1992;96:6866–6869.

[15] Churilov GN. Plasma synthesis of fullerenes (review). Instruments and Experimental Techniques. Springer 2000;43:1–10.

[16] Scott LT. Methods for the Chemical Synthesis of Fullerenes. Angewandte Chemie 2004;43:4994 – 5007.

[17] Hirsch A. Principles of fullerene reactivity. Springer 1999.

[18] Makarova TL. Electrical and optical properties of pristine and polymerized fullerenes. Semiconductors 2001;35:243–278.

[19] Diederich o. F, Thilgen C. Covalent Fullerene Chemistry. Science 1996;271:317–324.

[20] Lee K, Song H, Park JT. [60]Fullerene−Metal Cluster Complexes: Novel Bonding Modes and Electronic Communication. Accounts of Chemical Research 2003;36:78–86.

[21] Wienk MM, Kroon JM, Verhees WJ, Knol J, Hummelen JC, van Hal PA, R Janssen, Efficient Methano[70]fullerene/MDMO-PPV Bulk Heterojunction Photovoltaic Cells. Angewandte Chemie 2003;115:3493–3497.

[22] Yang MQ, Zhang N, Xu YJ. Synthesis of fullerene–, carbon nanotube–, and graphene–TiO2 nanocomposite photocatalysts for selective oxidation: a comparative study. Applied Material and Interfaces 2013;5:1156−1164.

[23] Tutt LW, Boggess TF. A review of optical limiting mechanisms and devices using organics, fullerenes, semiconductors and other materials. Progress in Quantum Electronics 1993;17:299–338.
[24] Bethune DS, Klang CH, Vries MS de, Gorman G, Savoy R, Vazquez J, et Beyers R. Cobalt-catalysed growth of carbon nanotubes with single-atomic-layer walls. Nature 1993;363:605–607.
[25] Ebbesen TW, Ajayan PM. Large-scale synthesis of carbon nanotubes. Nature 1992;358:220–222.
[26] Guo T, Nikolaev P, Thess A, Colbert DT, Smalley RE. Catalytic growth of single-walled manotubes by laser vaporization. Chemical Physics Letters 1995;243:49–54.
[27] Li WZ, Xie SS, Qian LX, Chang BH, Zou BS, Zhou WY, Zhao RA, Wang G. Large-Scale Synthesis of Aligned Carbon Nanotubes. Science 1996;274:1701–1703.
[28] Hata K. Water-Assisted Highly Efficient Synthesis of Impurity-Free Single-Walled Carbon Nanotubes. Science 2004;306:1362–1364.
[29] Collins PG. Defects and disorder in carbon nanotubes, Oxford Handbook of Nanoscience and Technology: Frontiers and Advance 2010.
[30] Lu J. Elastic properties of carbon nanotubes and nanoropes. Physical Review Letters 1997;79:1297.
[31] Tans SJ, Devoret MH, Dai H, Thess A. Individual single-wall carbon nanotubes as quantum wires. Nature 1997;386:474–477.
[32] Ebbesen TW, Lezec HJ, Hiura H, Bennett JW, Ghaemi HF, Thio T. Electrical conductivity of individual carbon nanotubes. Nature 1996;382:54–56.
[33] Wilder J, Venema LC, Rinzler AG, Smalley RE. Electronic structure of atomically resolved carbon nanotubes. Nature 1998;391:59–62.
[34] Hamada N, Sawada S, Oshiyama A. New one-dimensional conductors: Graphitic microtubules. Physical Review Letters 1992;68:1579–1581.
[35] Saito R, Fujita M, Dresselhaus G, Dresselhaus MS. Electronic structure of chiral graphene tubules. Applied Physics Letters 1992;60:2204.
[36] Odom T, Huang J-L, Kim P, Lieber CM. Atomic structure and electronic properties of single-walled carbon nanotubes. Nature 1998;391:62–64.
[37] Kataura H, Kumazawa Y, Maniwa Y, Umezu I, Suzuki S, Ohtsuka Y,Achiba Y. Optical properties of single-wall carbon nanotubes. Synthetic Metals 1999;103:2555–2558.
[38] Javey A, Guo J, Wang Q, Lundstrom M, Dai H. Ballistic carbon nanotube field-effect transistors. Nature 2003;424:654–657.
[39] Dhall S, Jaggi N. Highly dispersed platinum sputtered multiwall carbon nanotubes based hydrogen gas sensor at room temperature. Sensors and Actuators A: Physical 2015;224:50–56.
[40] Kong J. Nanotube Molecular Wires as Chemical Sensors. Science 2000;287:622–625.
[41] Someya T, Small J, Kim P, Nuckolls C, Yardley JT. Alcohol Vapor Sensors Based on Single-Walled Carbon Nanotube Field Effect Transistors. Nano Letters 2003;3:877–881.
[42] Wang J, Zhang L, Liu Y song, Guo X. One-step and low-temperature synthesis of carbon nanotubes with no post treatment and high purity. Royal Society of Chemistry Advances 2015;5:78917–78919.
[43] Kim K, Kingston CT, Ruth D, Barnes M, Simard B. Synthesis of high quality single-walled carbon nanotubes with purity enhancement and diameter control by liquid precursor Ar–H2 plasma spraying. Chemical Engineering Journal 2014;250:331–341.

[44] Charlier J-C, Arnaud L, Avilov I, Delgado M, Demoisson F, Espinosa E, Ewels CP, Felten A, Guillot J, Ionescu R, Leghrib R, Llobet E, Mansour A, Migeon HN, Pireaux JJ, Reniers F, Suarez-Martinez I, Watson GE, Zanolli Z. Carbon nanotubes randomly decorated with gold clusters: from nano2hybrid atomic structures to gas sensing prototypes. Nanotechnology 2009;20:375501.
[45] Khalap V, Sheps T, Kane A, Collins P. Hydrogen sensing and sensitivity of palladium-decorated single-walled carbon nanotubes with defects. Nano Letters 2010;10:896–901.
[46] Star A, Joshi V, Skarupo S, Thomas D, Gabriel J-CP. Gas Sensor Array Based on Metal-Decorated Carbon Nanotubes. The Journal of Physical Chemistry B 2006;110:21014–21020 .
[47] Kong J, Chapline MG, Dai H. Functionalized Carbon Nanotubes for Molecular Hydrogen Sensors. Advanced Materials 2001;13:1384–1386.
[48] Lu G, Ocola LE, Chen J. Room-Temperature Gas Sensing Based on Electron Transfer between Discrete Tin Oxide Nanocrystals and Multiwalled Carbon Nanotubes. Advanced Materials 2009;21:2487–249.
[49] An KH, Jeong SY, Hwang HR, Lee YH. Enhanced sensitivity of a gas sensor incorporating single-walled carbon nanotube-polypyrrole nanocomposites 2004;16:1005–1010.
[50] Ding M, Tang Y, Gou P, Reber MJ, Star A. Chemical sensing with polyaniline coated single-walled carbon nanotubes. Advanced Materials 2011;23:536–40.
[51] Li J, Lu Y, Ye Q, Cinke M, Han J, Meyyappan M. Carbon Nanotube Sensors for Gas and Organic Vapor Detection. Nano Letters 2003;3:929–933.
[52] Kong J, Franklin NR, Zhou C, Chapline MG, Peng S. Nanotube molecular wires as chemical sensors. Science 2000;287:622–62.
[53] Zhang W-D, Zhang W-H. Carbon Nanotubes as Active Components for Gas Sensors. Journal of Sensors 2009;2009:1–16.
[54] Frank S, Poncharal P, Wang ZL, Heer WA de. Carbon nanotube quantum resistors. Science 1998;280:1744–1746.
[55] Charlier JC, Issi JP. Electronic structure and quantum transport in carbon nanotubes. Applied Physics A 1998;67:79–87.
[56] Varghese OK, Kichambre PD, Gong D, Ong KG. Gas sensing characteristics of multi-wall carbon nanotubes. Sensors and Actuators B 2001;81:32–41.
[57] Guo K, Jayatissa A. Hydrogen sensing properties of multi-walled carbon nanotubes. Materials Science and Engineering: C 2008;28:1556–1559.
[58] Kumar M, Ramaprabhu S. Nanostructured Pt Functionlized Multiwalled Carbon Nanotube Based Hydrogen Sensor. The Journal of Physical Chemistry B 2006;110:1129111298.
[59] Penza M, Cassano G, Rossi R, Alvisi M, Rizzo A, Signore MA, Giorgi R. Enhancement of sensitivity in gas chemiresistors based on carbon nanotube surface functionalized with noble metal (Au, Pt) nanoclusters. Applied Physics Letters 2007;90:173123.
[60] Stangl J, Holý V, Bauer G. Structural properties of self-organized semiconductor nanostructures. Reviews of Modern Physics 2004;76:725–783.
[61] Rao CNR, Sood AK, Subrahmanyam KS, Govindaraj. Graphene: The New Two-Dimensional Nanomaterial. Angewandte Chemie 2009;48:7752–7777.
[62] Geim AK, Novoselov KS. The rise of graphene. Nature Materials 2007;6:183–91.

[63] Du X, Skachko I, Barker A, Andrei EY. Approaching ballistic transport in suspended graphene. Nature Nanotechnology 2008;3:491–495.
[64] Novoselov KS, Jiang D, Schedin F, Booth TJ, Khotkevich VV, Morozov SV, Geim AK. Two-dimensional atomic crystals. Proceedings of the National Academy of Sciences of the United States of America 2005;102:10451–3.
[65] Novoselov K, Geim A, Morozov S, Jiang D, Katsnelson M, Grigorieva I, Dubonos SV, Firsov AA. Two-dimensional gas of massless Dirac fermions in graphene. Science 2005;438:197–200.
[66] Hwang EH, Adam S, Sarma SD. Carrier transport in two-dimensional graphene layers. Physical Review Letters 2007;98:186806.
[67] Morozov SV, Novoselov KS, Katsnelson MI, Schedin F, Elias DC, Jaszczak JA, Geim AK. Giant Intrinsic Carrier Mobilities in Graphene and Its Bilayer. Physical Review Letters 2008;100:016602.
[68] Brodie BC. On the Atomic Weight of Graphite. Philosophical Transactions of the Royal Society of London 1859;149:249–259.
[69] Staudenmaier L. Verfahren zur Darstellung der Graphitsäure. Berichte Der Deutschen Chemischen Gesellschaft 1898;31:1481–1487.
[70] Hummers WS, Offeman RE. Preparation of Graphitic Oxide. Journal of the American Chemical Society 1958;80:1339–1339.
[71] Mattevi C, Eda G, Agnoli S, Miller S, Mkhoyan AK, Celik O, Mastrogiovanni D, Granozzi , Garfunkel E. Chhowalla M. Evolution of electrical, chemical, and structural properties of transparent and conducting chemically derived graphene thin films. Advanced Functional Materials 2009;19:2577.
[72] Dreyer D, Park S, Bielawski C, Ruoff R. The chemistry of graphene oxide. Chemical Society Reviews 2009;39:228–240.
[73] Tung VC, Allen MJ, Yang Y, Kaner RB. High-throughput solution processing of large-scale graphene. Nature Nanotechnology 2008;4:25–9.
[74] Park S, Ruoff RS. Chemical methods for the production of graphenes. Nature Nanotechnology 2009;4:217–224.
[75] Li D, Müller MB, Gilje S, Kaner RB, Wallace GG. Processable aqueous dispersions of graphene nanosheets. Nature Nanotechnology 2008;3:101–105.
[76] Bagri A, Mattevi C, Acik M, Chabal Y, Chhowalla M, Shenoy V. Structural evolution during the reduction of chemically derived graphene oxide. Nature Chemistry 2010;2:581–587.
[77] Li X, Wang H, Robinson JT, Sanchez H. Simultaneous nitrogen doping and reduction of graphene oxide. Journal of the American Chemical Society 2009;131:15939–15944.
[78] Pei S, Cheng H-M. The reduction of graphene oxide. Carbon 2012;50:3210–3228.
[79] Basu S, Bhattacharyya P. Recent developments on graphene and graphene oxide based solid state gas sensors. Sensors and Actuators B 2012; 173:1–21
[80] Johnson JL, Behnam A, Pearton SJ. Hydrogen Sensing Using Pd-Functionalized Multi-Layer Graphene Nanoribbon Networks. Advanced Materials 2010;22:4877–4880.
[81] Deng S, Tjoa V, Fan H, Tan H, Sayle DC, Olivo M, Mhaisalkar S,Wei S, Sow CH. Reduced graphene oxide conjugated Cu2O nanowire mesocrystals for high-performance NO2 gas sensor. Journal of the American Chemical Society 2012;134:4905–4917.
[82] Palanisamy S, Chen S-M, Sarawathi R. A novel nonenzymatic hydrogen peroxide sensor based on reduced graphene oxide/ZnO composite modified electrode. Sensors and Actuators B 2012;166:372–377.

[83] Hu N, Yang Z, Wang Y, Zhang L, Wang Y, Huang, Zhang Y. Ultrafast and sensitive room temperature NH3 gas sensors based on chemically reduced graphene oxide. Nanotechnology 2014;25:025502.
[84] Ma H-L, Zhang H-B, Hu Q-H, Li W-J, Jiang Z-G, Yu Z-Z, Dasari A. Functionalization and reduction of graphene oxide with p-phenylene diamine for electrically conductive and thermally stable polystyrene composites. Applied Materials & Interfaces 2012;4:1948–1953.
[85] Yuan W, Liu A, Huang L, Li C, Shi G. High-Performance NO2 Sensors Based on Chemically Modified Graphene. Advanced Materials 2013;25:766–771.
[86] Georgakilas V, Otyepka M, Bourlinos A, Chandra V, Kim N, Kemp K, Hobza P Zboril R, Kim KS. Functionalization of Graphene: Covalent and Non-Covalent Approaches, Derivatives and Applications. Chemical Reviews 2012;112:6156–6214.
[87] Xiong S, Li Z, Gong M, Wang X, Fu J, Shi Y, Wu B, Chu J. Covalently Bonded Polyaniline and para-phenylenediamine Functionalized Graphene Oxide: How the Conductive Two-dimensional Nanostructure Influences the Electrochromic Behaviors of Polyaniline 2014;138:101–108.
[88] Eda G, Fanchini G, Chhowalla M. Large-area ultrathin films of reduced graphene oxide as a transparent and flexible electronic material. Nature Nanotechnology 2008;3:270–274.

Chapter 3 - Optical gas sensor based on graphene oxide

3.1 Enhancement of optical gas sensing properties of nanoplasmonic sensor based on graphene oxide coupled with gold nanoparticles

3.1.1 Introduction

In the last decade graphene and graphene oxide have attracted large interest for their peculiar properties. Graphene consists of a single graphite sheet and present unique property such as high mechanical properties, thermal conductivity (~5000 $Wm^{-1}K^{-1}$) [1] , elevated specific area(calculated value, 2630 m^2g^{-1}) [2] and more interestingly is zero-band gap semiconductor with ballistic conduction [3] .

The effort of a cheap and large scale production of graphene leaded to the synthesis and study of graphene oxide (GO) as a new material with properties differing from pristine graphene[4] [5] .

GO differs for the presence of oxidized groups that reduce the π-conjugation to isolated graphitic clusters[6] . The presence of oxygen functionalities confer hydrophilic behavior and so processability of the material with wet chemistry techniques[7] , but the presence of functional groups strongly affect the electrical properties making GO an insulator.

In the attempt to recover the electrical properties of graphene oxide different ways have been considered in literature, i.e. chemical reduction, thermal annealing, electrochemical reduction in attempt to restore the π-conjugation[8] .

Reduced graphene oxide (rGO) presents hybrid features of the conducting π states and large energy gap, between the σ-states of its sp^3-bonded carbons with the presence of disorder and defects like holes, Stone-wales defects (5-7-7-5 carbon rings), and residual oxygen group that cannot be removed without the destroying of the graphene basal plane[9] .

Theoretical studies showed that the thermal reduction in an atmosphere containing H_2 can reduce the defects and also carry to a partial healing of the lattice[10] and also reported a dependence of the chemical structure with the photocatalytic activity of the GO[11] that make it an interesting material for optical gas sensors.

The aim of the study is a progressive reduction of GO in an atmosphere of H_2(5%v/v Argon) at different temperature (150°C, 250°C, 350°C and 500°C) to investigate the chemical

structure of graphene oxide obtained for each treatment and relate the changes in functional groups with the optical gas sensing properties of reduced graphene.

To this purpose the GO was coupled with Au NPs to exploit the characteristic LSPR peak of the Au NPs as optical probe sensitive to the variation of optoelectrical properties of the rGO layer. Moreover, Au NPs displayed the ability of extending the photocatalytic properties of GO thank to a strong interaction between the two nanomaterials[12].

At the best of our knowledge, rGO has been widely employed in gas sensing but poor attention has been paid to the influence of the reduction process and structure of rGO to its gas sensing performance. This work is focused on the correlation between gas optical sensing properties and functionalization of graphene oxide.

3.1.2 Experimental section

3.1.2.1 Gold nanoparticles monolayer

Au NPs were prepared with the procedure described in Appendice A2.1 and the monolayers were produced with the procedure illustrated in Appendice A2.14.

The Au NPs monolayers were treated at 650°C in air for one hour and at 600°C in H_2(5%v/v Argon) for one hour in order to reduce the alteration of the Au NPs monolayer with the later treatments at high temperature in H_2(5%v/v Argon) atmosphere.

3.1.2.2 Graphene oxide deposition

GO was synthesized with a modified Hummer synthesis by Favaro et al. [13].

700µl of a solution 1mg/ml in DI water was deposited by spincoating on substrates of 1cmx2cm of Au NPs on quartz. The films were annealed at 70°C for few minutes to remove the solvent.

Film of GO were deposited on Silicon substrates with the same procedure.

Then the film have been progressively reduced with treatments of reduction for 15', 30', 45' minutes at 150°C, 250°C, 350°C, 500°C. The films reduced with any of these treatments are referred as <TT>x<tt>, with <TT> the temperature of treatment and <tt> the permanence at that temperature.

3.1.2.3 Film characterization and gas sensing measurement

The thin films have been characterized with UV/Vis and FTIR spectroscopy, X-ray diffraction analysis, Scanning Electron Microscopy and Atomic Force Microscopy, illustrated respectively in Appendix A1.7, A1.1, A1.1.2 and A1.6

The gas sensing tests have been performed at operating temperature (OT) of 150°C and 300°C toward H_2(10,000ppm), CO(10,000ppm), NO_2(1ppm). Two modes of gas sensing test have been conducted, the static and dynamic measures. The detailed description of the gas sensing set-up and modality of analysis are reported in A3.

3.1.3 Gold Nanoparticles monolayer characterization

The heat treatment of the Au NPs monolayer affects the shape and position of the LSPR peak as can be noticed in Figure 3.1.1. Both the annealing in air and the annealing in H_2(5% v/v Argon) lead to an increase in the size of the NPs, leading to a blue-shift of the LSPR that states an increase in the distance among nanoparticles with a reduction of the coupling of the LSPR effect among the particles[14] [15] .

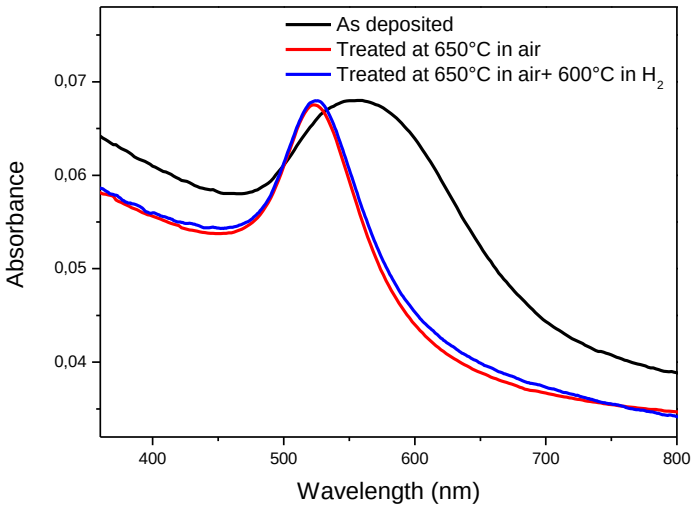

Figure 3.1.1 – Evolution of the plasmon peak of the gold NPs as deposited (black line), after a thermal treatment at 650°C for 1 hour and after treatment at 600°C in H_2(5%v/v Argon) flux for a 1 hour (red line).

The XRD analysis of the substrates with Au NPs shows a variation in size with the heat treatment as reported in Table 1. The size of NPs have been estimated with Scherrer equation[16] [17] , considering the particles as single crystals.

	Nanoparticles diameter (nm)
As deposited on substrates	10,6
After TT at 650°C	11,4
After TT at 600°C in H_2 flux	14,6

Table 1 – Mean diameter of the of Au NPs as deposited, after the thermal treatment at 650°C and after the treatment at 600°C in atmosphere of H_2(5%v/v), estimated from XRD pattern.

The effective size of the nanoparticles can be observed in the pictures acquired with SEM and shown in Figure 3.1.2. The nanoparticles as depositedhave a mean size of 13nm (Fig. 3.1.2a). The thermal treatments of stabilization of the Au NPs monolayer lead to the growth of NPs due to coalescence, which can be noticed in Fig. 3.1.2b. After the thermal treatments, the average diameter of the Au NPs is of 40nm. With the increase of the size of NPs, the distance between them is enlarged, causing to the blue-shift of the LSPR peak observe in Figure 3.1.1.

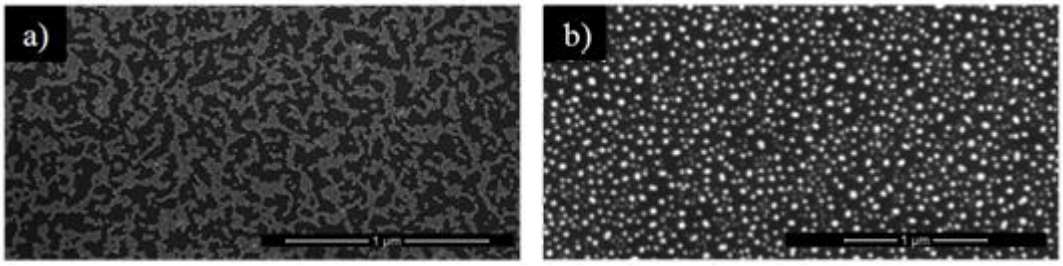

Figure 3.1.2 – SEM images of the monolayer of Au NPs a) as deposited and b) after the heat treatments at 650°C in air and 600°C in H_2(5%v/v).

3.1.4 Thin film characterization

The position of the LSPR peak is further affected by the deposition of the GO layer and the following treatments of reduction at different temperatures. The plasmon peak undergoes a red-shift once the GO is added on it due to the high refractive index of this material.

The reduction at 150°C provokes a further red-shift of the LSPR peak position, due to the rise in value of the index of refraction of the graphene oxide layer, caused by the increase in

interaction among the sheets with the removal of water molecules among the stack of GO[18] .

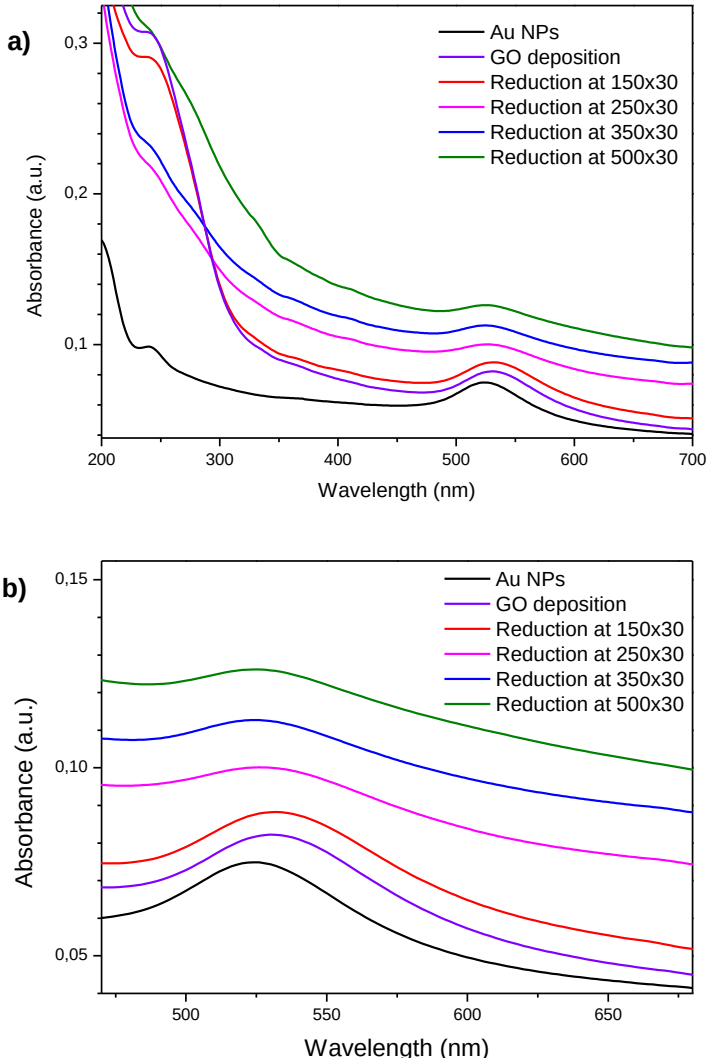

Figure 3.1.3 – a) Evolution of the absorbance of the films of GO and Au NPs and of b) the plasmon peak of the stabilized monolayer of gold nanoparticles after deposition of graphene oxide and the later treatments of reduction in H_2(5%v/v Argon) at increasing temperature.

The refractive index increases from a value of ~2 toward a value of ~2.25 with the removal of water molecules and becomes higher as the interlayer interactions are extended with reduction, with an intermediate value between the one of GO and bulk graphite (~3)[18] .

The subsequent treatments of reductions are conducted at higher temperature and coalescence phenomena of the Au NPs may occur in spite of the previous treatment to achieve a stability to the following treatment. Thus, an appreciable blue-shift (~5nm) of the LSPR peak of the Au NPs can be noticed in Figure 3.1.3b.

The difference in intensity of the absorbance for the transition $\pi \rightarrow \pi^*$ at 240nm and $\pi \rightarrow \sigma^*$ at 290nm may be ascribed to a non homogeneous film of rGO and so different cross sections of active material are met by the incident beam. With the reduction treatments the peak at 240nm shifts toward the visible, becoming a shoulder at 275nm for GO treated at 500°C. The shift of the peak related to the $\pi \rightarrow \pi^*$ transition underlines an increase in the conjugation of the sp^2 domains.

Figure 3.1.4 shows the effects of the reducing treatments on the stacking distance among the GO layer.

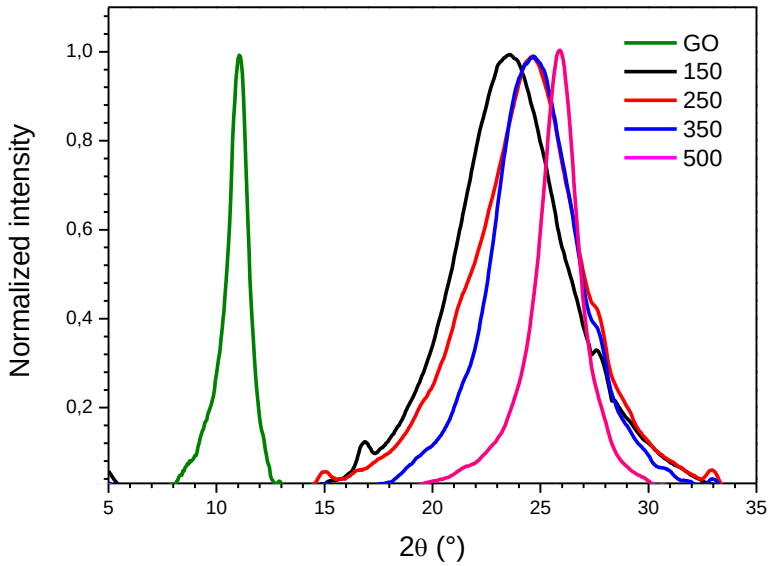

Figure 3.1.4 – XRD patterns of graphene oxide as deposited and after the reducing treatments in H_2(5%v/v Argon) at increasing temperature. The intensity of the diffraction peaks has been normalized to better visualize the shifts.

The peak of the (002) plane moves from 11,10° to 23,44° with the reduction at 150°C. The following reducing treatments approaches the position of the (002) peak narrower to that relative to graphite, at 26,63° (JCPDS No. 75-2078) for each step of reduction.

The decrease in spacing at 150°C can be related to the removal of residual water molecules among the sheets. Table 2 reports the position of (002) peak and relative stacking of rGO with the different treatments. The further shifts of the (002) peak suggest the removal of the functional groups and eventual remaining water molecules[18].

Temperature of treatment (°C)	2θ (°)	Stack distance (Å)
RT	11,10	8,0
150	23,45	3,8
250	24,49	3,6
350	24,72	3,6
500	25,84	3,4

Table 3.2 – Variation of the stacking distance with the temperature of reduction

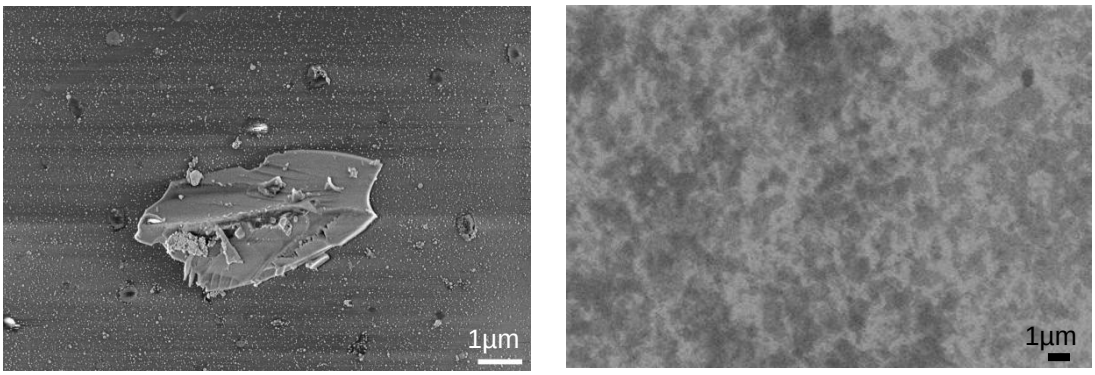

Figure 3.1.5 –SEM image of a) an isolated flake of graphene oxide and Au NPs; b) thin film of GO.

The morphology of the rGO is depicted in Figure 3.1.5. The GO forms stacking covering the monolayer of Au NPs as can be seen for the isolated flake in Figure 3.1.5a. The GO sheets have size ranging from hundreds of nanometers to few microns and gives a good coverage of the surface., as shown in Figure 3.1.5b.

3.1.4.1 Characterization of thin films reduced at 150°C

The treatment of reduction at 150°C leads to a partial desorption of most of the water trapped among the sheets with the dumping of the peak at 1424cm^{-1} and ~3200cm^{-1}, as can be noted from the FTIR spectra reported in Figure 3.1.6. The presence of adsorbed water after the treatments can be ascribed to the reaction of H_2 with hydroxyl and epoxies resulting in the formation of water molecules[10] .

The increase in the reduction period leads to a stronger reduction, with the rise of the peak relative to the aromatic carbon (~1587cm^{-1}). This is accompanied by a strong reduction of hydroxyl groups and a slighter decrease in epoxy and ether species(~1230cm^{-1}). The

carbonyls groups don't appear significantly affected by the reduction treatments at 150°C, independently by the reduction time. A weak shoulder at ~2800cm^{-1} can be attributed to methyl groups as a minor part of the sp^3 defects in the basal plane of GO.

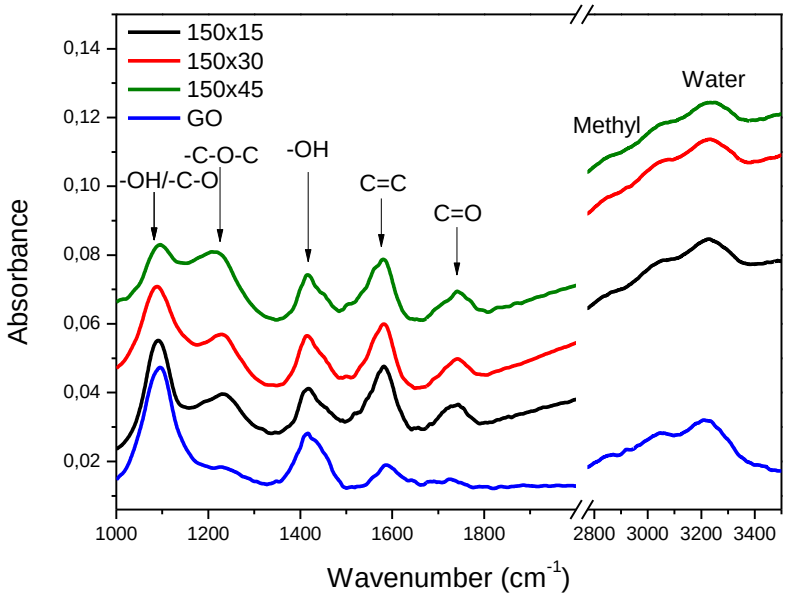

Figure 3.1.6 – FTIR plots of graphene oxide reduced at 150°C for 15'(black line), 30'(red line), 45' (green line) and not treated GO(blue line) as reference.

To evaluate the influence of the chemical structure on the optical gas sensing properties the Optical Absorbance Change (OAC) parameter is considered. It is defined as the difference between absorbance during gas exposure and absorbance in air ($OAC = Abs_{Gas} - Abs_{Air}$) and is an useful tool to a clear visualization of how the target gases affect the optical properties of the films.

The modification in chemical structures are reflected in a sensitization of the films toward gases, as can be seen in Figure 3.1.6. In particular a longer treatment of reduction is associated to an enhanced response toward H_2(1%). This is expressed by the blue-shift of the LSPR peak under exposure to hydrogen, visible in Fig.3.1.6d, and is reflected in the appearance in the OAC plot relative to H_2(1%) of a peak and a valley in proximity of the position of the LSPR peak of the Au NPs.

The interaction of CO and NO_2 and the nanostructures didn't produce a noticeable variation in absorbance.

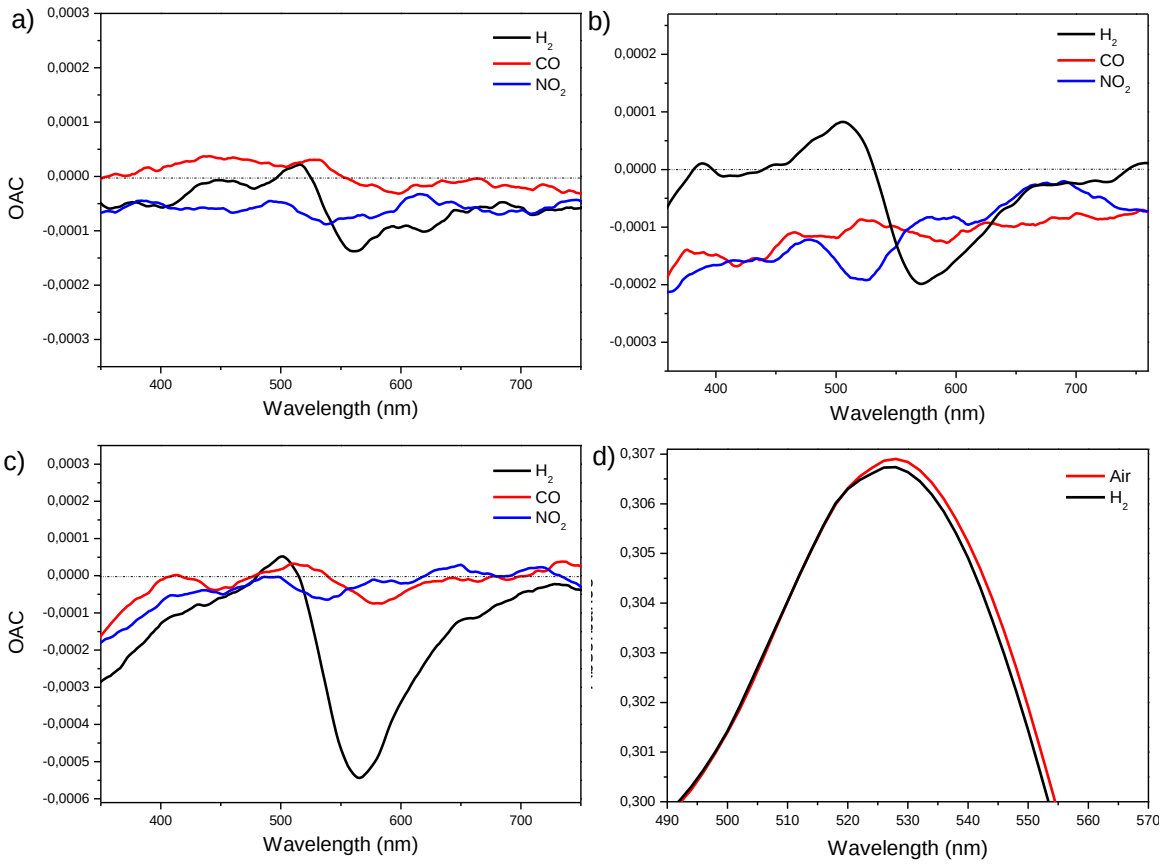

Figure 3.1.7 – a) OAC plots of the sample 150x15 at OT=100°C; b) OAC plots of the sample 150x30 at OT=100°C; c) OAC plots of the sample 150x45 at OT=100°C; d) Absorbance plot of the LSPR peak of the Au NPs in the film150x45 in air and H_2(1%) .

The time resolved scans have been acquired at the wavelengths where the strongest difference in absorbance values was observed in the OAC plots due to exposure to the gas analyte. The three sensors have been tested at the negative peaks in the OAC plots at 550nm for150x15 and 570nm for 150x30 and 150x45.

Figure 3.1.8 shows the dynamic resolved scans of the films toward the gas analyte. The responses toward H_2(1%v/v) becomes sharper with a more prolonged treatment.

This is stressed by the reduction of the response time: 195s and for a change in relative absorbance value of $6*10^{-4}$ for the sample 150x15, 103s with a change in relative absorbance of $4*10^{-4}$ for 150x30, 67s with a change in relative absorbance of $5*10^{-4}$ for sample 150x45.

The increase in reduction time leads to a more reduced structure, as expected with resulting improvement in optical gas sensing for rGO on Au NPs. The longer treatment reduces the

response period, giving sharper variation. The variation in absorbance is similar for the three samples.

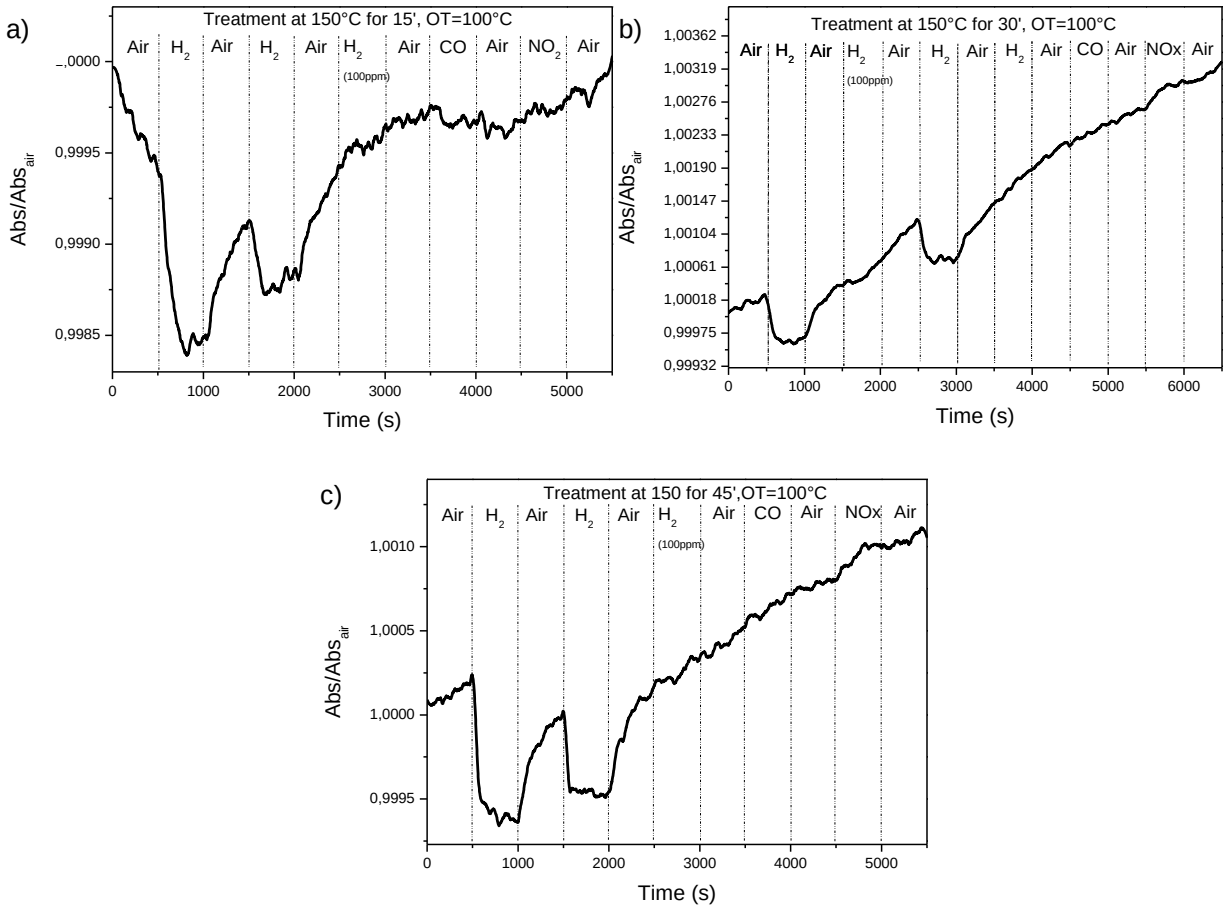

Figure 3.1.8 –Time resolved scans at OT= 100°C of the films of GO on Au NPs a) treated at 150°C for 15' at λ=550nm; b) treated at 150°C for 30' at λ=570nm; c) treated at 150°C for 45' at λ=570nm.

3.1.4.2 Characterization of thin films reduced at 250°C

The comparison of the FTIR spectra obtained after the treatments of reduction at 250°C and the structure of the 150x45 is represented in Figure 3.1.9.

The treatments of reduction at 250°C leads to the complete removal of adsorbed water, with the disappearance of the peaks at ~1424cm^{-1} and ~3200cm^{-1}. This is accompanied by a strong loss of hydroxyls (~1090cm^{-1}),a reduction of epoxies (~1220cm^{-1}) and carbonyls (~1750cm^{-1}) and a subsequent increment of aromatic carbon.

The time of reduction doesn't influence remarkably the structure: slight differences in the height of the hydroxyls groups can be noted . The longer treatments with H_2 may lead to the reaction of hydrogen with a larger number of sites of epoxies and carbonyls, causing the formation of water and hydroxyl functionalities [10] .

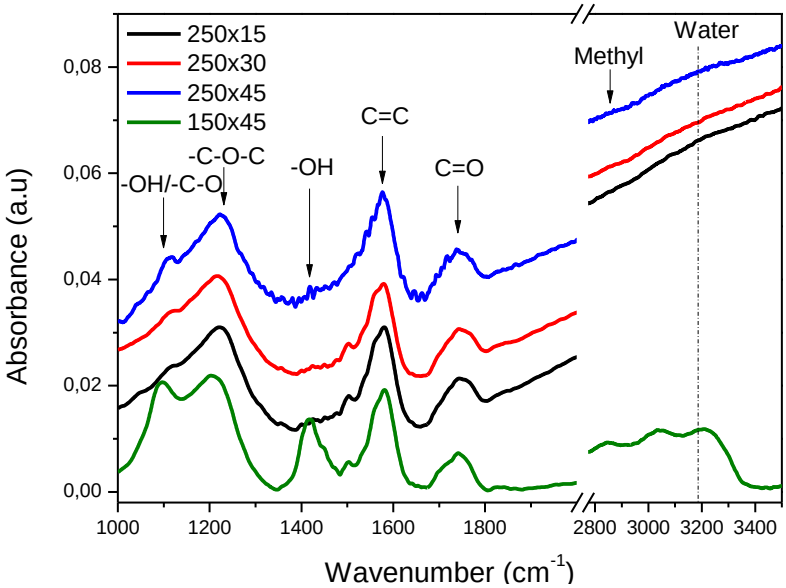

Figure 3.1.9 – FTIR plots of graphene oxide reduced at 250°C for 15'(black line), 30'(red line), 45' (blue line) and graphene oxide reduced at 150°C for 45'(green line), reported as benchmark.

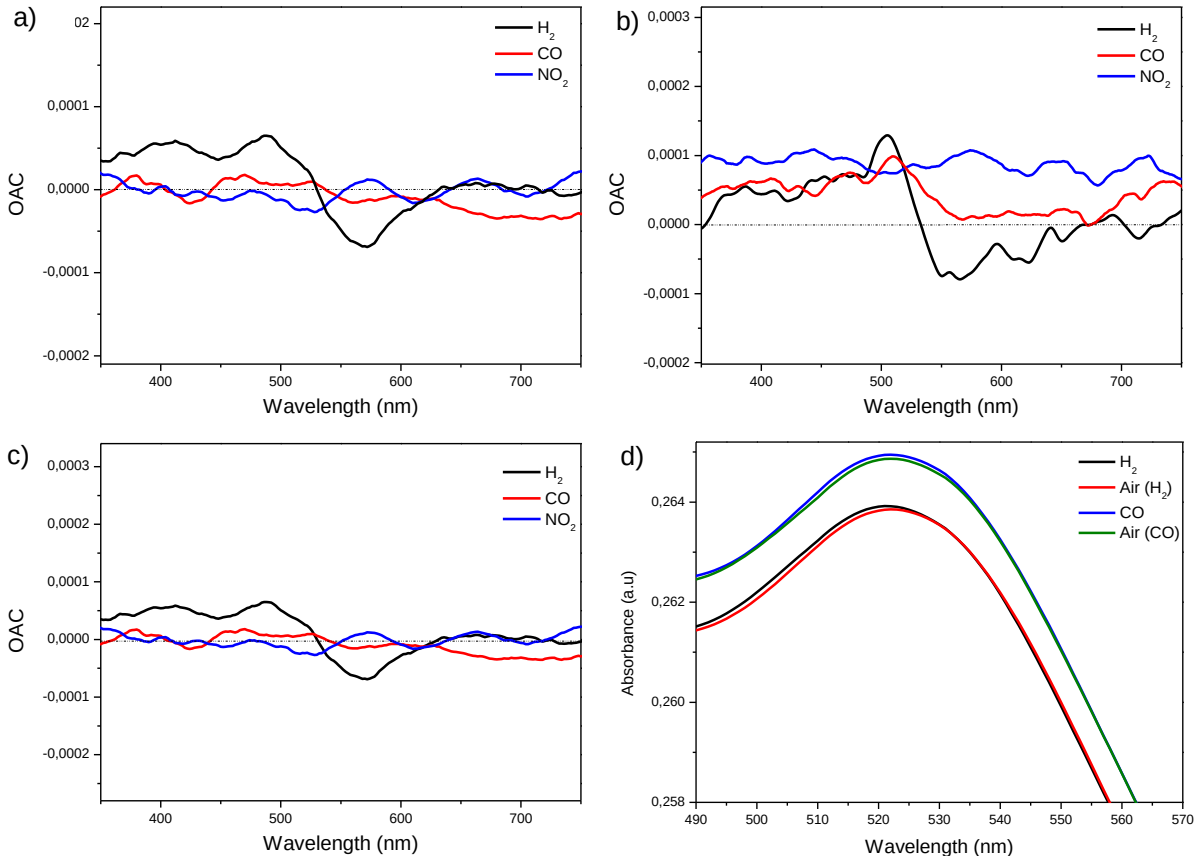

Figure 3.1.10 - a) OAC plots of the sample 250x15 at OT=150°C; b) OAC plots of the sample 250x30 at OT=150°C; c) OAC plots of the sample 250x45 at OT=150°C; d) Absorbance plot of the LSPR peak of the Au NPs in the film250x30 at 150°C in air, in H_2(1%),in CO(1%) and air. The last two plots are slightly stacked from the previous for a better visualization.

Figure 3.1.10 illustrates the OAC plots of the samples treated at 250°C. The reduction at 250°C leads to a variation in absorbance toward H_2(1%).

The sample at 250x30 displays a sharper variation toward hydrogen and a mild response also toward CO related to a remarkable blue-shift and a slight shift of the LSPR peak of Au NPs respectively in H_2 and CO atmospheres, visible in Fig 3.1.10d. A weak response to NO_2 can be noted in Figure 3.1.10c.

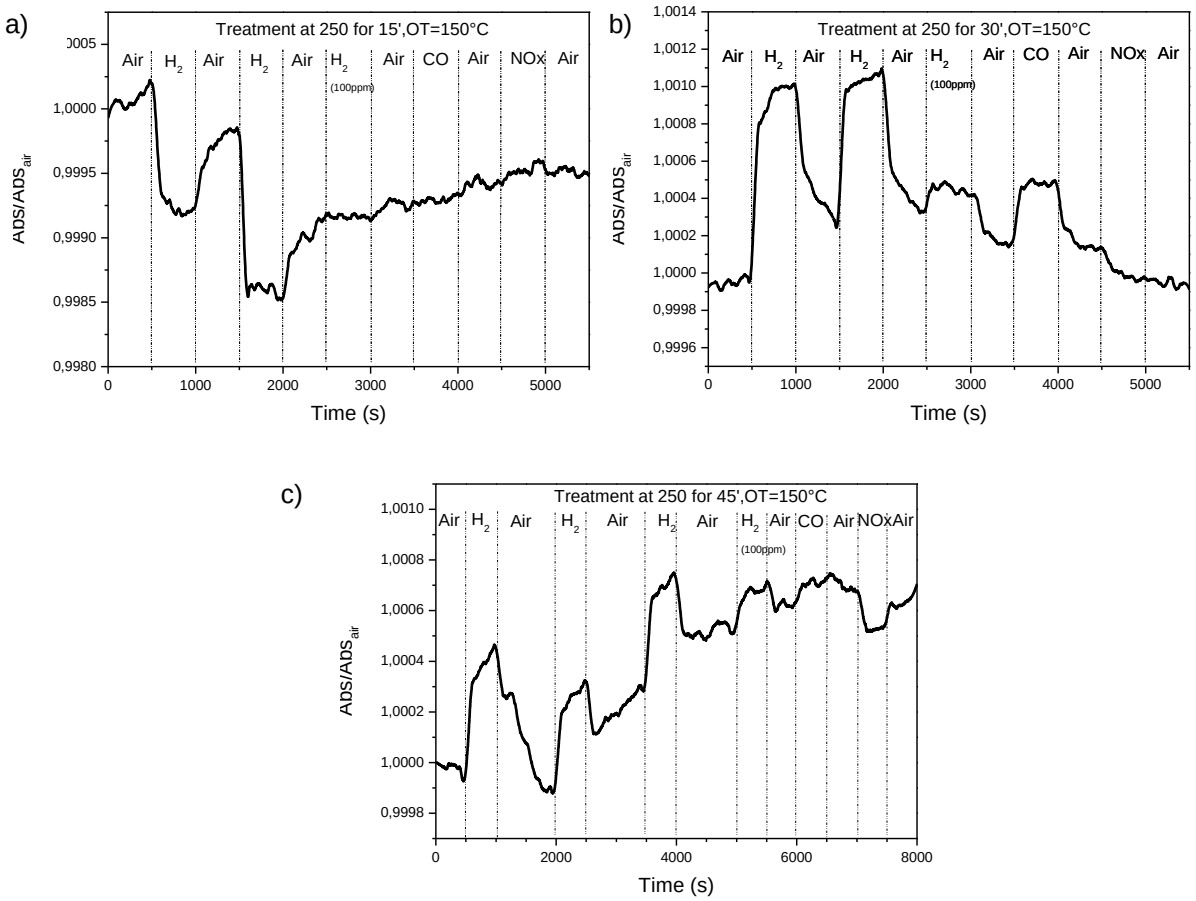

Figure 3.1.11 - Time resolved scans at OT= 150°C of the film of GO on Au NPs at a) treated at 250°C for 15' at λ=560nm; b) treated at 250°C for 30' λ=510nm; c) treated at 250°C for 45' at λ=510nm.

Figure 3.1.11 shows the dynamic scans of the films treated at 250°C.

The dynamic tests confirm what observed with OAC plots: an increase in reduction improves the optical sensing performance toward H_2(1%v/v). Indeed, the dynamic response becomes more relevant and sharper than the one displayed by the sensors treated at 150°C.

It is noticed that a longer period of treatment provides a finer sensitivity to H_2, making even possible the detection of this gas in concentration of 100 ppm.

250x15 is tested at λ=560nm, meanwhile 250x30 and 250x45 are at λ=510nm. At these wavelengths the stronger variations in absorbance are observed in the OAC plots.

The responses are of $1*10^{-3}$ in 84s for 250x15, $9*10^{-4}$ in121s for 250x30 and $4*10^{-4}$ in 190s for 250x45. The nanocomposites are responsive toward H_2(100ppm) with a variation of $1*10^{-4}$ in 41s for 250x30 and of $2*10^{-4}$ in 211s for 250x45.

250x30 and 250x45 are weakly responsive to CO(1%v/v) and NO_2(1ppm). The slight increase in hydroxyls in the structure of rGO may play an important role in the attraction of

CO and NO_2, due to the establishment of weak interaction between the functional oxidized groups and the polar gas molecules.

At the same time it is observed a variation in the structure with a diminution of intensity of the peak of the hydroxyl groups at increasing time of reduction at 250°C.

3.1.4.3 Characterization of thin films reduced at 350°C

Figure 3.1.12 displays the chemical structure obtained by the samples treated at 350°C with FTIR investigation.

The reduction in hydrogen at 350°C generates an increase of the aromatic carbon peak compared to those of the oxidized groups.

Little variation can be noted in the FTIR plots of 350x30 and 350x45 compared to the plot of 350x15: a weak increase of hydroxyl(~1120cm^{-1}) groups is accompanied by a slight increase in aromatic carbon (~1580cm^{-1}).

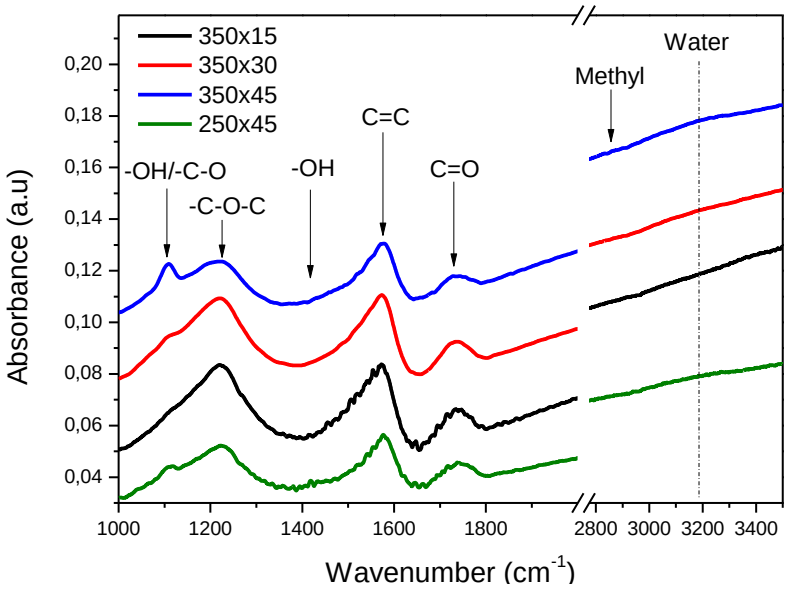

Figure 3.1.12 – FTIR plots of graphene oxide reduced at 350°C for 15'(black line), 30'(red line), 45' (blue line) and graphene oxide treated at 250°C for 45'(green line), reported as benchmark.

3.1.4.3.1 Gas sensing tests at 150°C OT

In Figure 3.1.13, the nanocomposites display similar change in absorbance for prolonged exposure to oxidizing/reducing gases. H_2(1%) causes a strong variation in absorbance which is evident for all the films and is clearly represented in the relative OAC plots as reported in Figure 3.1.13. A weak variation in optical absorbance, caused by weak blue-shift of the LSPR peak of Au NPs, is observed also toward H_2(100ppm), in Figure 3.1.13d and is stressed in the OAC plots of H_2(100ppm) in Figure 3.1.13. Instead, the entity of the position change of the LSPR peak with the exposure to the higher concentration, H_2(1%) is conspicuous.

CO(1%) and NO_2(1ppm) don't significantly alter the optical properties of the films.

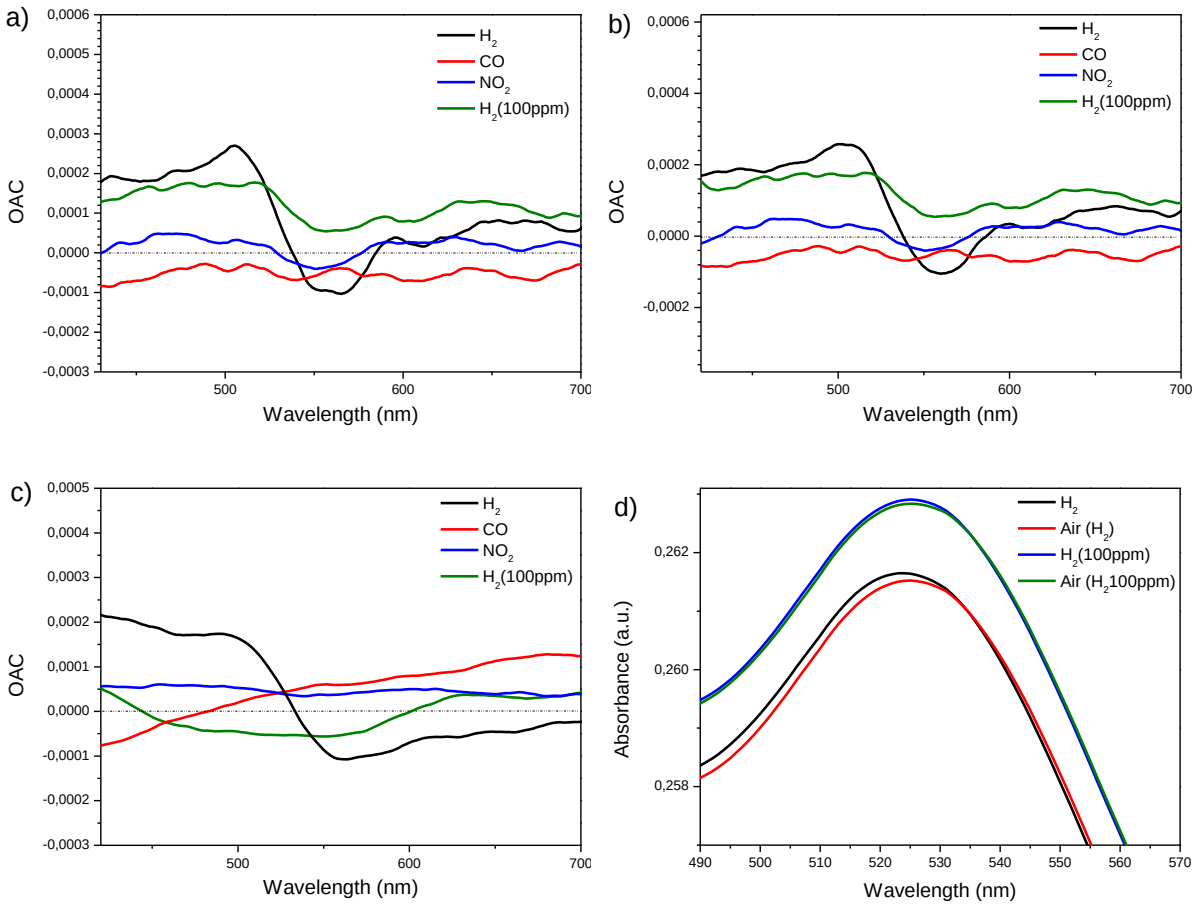

Figure 3.1.13 - a) OAC plots of the sample 350x15 at OT=150°C; b) OAC plots of the sample 350x30 at OT=150°C; c) OAC plots of the sample 350x45 at OT=150°C; d) Absorbance plot of the LSPR peak of the Au NPs at OT=150°C of the film 350x30 in air and H_2(1%) and H_2 (100ppm) and air slightly stacked from the previous for a better visualization.

The dynamic scans of the films treated at 350°C are reported in Figure 3.1.14.

From OAC plots we draw two possible wavelengths for the time resolved scans: λ=500nm, where the samples detect multiple H_2 concentrations and varieties of gases and λ=560nm, where the difference in absorbance is maximized due to exposure to H_2(1%v/v), but the other gases don't induce a remarkable variation in absorbance, as can be noted in Figure 3.1.13.

The dynamic scans outline the considerations drawn from OAC plots.

The strongest response to H_2 is pursued at λ=560nm with a value in relative absorbance of$1*10^{-3}$, but poor results toward H_2(100ppm) and CO(1%) are obtained.

Setting the wavelength at 500nm, a more net response to H_2(100ppm) is obtained.

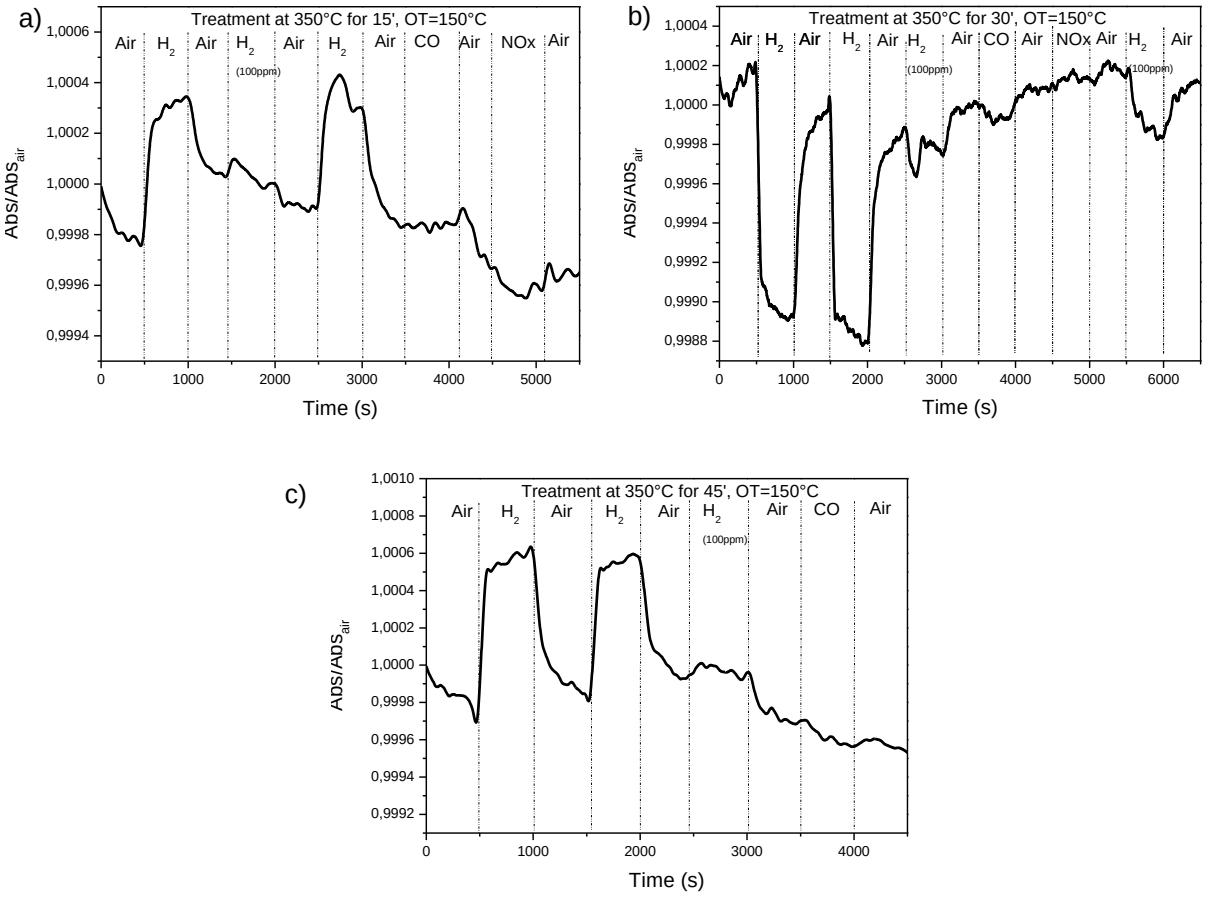

Figure 3.1.14 - Time resolved scans OT= 150°C and of the film of GO on Au NPs a) treated at 350°C for 15' at λ=510nm; b) treated at 350°C for 30' at λ=560nm; c) treated at 350°C for 45' at λ=500nm.

The samples show faster responses to H_2 than the films treated at 250°C. The response becomes more rapid with a longer treatment of reduction, but the change in relative absorbance is similar in intensity to what obtained at 250°C. These intensities appear to be dependent on the wavelength chosen for dynamic tests as mentioned above.

The film treated at 350°C for 45 minutes lose the mild sensitivity toward CO(1%v/v), $0.8*10^{-4}$, and NO_2(1ppm) $0.8*10^{-4}$, that was present in 350x15 and 350x30.

The step at 350°C reduces the further the carboxyl and hydroxyl groups, a correlation between this groups and the adsorption of CO and NO_2 may exist.

3.1.4.3.2 Gas sensing tests at 250°C OT

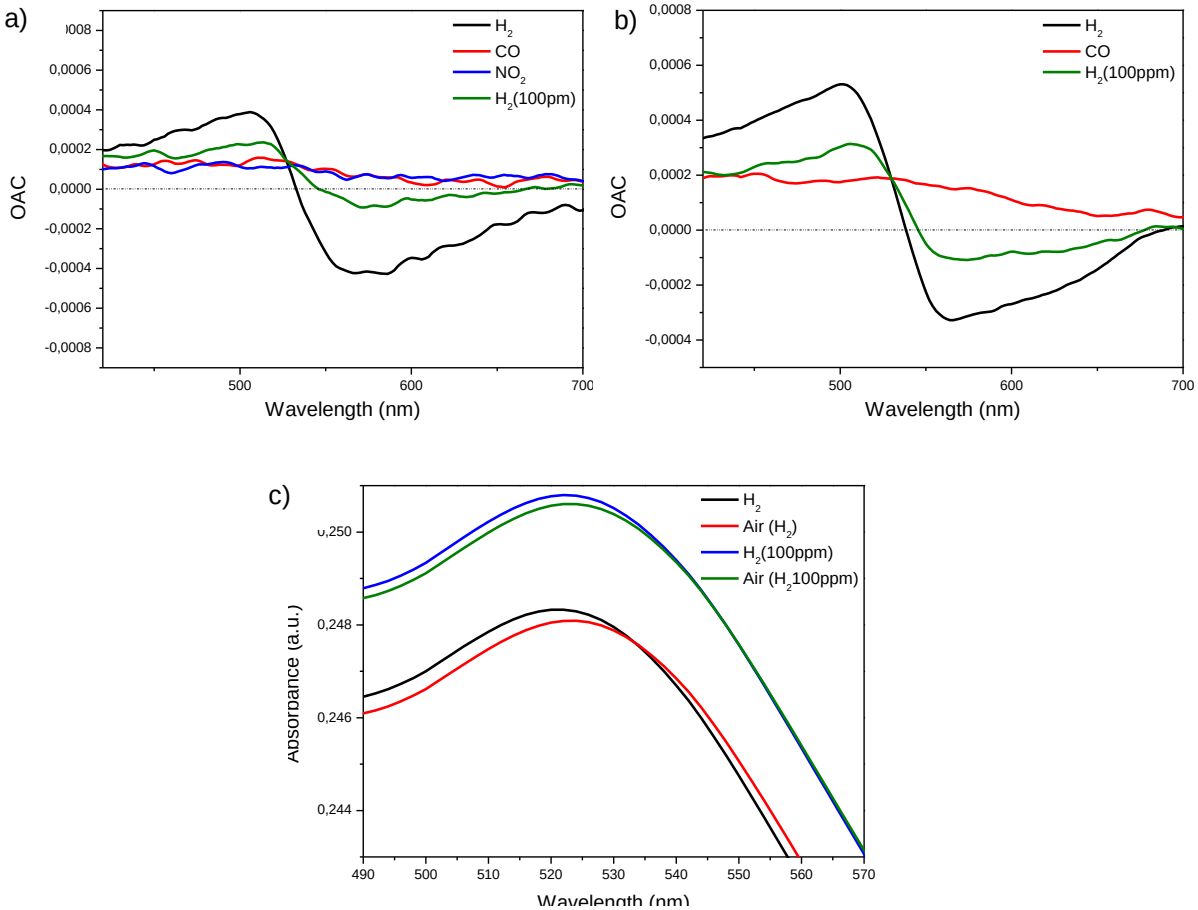

Figure 3.1.15 - a) OAC plots of the sample 350x15 at OT=250°C; b) OAC plots of the sample 350x30 at OT=250°C; c) Absorbance plots of the LSPR peak of the Au NPs in the film 500x15 in air and H_2(1%) and H_2 (100ppm) at OT=250°C.

The samples 350x30 and 350x45 have also been tested at 250°C. The results of the static tests are displayed in Figure 3.1.15.

The OAC plots related to H_2(1%) are similar in shape to the analogous recorded at 150°C, but the intensity of the peaks and dips is sensibly higher indicating a stronger blue-shift of the LSPR peak of metallic NPs also for the lower concentration,H_2(100ppm).

CO and NO_2 are not observed with the OAC plots.

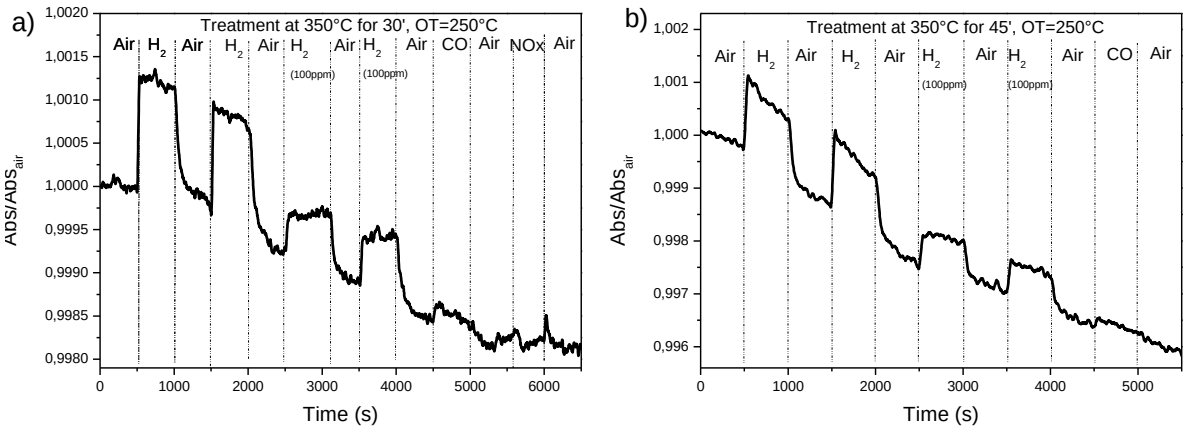

Figure 3.1.16 - Time resolved scans OT= 250°C and of the film of GO on Au NPs a) treated at 350°C for 15' at λ=500nm; b) treated at 350°C for 30' at λ=500nm.

Raising the temperature of the sensing tests at 250°C produces superior performance than what achieved at operating temperature of 150°C also in dynamic tests, see Figure 3.1.16.

In fact, the response to H_2 (1%v/v) gives $1{,}11*10^{-3}$ in 43s for 350x30 and in 33s for 350x45. The response to H_2(100ppm) is enhanced too with a variation in analysis property of $5*10^{-4}$ in39s for 350x45, comparable to the results toward H_2(1%) obtained at 150°C OT.

The recovery steps are faster and sharper than their counterpart at OT=150°C. The higher temperature can ease the desorption of the gases from the surface and their replacement with oxygen.

A faint response to CO was observed (~ $1*10^{-4}$) without a clear recovery step switching back to air. Similar results were obtained with 350x30 toward NO_2(1ppm), meanwhile 350x45 was not responsive to these two gases.

3.1.4.4 Characterization of thin films reduced at 500°C

Figure 3.1.17 compares the structure obtained at 500°C for 45' with those obtained at 500°C for different period (15', 30',45') in H_2(5%v/v Argon). The plots of FTIR spectra appear similar among them, except for an increase in hydroxyls at 500x30. The treatments at 500°C don't appear to enhance the reduction of the GO beyond what gained at 350°C.

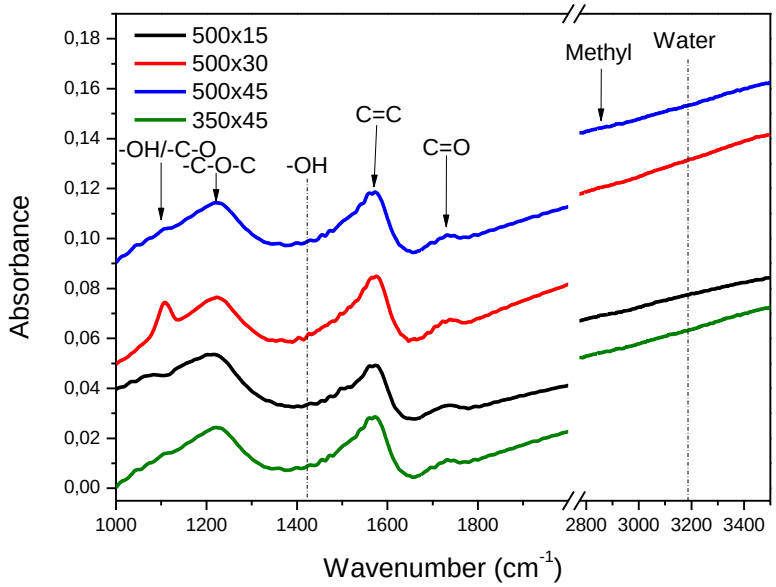

Figure 3.1.17 - FTIR plots of graphene oxide reduced at 500°C for 15'(black line), 30'(red line), 45' (blue line) and graphene oxide treated at 350°C for 45'(green line), reported as benchmark.

3.1.4.4.1 Gas sensing tests at 150°C

The samples treated at 500°C present similar behavior to the analogous treated at 350°C. The exposure to H_2(1%v/v) leads to strong change in optical properties of the films.

500x45 present a more marked dip in the OAC plot than those exhibited by 500x15 and 500x30.

Similar trend is observed with the OAC plots of the films toward H_2(100ppm).

The samples have been tested at 300°C and have been degraded so 500x45 was freshly prepared. The Au NPs monolayer is not affected by the repeated cycles of thermal treatments and presents a stronger LSPR absorbance peak. Figure 3.1.3 shows a dumping of intensity of LSPR peaks with the repeating of high temperature cycles. The strong reduction and the higher coverage of Au NPs may cause the stronger variation

of film 500x45 toward H_2(1%). The absorbance plots of the peak of the Au NPs of 500x15 (Figure 3.1.18d) show the change in position of the LSPR peak under different concentration of hydrogen and under CO(1%) fluxing. The change in absorbance in CO atmosphere is weak. Differently, in H_2(100ppm) the LSPR peak of 500x15 presents a discrete blue-shift, that is converted in an appreciable peak and valley in the OAC plots.

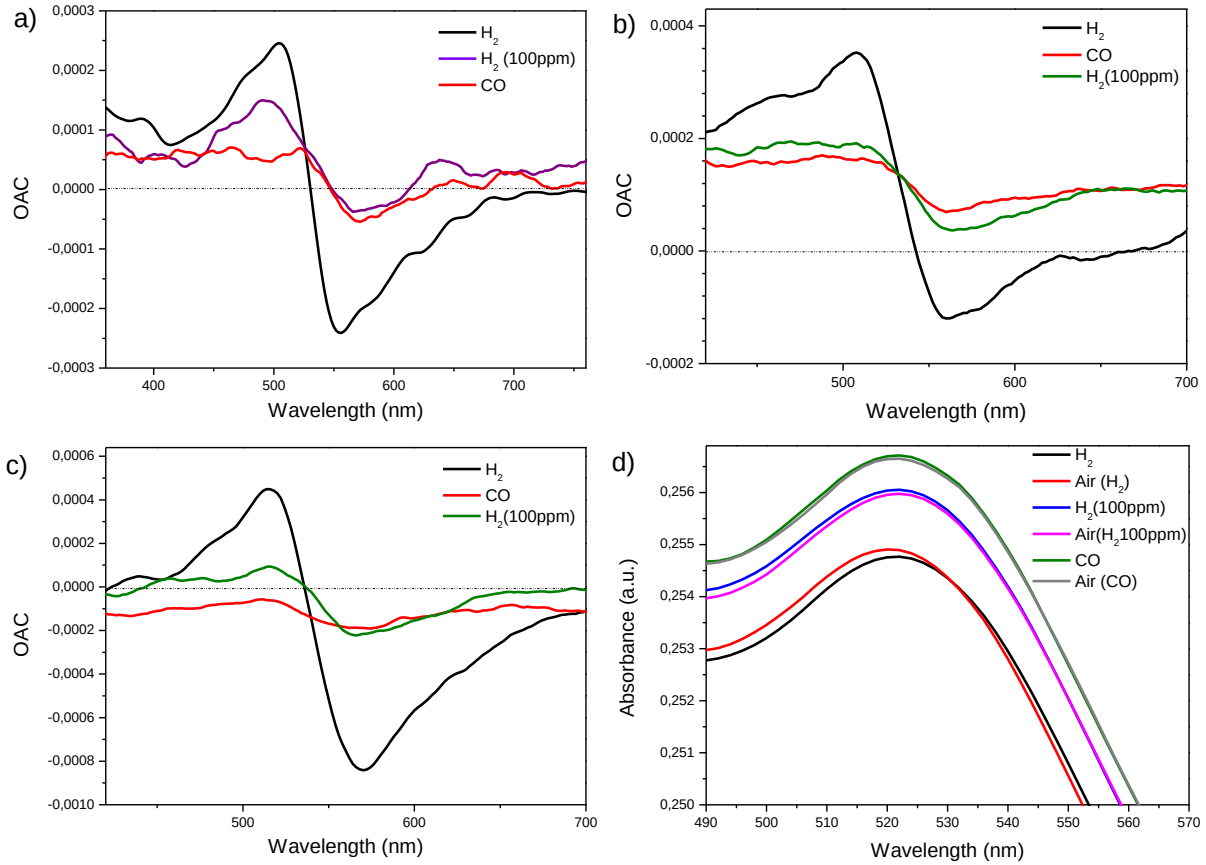

Figure 3.1.18 - a) OAC plots of the sample 500x15 at OT=150°C; b) OAC plots of the sample 500x30 at OT=150°C;) OAC plots of the sample 500x45 at OT=150°C; d) absorbance plots of the LSPR peak of the Au NPs in the film 500x30 in air and H_2(1%), H_2 (100ppm) and CO(1%), at OT=300°C

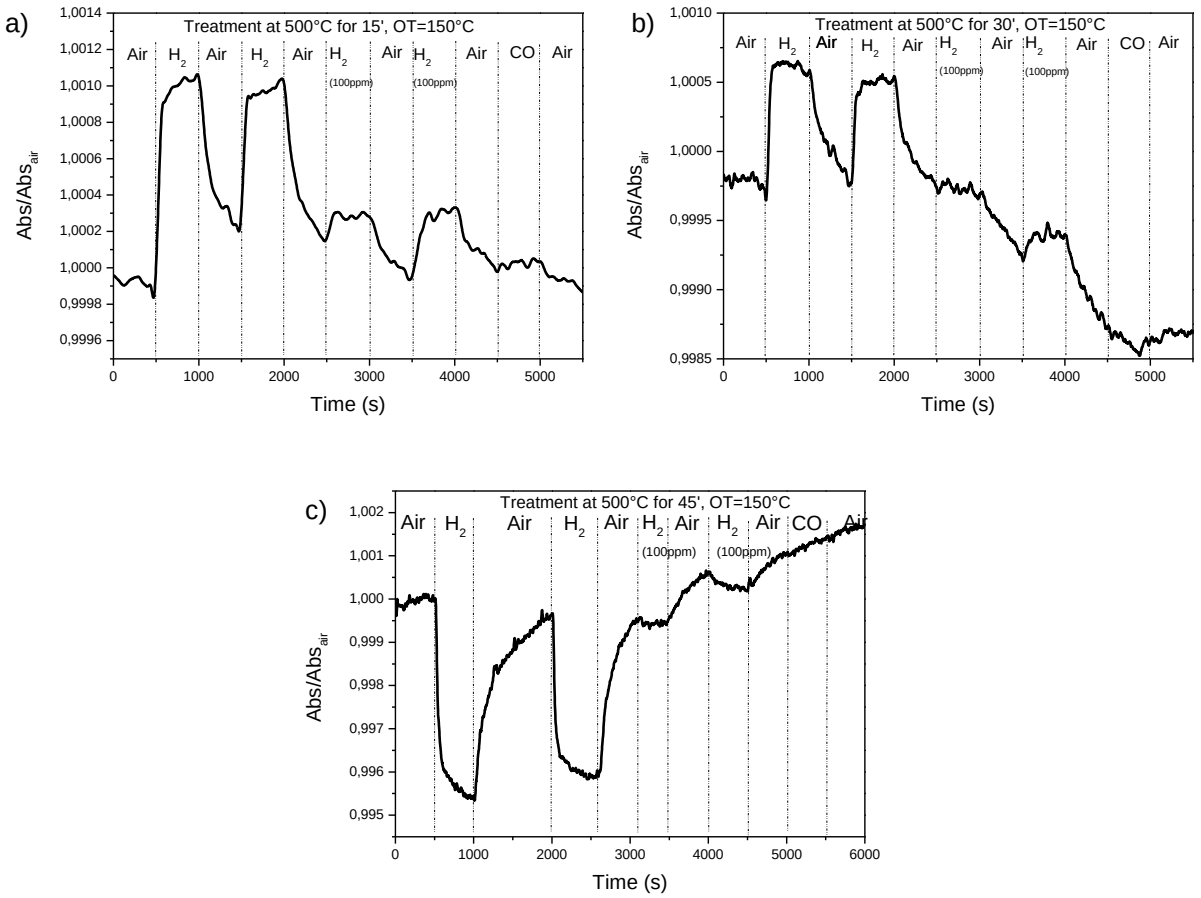

Figure 3.1.19 - Time resolved scans at OT= 150°C and of the film of GO on Au NPs a) treated at 500°C for 15' at λ=500nm; b) treated at 500°C for 30' at λ=500nm; c) treated at 500°C for 45' at λ=560nm.

Figure 3.1.19 illustrates the dynamic tests at 150°C of the samples treated at 500°C.

The sensing tests carried on 500x15 and 500x30 present similar results to the performance of 350x45. The change in relative optical absorbance is of $8*10^{-4}$ in 52s for 500x15 and 82s for 500x30.

500x15 showed an increase in variation under atmosphere of H_2(100ppm) with a value of $3*10^{-4}$ in 157s.

The performance of 500x30 toward H_2(100ppm) are not so brilliant and a strong drift can be recognized.

The best results were achieved with 500x45 with a large variation in relative absorbance, with $3*10^{-3}$ in 79s.

On the contrary, 500x45 appears less performing toward H_2(100ppm) with a variation of

No response was achieved with the films toward CO(1%). The lower performance can be related to the different wavelength at which the dynamic test was carried for such sensor.

3.1.4.4.2 Gas sensing tests at 300°C

As reported in Figure 3.1.20, the variation toward H_2(1%) are more pronounced at 300°C OT. The blue-shift of the LSPR peak is more intense, see Fig. 3.20d.

The OAC plots of H_2(1%) present peaks at λ=500nm and a dips at λ=560nm remarking a strong variation in optical absorbance for the films. The same peaks, but less intense are clearly visible for H_2(100ppm) for all the three films.

In Figure 3.1.20d, the absorbance plots of the film 500x45 in CO(1%) shows the poor sensing properties toward this gas of the nanostructures treated at 500°C.

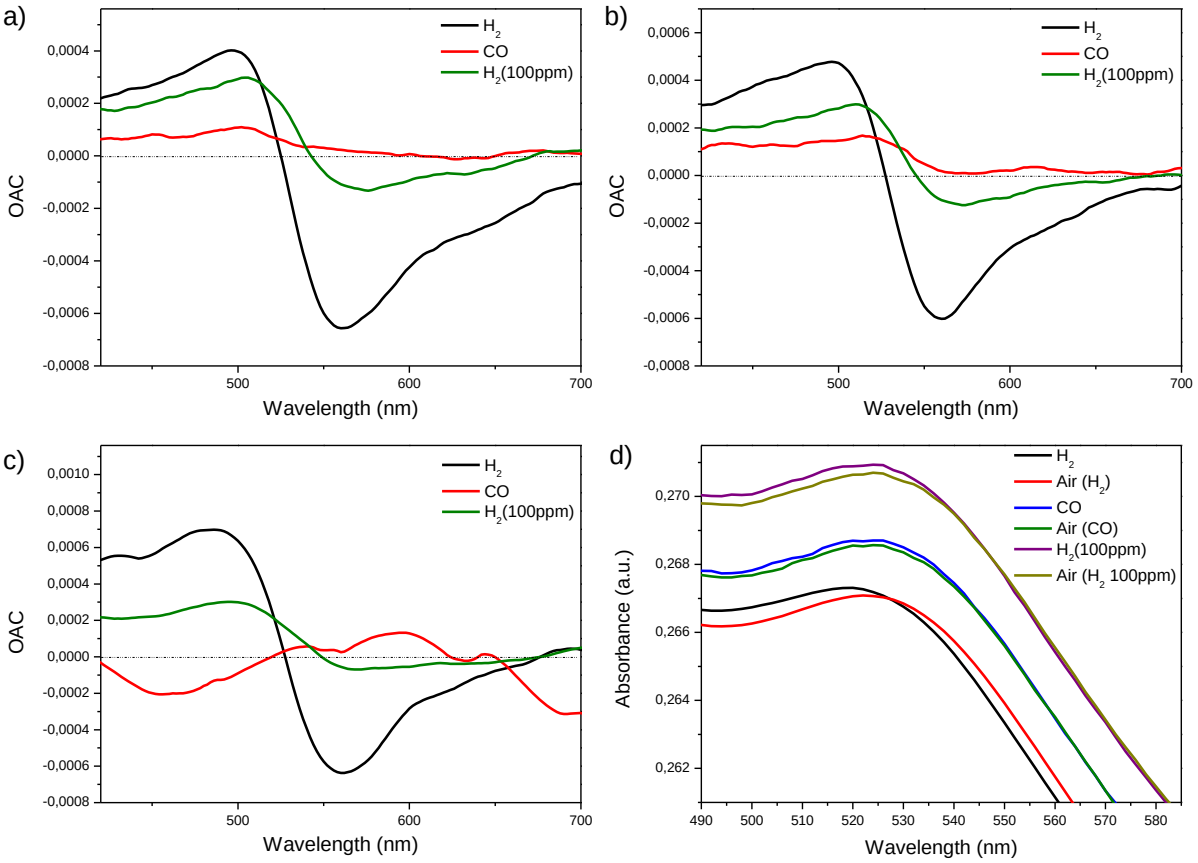

Figure 3.1.20 - a) OAC plots of the sample 500x15 at OT=300°C; b) OAC plots of the sample 500x30 at OT=300°C; c) OAC plots of the sample 500x45 at OT=300°C.

In Figure 3.1.21, the dynamic sensing tests at higher operating temperature report better performances toward H_2 gas in both the concentrations of analysis: the responses to H_2(1%v/v) are of $1.3*10^{-3}$ in 38s for both 500x15 and 500x30.

The higher OT plays a positive action also for the detection of H_2(100ppm) with a variation of relative absorbance of $6*10^{-4}$.

The sample 500x45 was tested at a wavelength corresponding to the dip in the OAC plot of H_2(1%v/v). The higher coverage of the surface with Au NPs and the different wavelength of analysis induce a sensible increase in performance of the sample. The variation of relative absorbance are of $1.2*10^{-2}$ in 60s and $3*10^{-3}$ toward respectively H_2(1%) and H_2(100ppm), an order of magnitude superior than what achieved.

All the sample are not affected by exposure to CO(1%).

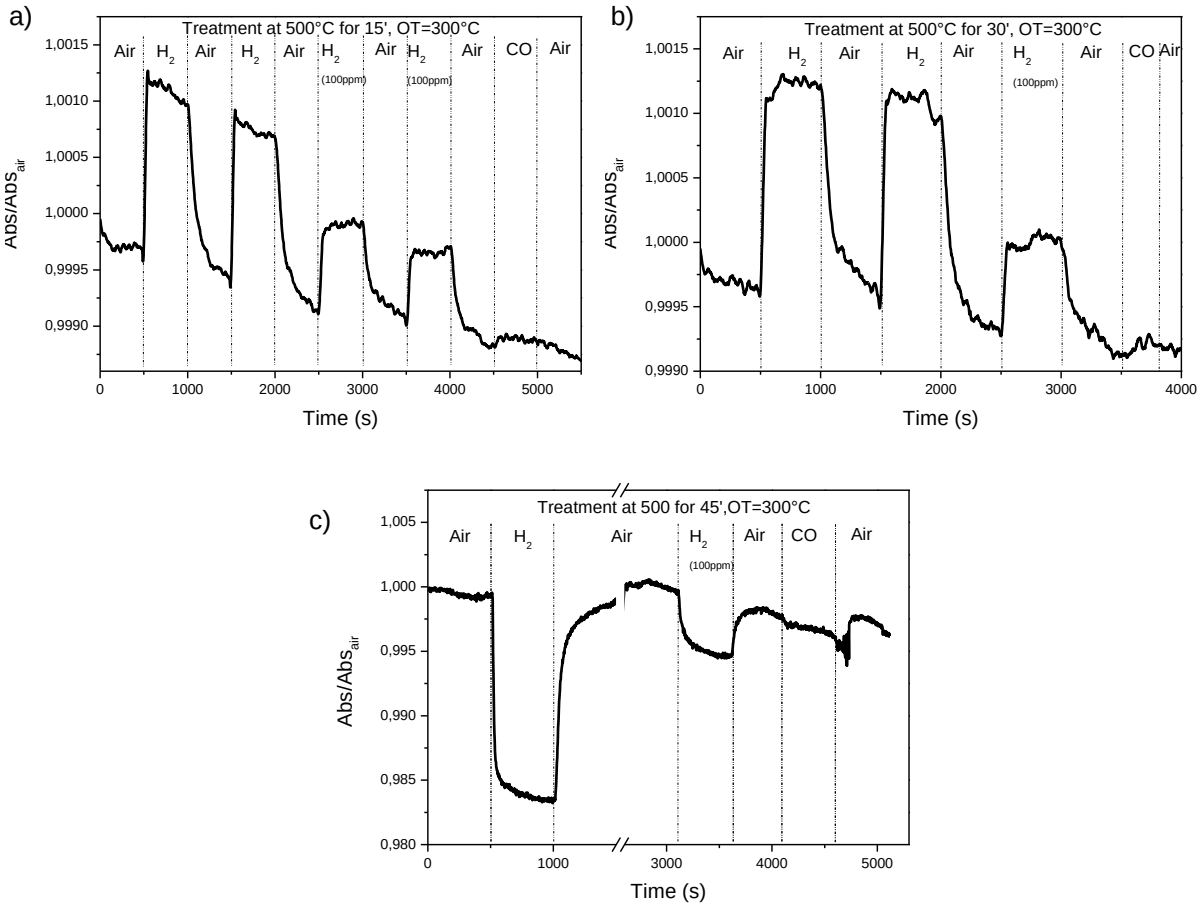

Figure 3.1.21 - Time resolved scans at OT= 300°C and of the film of GO on Au NPs a) treated at 500°C for 15' at λ=500nm; b) treated at 500°C for 30' at λ=500nm; c) treated at 500°C for 45' at λ=560nm.

3.1.4.5 Reduction of GO and H_2 gas sensing

The evolution of the chemical structure as a function of the temperature of reduction is portrayed in Figure 3.1.22 As evidenced above, changes in chemical structure of rGO can be seen varying the length of the treatments, but the chemical structure is more sensitive to the different temperature profiles of reduction.

In Table 3.3 the areas of the peaks of hydroxyl (~1095cm^{-1}), epoxy (~1230cm^{-1}), carbonyl/carboxyl groups (~1730cm^{-1}), adsorbed water (~1424cm^{-1}) and aromatic carbon (~1587cm^{-1}) are reported as a ratio C_f/C_{Ar} where C_f is the area relative to the specific functional group f and C_{Ar} the area of the aromatic carbon.

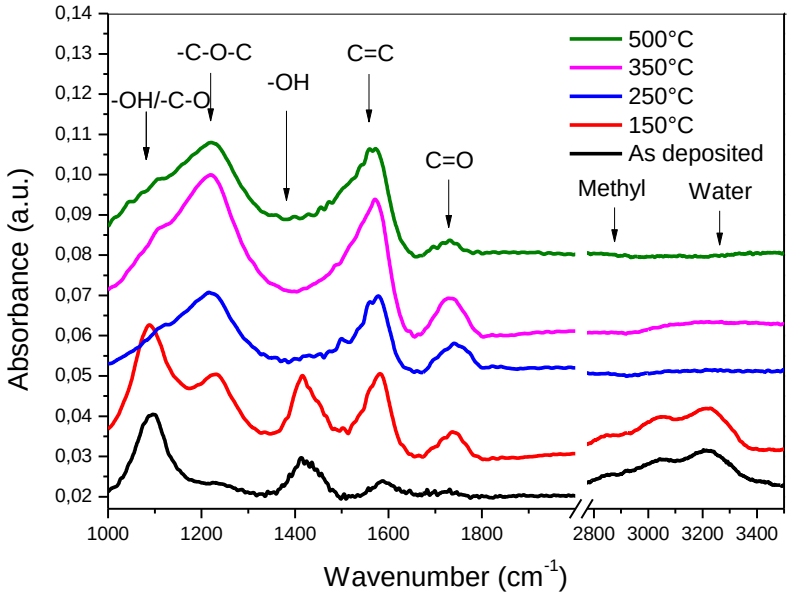

Figure 3.1.22 – FTIR plots of graphene oxide after the treatments at different temperatures.

	GO	150	250	350	500
C-OH	9,23	4,66	1,04	0,76	0,54
C-O-C-	3,86	2,71	1,35	1,21	0,93
H-OH	2,85	0,78	0,07	---	---
-C=C-	1	1	1	1	1
-C=O	0,40	0, 44	0,32	0,23	0,09

Table 3.3 – Presence of functional groups related to aromatic carbon obtained from the ratio C_f/C_{Ar} where C_f is the area relative to the specific functional group f and C_{Ar} the area of the aromatic carbon.

A general reduction of the functional groups is achieved with the reduction treatment at 150°C and is accompanied with the increase of the aromatic carbon signal. The structure presents a large amount of hydroxyl yet, which may also be the result of the interaction of hydrogen with ethers and epoxies leading to the formation of hydroxyl[10] , meanwhile the carbonyls and hydroxyls may be converted in water molecules[10] and finally evaporated. The reduction at 250°C lead to a strong loss of hydroxyl groups and a reduction of the epoxy functionalities and the complete loss of adsorbed water.

The sequent treatments (350°C and 500°C) lead to a further loss of hydroxyl and epoxy groups, meanwhile the C=O functionalities are poorly affected. The treatment at 500°C apparently don't lead to a significant improvement of the reduction of the GO film.

The increase in intensity of the peak of the aromatic carbon peak is noted for each temperature of reduction, gaseous hydrogen can restore the sp^2 lattice with the healing of the holes formed by hydroxyl and carbonyl pairs[10] .

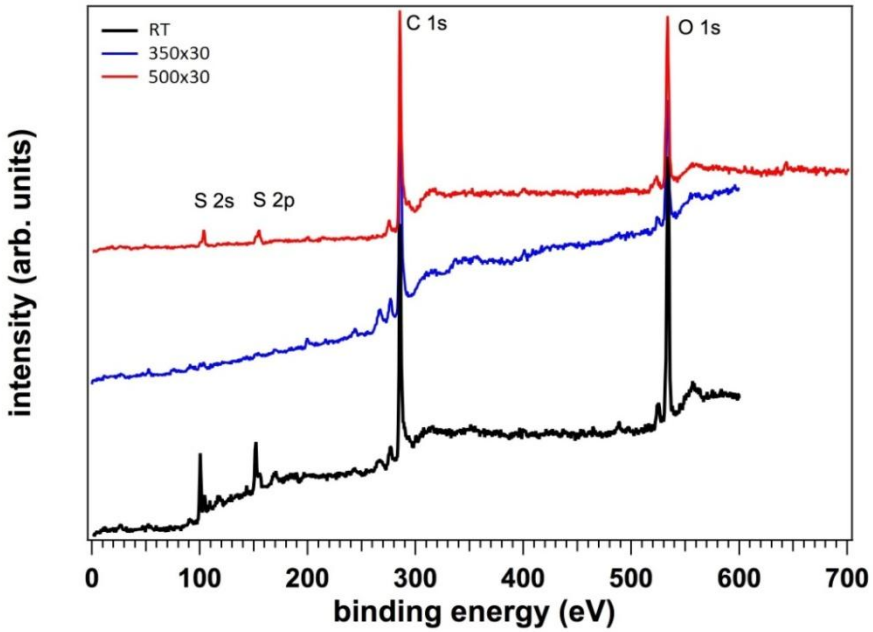

Figure 3.1.23 –XPS spectra of graphene oxide after the treatments at different temperatures of the samples RT, 350x30, 500x45.

In Figure 3.1.23, XPS surveys confirm the reduction of the structure observed with FTIR. The C/O ratio are drawn from the XPS survey and the value moves from 1,06 for the GO to 2,69 for GO treated at 350°C and 2,56 for the GO film treated at 500°C. The reduction treatment carried at the highest temperature, 500°C can be considered equivalent to a

reduction carried at 350°C. This may imply that treatments at higher temperatures won't lead to an increase in the reduction of the graphene oxide.

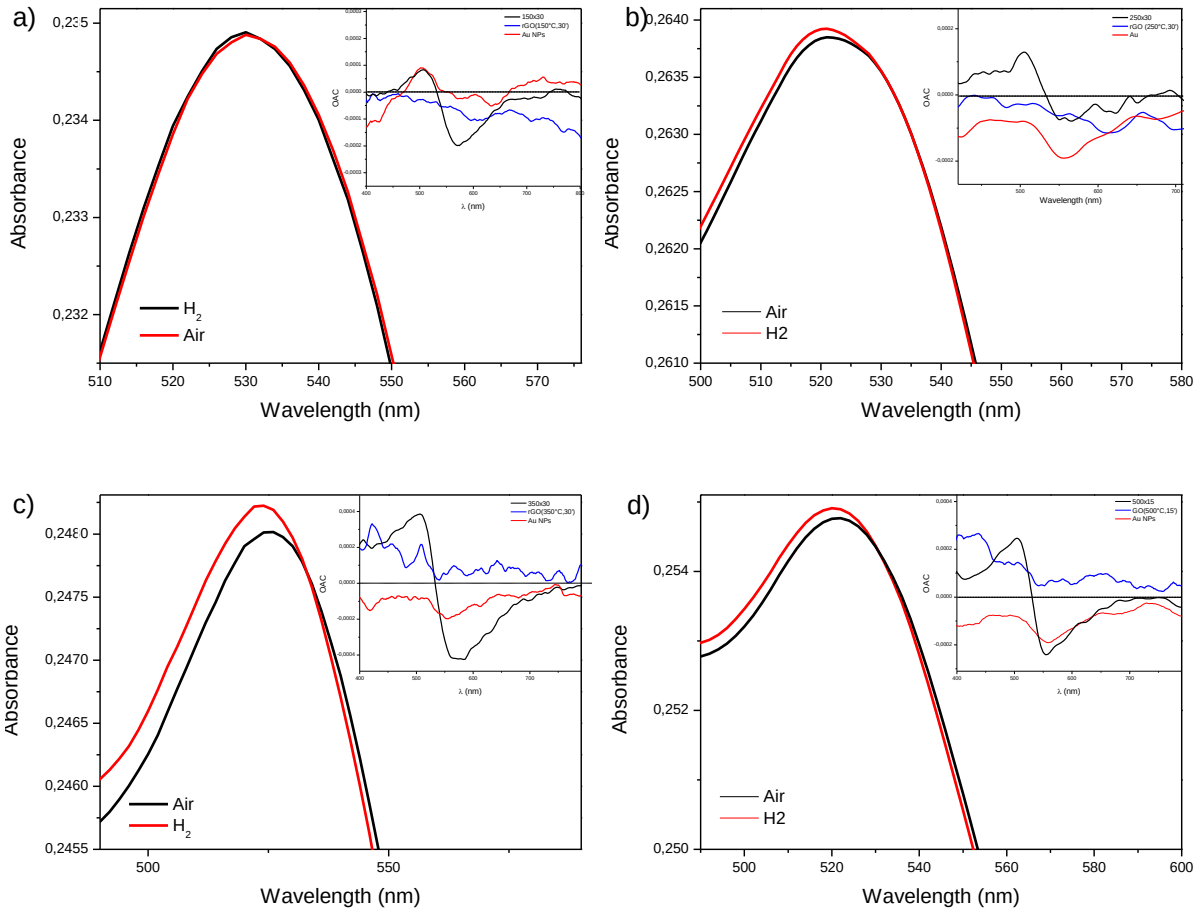

Figure 3.1.24 – a) Optical absorption spectra in air and in H_2(1%) of a)150x30 at OT= 100°C; b) of 250x30 at OT=150°C; c) of 350x30 at OT= 150°C; d) of 500x15 at OT= 150°C. In the insets are reported the OAC in H_2(1%) of the nanocomposites structures, bare Au NPs monolayer and rGO alone, heat treated with the same treatment of the composites.

The reduction of graphene oxide is fundamental to activate the gas sensing properties of the material. A preliminary test was conducted with GO and Au NPs at room temperature, but a positive response was not reached.

Figure 3.1.24 shows the optical gas sensing properties of the nanocomposites in static measurements toward H_2(1%). The treatment at 150°C triggers the optical gas sensing properties of the nanostructure: the LSPR peak of the Au NPs presents a weak blue-shift when the material is exposed to H_2(1%) as shown in Figure 3.1.24a.

The increase in reduction of the structure leads to a stronger blue-shift of the LSPR peak as reported in Figure 3.1.24.

The insets in Figure 3.1.24 report the OAC plots of the Au NPs, rGO on Au NPs and rGO reduced in the same conditions as the corresponding nanocomposite structures of rGO and Au NPs. Au NPs proves to be fundamental for the optical gas sensing of the nanostructure, even if the Au NPs alone are not responsive to H_2(1%).

The performance of the sensors toward H_2(1%) are summarized in Table 3.4, where the relative changes in absorbance and the response and recovery time are reported.

OT=150°C	Δabs/Abs$_{air}$ air to H_2(1%)	Time of response	Δabs/Abs$_{air}$ H_2(1%) to air	Time of recovery
150x30	$0.5*10^{-3}$	124 s	$0.3*10^{-3}$	105 s
250x30	$0.7*10^{-3}$	125 s	$0.6*10^{-3}$	243 s
350x30	$1*10^{-3}$	67 s	$0.9*10^{-3}$	204 s
500x30	$0.8*10^{-3}$	81 s	$0.6*10^{-3}$	294 s

Table 3.4 – Optical responses/recoveries entity and times of the films of Au NPs and GO reduced at different temperatures

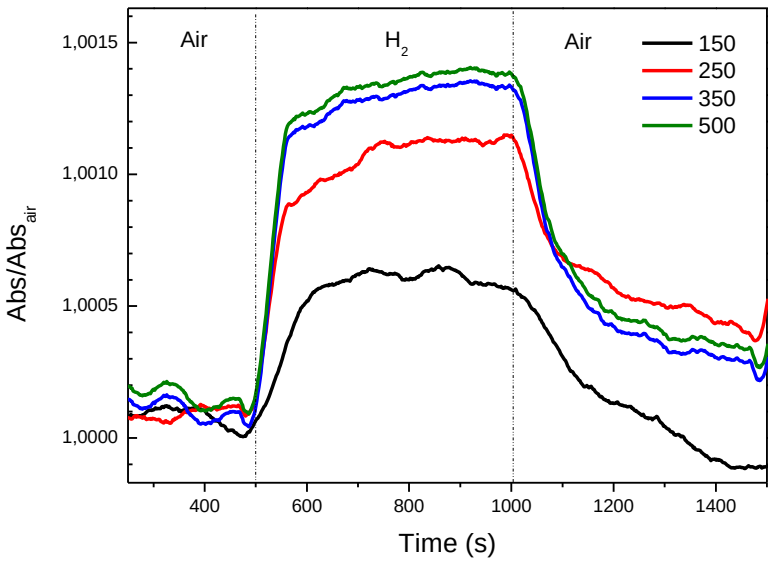

Figure 3.1.25 – Comparison of the dynamic scans of GO and Au NPs after reducing treatments at different temperature after different.

The time resolved scans have demonstrated an increase in performance with the increase in reduction. The response to H_2(1%) becomes faster and more intense with the higher temperature of treatment. The films treated at 350°C and 500°C present similar performance to H_2.

The variation in optical absorbance increases with a remarkable diminishing of the periods of the response as reported in Figure 3.1.25. In this image a direct comparison of the dynamic performance of the nanocomposites treated at progressively increasing temperature is depicted, suggesting a correlation between the reduction degree of the GO and the optical gas sensing performance.

3.1.4.5.1 H_2 gas sensing tests at 300°C

The gas sensing tests carried at 300°C have showed encouraging results toward H_2(1%).

Figure 3.1.26 display the OAC plots relative to H_2(1%) of films 350x30, 500x45 and Au NPs monolayer tested at 300°C. The behavior of the Au NPs to static gas sensing tests at 300°C is surprisingly strong and more intense than the change in absorbance exhibited by the nanocomposites of rGO and Au NPs.

Hence, at high temperatures the response of the nanocomposite sensors appeared ruled by the behavior of the Au NPs and rGO may act as a limiter in interaction of the between Au NPs and H_2 molecules.

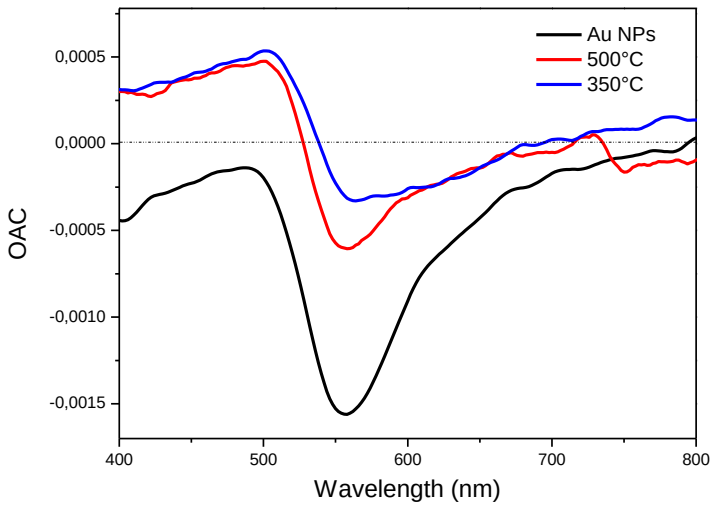

Figure 3.1.26 – OAC plots of bare Au NPs, 350x30 and 500x45 and

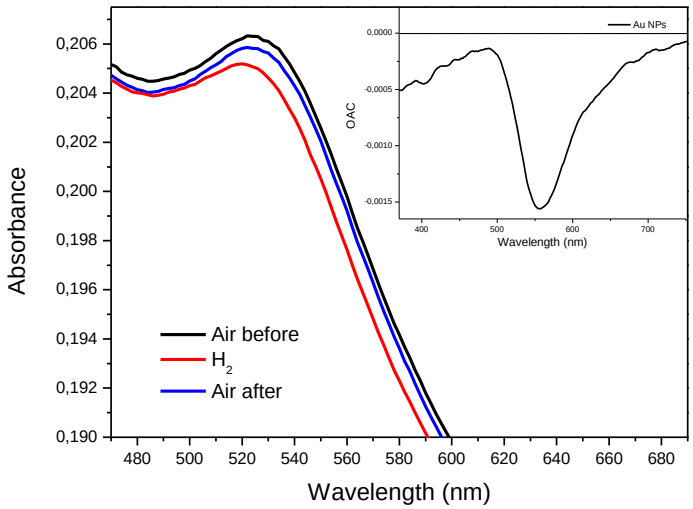

Figure 3.1.27 – Absorbance plot of Au NPs monolayer recorded in air-H_2(1%)-air cycle. In the inset OAC plot of bare Au NPs.

Figure 3.1.27 reports the optical absorbance of the LSPR peak of the Au NPs monolayer exposed to an air-H_2(1%)-air cycle.

The exposure to H_2 has a double effect, a slight decrease in intensity of the LSPR peak and the blue-shift of this peak. The behavior of the Au NPs appear similar to what observed with nanohemispheres of Au NPs at room temperature in atmosphere of H_2(10%) by Sil at al[19] . They observed the splitting of H_2 on Au nanohemispheres and the formation of hydride on the surface provoking an increase in transmittance of the material and the blue-shift of the LSPR peak, due to the different refractive index of the hydride.

At the best of our knowledge, this phenomenon has not been observed with spherical NPs so far. The high temperature, 300°C, employed in the gas sensing tests may induce the formation of hot electrons and catalyze the formation of the Au hydride, even with a concentration inferior than the one used in[19] .

More studied have to be carried for a better understanding of the response of Au NPs at 300°C and the possible development of sensors of bare Au NPs.

3.1.4.6 Sensing mechanism for rGO and Au NPs nanocomposites

The Au NPs have the only function of optical probe at the lower profile of OT(150°C), but become an active material for the detection of H_2 above 250°C. A threshold temperature between this behavior may be reasonably located in the range 200-250°C.

The interaction of gases occurs with the oxygen adsorbed on rGO or directly on the surface of rGO[20] [21] . The H_2 molecules interacts with the oxygen adsorbed on the surface of rGO with a charge injection to the rGO.

The presence of the metal nanoparticles may play a crucial role in the performances of the nanocomposites of rGO and Au NPs in comparison to the behavior of the chemoresistor of bare rGO prepared H_2 by Zhang et al[22] . They observe the influences of the functional group and conductivity on the interaction between H_2 molecules and rGO, which manifest with a decay of the response of the sensors toward H_2 beyond a certain degree of reduction, due to the removal of functional groups.

The nanostructures we developed rely on the synergic behavior of Au NPs and GO flakes.

The Au NPs highlight the variation in charge carriers in the rGO layer: the strong electromagnetic coupling allows a facile movement of the carriers to the Au NPs[12] leading to the blue-shift of the LSPR peak.

The reduction of graphene oxide strengthen the interaction between Au NPs and sp^2 domains with a subsequent enhancement of the photocatalytic activity of the nanostructures[25]. Moreover the Au NPs extend the photocatalytic activity of the rGO thank to the Resonant Energy Transfer effect till the visible range[23] [23] increasing the capability to excite electron-hole pairs with the visible light in the rGO layer [24] [21,25] .

Au NPs can also increase the sensitivity of the compound with the subtraction of electron to rGO due to the difference in work function, W_f[26] : W_f is -5.3 eV for gold and -4.6eV for rGO[27] . The Au NPs may act as p-dopant and extend the responsitivity of the nanocomposites to lower concentrations thank to the withdrawal of the electrons from rGO to Au NPs, leading to the shift of the LSPR peak of the metallic NPs.

The Au-rGO nanocomposites were sensitive also to CO(1%) and NO_2(1ppm) if treated at intermediate temperature, 250°C. The more reduced structure, obtained with treatments at higher temperatures, inhibits the reactivity of the films toward these species.

The loss of the capability of detection of CO and NO_2 may lay in the interaction of the gas molecules with the oxidized groups, where a stronger interaction than at the sp^2[20] [28] domains with rGO can occurs due to possible H-bonding or polar interaction between oxygen groups and polar molecules[29] [30] .

Hence, the interaction of rGO with CO or NO_2 may be reduced with the progressive removal of oxidized group of GO and the detection of these gases may be inhibited.

3.1.5 Conclusions

The treatments of nanostructures with H_2(5%v/v Argon) leaded to the reduction of graphene oxide at ambient pressure and moderate temperature, with a good level of reduction at 350°C. The thermal treatments in H_2(5%v/v Argon) has a healing effect on the chemical structure of GO, partially restoring the π-conjugation. The treatments at 500°C don't lead to a remarkable variation in structure than the treatments at 350°C.

The GO don't display sensing properties and the reducing treatments are fundamental to activate the response to the gases. Hence, the extension of the π-conjugation appear related to the optical gas sensing properties of the nanostructures to H_2(1%), the increases in sp^2 domains rises the response of the nanocomposites to H_2, allowing the detection of lower concentration of hydrogen.

Thus, the most reduced structures appear as the most performing sensors and are characterized by a fast and sharp response to H_2(1%) and can also detect H_2(100ppm) at a moderate operating temperature, 150°C. The freshly prepared sensor reduced for 45' at 500°C showed the best gas sensing properties thanks to the highly reduced chemical structure and the higher coverage in Au NPs, which have not been subject to the coalescence of the NPs in the previous cycles of high temperature treatments of reduction.

The higher OT enhances the capability of the sensor to perceive gaseous H_2 with a sharper and more intense reponse. However, at 250-300°C the Au NPs become an active sensing material toward H_2 and may heavily contribute in the gas sensing response interacting directly with the gas molecules.

The interaction with CO and NO_2 is initially triggered with the recovering of π-conjugation. However, the subsequent loss in functional oxygen groups may inhibit the response toward CO and NO_2, with the loss of the ability of sensors to detect CO and NO_2 once treated at high temperature.

References

[1] Balandin A, Ghosh S, Bao W, Calizo I, Teweldebrhan D, Miao F, et al. o§ and Lau C. Superior Thermal Conductivity of Single-Layer Graphene. Nano Letters 2008;8:902-907

[2] Rao CNR, Sood AK, Subrahmanyam KS, Govindaraj. Graphene: The New Two-Dimensional Nanomaterial. Angewandte Chemie 2009;48: 7752–7777.

[3] Novoselov KS, Geim AK, Morozov SV, Jiang D, Zhang Y, Dubonos SV, Grigorieva IV, Firsov AA. Electric field effect in atomically thin carbon films. Science 2004;306:666–669.

[4] Park S, Ruoff RS. Chemical methods for the production of graphenes. Nature Nanotechnology 2009;4:217–224.

[5] Tung VC, Allen MJ, Yang Y, Kaner RB. High-throughput solution processing of large-scale graphene. Nature Nanotechnology 2008;4:25–9.

[6] Mattevi C, Eda G, Agnoli S, Miller, Mkhoyan A,Celik O, Mastrogiovanni D,Granozzi G, Garfunkel E, Chhowalla M. Evolution of electrical, chemical, and structural properties of transparent and conducting chemically derived graphene thin films. Advanced Materials 2009;19:2577–2583.

[7] Li D, Müller MB, Gilje S, Kaner RB, Wallace GG. Processable aqueous dispersions of graphene nanosheets. Nature Nanotechnology 2008;3:101–105.

[8] Dreyer D, Park S, Bielawski C, Ruoff R. The chemistry of graphene oxide. Chemical Society Reviews 2009;39:228–240.

[9] Pei S, Cheng H-M. The reduction of graphene oxide. Carbon 2012;50:3210–3228.

[10] Bagri A, Mattevi C, Acik M, Chabal Y, Chhowalla M, Shenoy V. Structural evolution during the reduction of chemically derived graphene oxide. Nature Chemistry 2010;2:581–587.

[11] Jiang X, Nisar J, Pathak B, Zhao J, Ahuja R. Graphene oxide as a chemically tunable 2-D material for visible-light photocatalyst applications. Journal of Catalysis 2013;299:204-209.

[12] Huang J, Zhang L, Chen B, Ji N, Chen F, Zhang Y, Zhang Z. Nanocomposites of size-controlled gold nanoparticles and graphene oxide: formation and applications in SERS and catalysis. Nanoscale 2010;2:2733-2738.

[13] Favaro M, Agnoli S, Valentin C, Mattevi C, Cattelan M, Artiglia L, Magnanod E, Bondinod F, Nappinid S, Granozzi G. TiO2/graphene nanocomposites from the direct reduction of graphene oxide by metal evaporation. Carbon 2014;68:319-329.

[14] Zhang X, Zhang J, Wang H, Hao Y, Zhang X, Wang T, Wang Y, Zhao R, Zhang H, Yang B. Thermal-induced surface plasmon band shift of gold nanoparticle monolayer: morphology and refractive index sensitivity. Nanotechnology 2010;21:465702.

[15] Mock J, Hill R, Degiron A, Zauscher S, Chilkoti A, Smith D. Distance-dependent plasmon resonant coupling between a gold nanoparticle and gold film. Nano Letters 2008;8:2245–52.

[16] Scherrer P. Bestimmung der Grösse und der inneren Struktur von Kolloidteilchen mittels Röntgenstrahlen. Nachrichten von Der Gesellschaft Der Wissenschaften 1918;2;98.

[17] Patterson AL. The Scherrer formula for X-ray particle size determination. Physical Review 1939;56:978.

[18] Jung I, Vaupel M, Pelton M, Piner R, Dikin D, Stankovich S, Stankovich S, An J, Ruoff R. Characterization of Thermally Reduced Graphene Oxide by Imaging Ellipsometry. The Journal of Physical Chemistry C 2008;112:8499–8506.

[19] Sil D, Gilroy K, Niaux A, Boulesbaa A, Neretina S, Borguet E. Seeing Is Believing: Hot Electron Based Gold Nanoplasmonic Optical Hydrogen Sensor. Acs Nano 2014;8:7755-7762.
[20] Robinson J, Perkins F, Snow E, Wei Z, Sheehan P. Reduced Graphene Oxide Molecular Sensors. Nano Lett 2008;8:3137–3140.
[21] Cittadini M, Bersani M, Perrozzi F, Ottaviano L, Wlodarski W, Martucci A. Graphene oxide coupled with gold nanoparticles for localized surface plasmon resonance based gas sensor. Carbon 2014;69:452–459.
[22] Zhang L-S, Wang W, Liang X-Q, Chu W-S, Song W-G, Wang W, Wu Z-Y. Characterization of partially reduced graphene oxide as room temperature sensor for H 2. Nanoscale 2011;3:2458–2460.
[23] Cushing SK, Li J, Meng F, Senty TR, Suri S,Zhi M, Li M, Bristow A, N Wu. Photocatalytic activity enhanced by plasmonic resonant energy transfer from metal to semiconductor. Journal of the American Chemical Society 2012;134:15033–15041.
[24] Niu J, Shin YJ, Son J, Lee Y, Ahn JH, Yang H. Shifting of surface plasmon resonance due to electromagnetic coupling between graphene and Au nanoparticles. Optics Express 2012:20;19690.
[25] Niu J, Shin YJ, Lee Y, Ahn JH, Yang H. Graphene induced tunability of the surface plasmon resonance. Applied Physics Letters 2012;100:061116.
[26] Fu X, Bei F, Wang X, O'Brien S, Lombardi JR. Excitation profile of surface-enhanced Raman scattering in graphene–metal nanoparticle based derivatives. Nanoscale 2010;2:1461-1466.
[27] Sygellou L, Paterakis G, Galiotis C, Tasis D. Work Function Tuning of Reduced Graphene Oxide Thin Films. The Journal of Physical Chemistry C 2016;120:281–290.
[28] Zhang Y-H, Chen Y-B, Zhou K-G, Liu C-H, Zeng J, Zhang H-L, Peng Y. Improving gas sensing properties of graphene by introducing dopants and defects: a first-principles study. Nanotechnology 2009;20:185504
[29] Robinson JA, Snow ES, Badescu SC, Reinecke TL, Perkins FK. Role of defects in single-walled carbon nanotube chemical sensors. Nano Letters 2006;6:1747–1751.
[30] Gadipelli S, Guo Z. Graphene-based materials: Synthesis and gas sorption, storage and separation. Progress in Materials Science 2015;69:1–60.

Chapter 3 - Optical gas sensor based on graphene oxide

3.2 Chemically modified Graphene for room temperature optical gas sensor

3.2.1 Introduction

Different methods for the production of graphene have been covered, with mechanical exfoliation [1], chemical vapor deposition [2], epitaxial growth [3] and the route of wet chemistry with graphene oxide (GO) [4].

The ease in handling and processability in GO led to several attempts to recover the structure of the pristine graphene by the defective and oxide structure of GO [5]. Among the techniques employed to reduce GO, chemical reduction retains the advantages of the manipulation of GO. In fact, Chemically Modified Graphene (CMG) is synthesized by GO in solution and is soluble in different solvents, conferring high versatility and closing graphene to industrial and scaling-up processes.

The loss of functional oxidized groups makes CMG less soluble in polar solvents, but the solubility can be maintained by regulation the pH of water solution [6] [7], use of surfactant [8] and the grafting of functional groups [9,10].

CMG attains another advantage to GO reduced with other techniques: meanwhile, the latter is often employed in combination of other materials to achieve an elevated sensitivity and/or selectivity to gas species, the former can be provided, in the reduction step, with covalent [11] [9] or adsorbed [12] [13] functionalization improving its sensitivity to target species.

Hydrazine-based CMG has captured large attention and has been extensively studied as a material [14] [15] and chemoresistor [16] [11], but low attention was directed toward CMG obtained with para-phenylenediamine (PPD). Previous studies evidenced the accomplished reduction and the grafting of PPD on GO [17] and suggested the possibility of a CMG competitive to the hydrazine based ones [18].

The target of the following work is the chemical reduction of GO with PPD and the evaluation of the sensing properties of the material toward dangerous species.

Gold nanoparticles (Au NPs) are used for their peculiar characteristic of the Localized Surface Plasmon Resonance (LSPR) effect. The LSPR enhances the variation in optoelectronic properties of the surrounding media, more precisely regarding the refractive index of the surrounding media or by charge injection/subtraction [19].

On the purpose of analyze the optical gas sensing properties of CMG, thin films of chemically reduced GO have been fabricated and tested as gas sensor and the response to gases have been assessed for the CMG alone and also for the nanostructure of CMG and gold nanoparticles.

Gas sensing tests have been run to study the optical gas sensing properties of the nanostructures at room temperature

3.2.2 Experimental

3.2.2.1 Graphene oxide synthesis

GO was synthesized with a modified Hummers synthesis [20] . A synthesis carried at temperatures close to room temperature, (35-40°C) and without the aid of HNO_3 has been set-up by Chen et al [21] in order to remove the formation of dangerous NO_2 fumes during the reaction.

0.5g of graphite flakes were mixed with 3g of $KMnO_4$ in a round flask in ice-cold bath.

Then,30ml of concentrated H_2SO_4 (98%) were slowly added in the flask.

The slurry obtained was slowly carried at 40°C in 2,5h to achieve the homogenization of the compound. The reaction was carried at 40°C for 24h, then the solution was quenched by dilution with 60ml of water. Finally, a solution of 5ml H_2O_2 (30%) in 70ml water was added to the batch.

The resulting brown slurry was dispersed in water containing HCl(37%) in ratio 1:9 of HCl:H_2O and centrifugated to remove the metal ions. GO was then further centrifugated in water solution till pH 7 was reached.

3.2.2.2 Chemically modified graphene synthesis

Chemically Modified Grafene was obtained by reaction with Para-PhenyleneDiamine (PPD). A solution of 3mg/ml of PPD in ethanol was added to a solution of GO 1mg/ml in water , and the reaction occurred at room temperature for 24h. The product of the reduction was an ammine terminated graphene referred as CMG.

CMG was extensively purified with ultrasound bath for 10’ and centrifugation in solvent of H_20:EtOH in ratio 1:1. This procedure was cycled till the obtained surnatant was transparent, indicating the accomplished removal of the PPD.

The synthesis of CMG was conducted also at higher temperature, 95°C, with a reduced PPD:GO ratio. A synthesis with a simpler purification step and a shorter reaction time was also attempted, with a GO:PPD ratio of 0.3:1 and a reaction period of 3h. The lower concentration and reaction time were compensated with a higher temperature, 95°C. The material obtained in this way is referred as 0.3CMG.

The purified CMG was dissolved in EtOH in concentration of 0.3mg/ml.

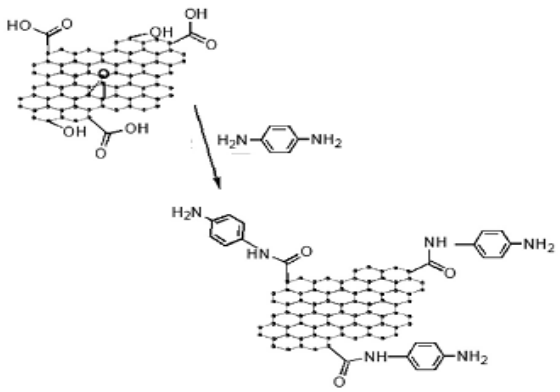

Figure 3.2.1– Schematic of the mechanism of reduction and functionalization of GO with reduction with PPD [22] .

3.2.2.3 Au NPs

Au NPs were prepared with the procedure described in Appendice A2.1 and the monolayers were produced with the methodillustrated in Appendice A2.14.

3.2.2.4 Sample production

GO thin films were produced on SiO_2 substrates functionalized with Ammino propyl triethoxy silane (APTES). GO was deposited with dropcasting and spincoating.

Dropcasting technique is similar to that explained in A2.15: GO solution is dropped on the substrate and is left to sediment for 10’ and then the film is rinsed with water and dried with air flow. The deposition with spincoating was run at 2000rpm and 60s.

CMG was deposited with spincoating with 4 steps of deposition at 500rpm for 30s.

3.2.3 GO characterization

Figure 3.2.2 displays the UV/Vis spectra of graphene oxide. It presents the typical features of GO with a peak at 224nm and a shoulder at 292nm. The former is related to the electronic transition $\pi \rightarrow \pi^*$, the latter to the transitions $\sigma \rightarrow \pi^*$ of carbonyl groups [23] .

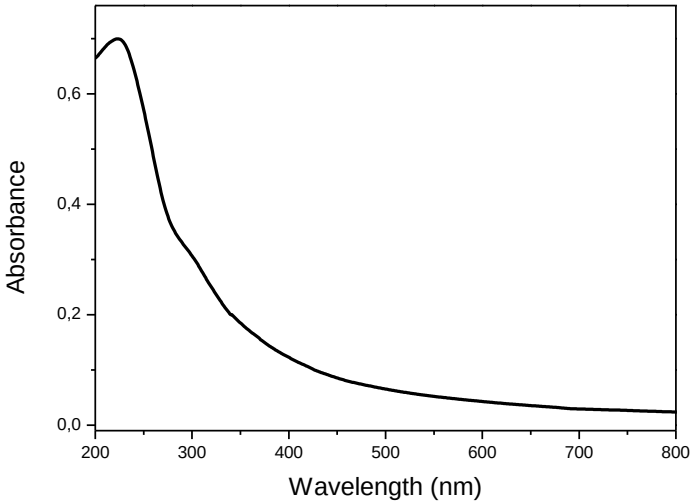

Figure 3.2.2 –UV/vis absorbance plot of GO in water solution in a quartz cuvette.

The analysis of the chemical structure was conducted with FTIR and confirms that the oxidation of graphite has occurred. Hydroxyls (~1074 cm^{-1}), epoxy (~1220 cm^{-1}), carbonyls (~1625 cm^{-1}) and carboxyls (~1728 cm^{-1}) can be noticed in Figure 3.2.2.

The peaks at 1388 cm^{-1} and the broad band at 3300 cm^{-1} are attributed to water molecules that can be adsorbed on the surface of GO or intercalated among the planes.

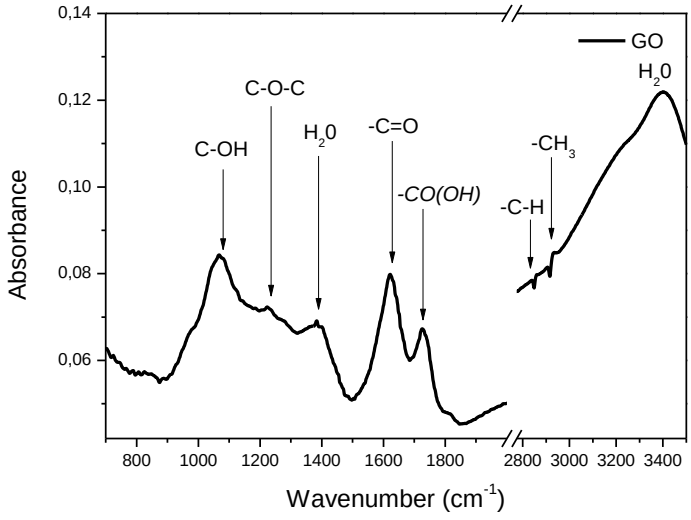

Figure 3.2.3 – FTIR spectrum of graphene oxide in KBr disk

The XRD pattern of GO is reported in Figure 3.2.4. The (002) peak of graphitic material is shifted to 10°. The stacking distance was drawn with Bragg equation [24] and the distance among planes of GO has a value of 9Å.

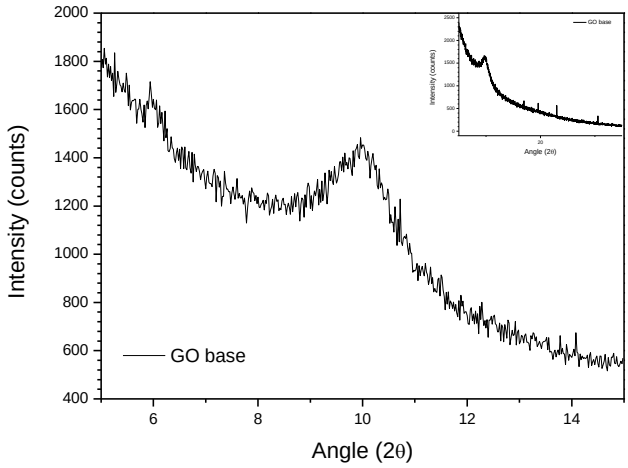

Figure 3.2.4 –XRD analysis of GO thin film. In inset is reported the XRD scan of a GO thin film in the range of 2θ of 5-35°.

3.2.4 Film production

Films of GO have been deposited with spincoating and dropcasting. The amount of material deposited by spincoating is superior than by dropcasting with a high concentration, 1mg/ml.

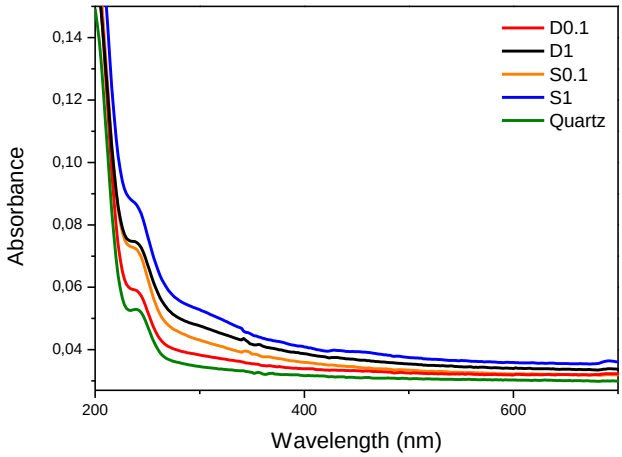

Figure 3.2.5 – Comparison of the absorbance plot of GO thin films deposited by dropcasting (D0.1 and D1) and spincoating (S0.1 and S1), with different concentration of GO in water solution: 0.1mg/ml for D0.1 and S01 and 1mg/ml for D1and S1.

At inferior concentration (0.1mg/ml) the film obtained with dropcasting are more dense of material, displaying a minor transparency (see Figure 3.2.5). Spincoated GO at 0.1mg/ml concentration has not enough time to sediment at the surface and is washed away by the solvent flux with the spinning of the substrate.

Due to the low amount of material on the substrates the dropcasting technique have been discarded.

The morphology of spincoated GO is depicted in Figure 3.2.6a. The sheets are wrinkled and scrolled by the flux of solvent during spincoating. Few sheets are spread on the surface. Figure 3.2.6c shows the height profile of a flake. The variation in height in the order of nm can be ascribed to the scrolled sheets adsorbed on the flakes.

In Figure 3.2.6b the GO flakes can be recognized without the presence of scrolled and corrugated sheets. The film was obtained by spincoating followed by rinsing with water. Only the flakes spread on the surface had a sufficiently extent of weak interactions with the functionalized substrate and remained attached on the surface.

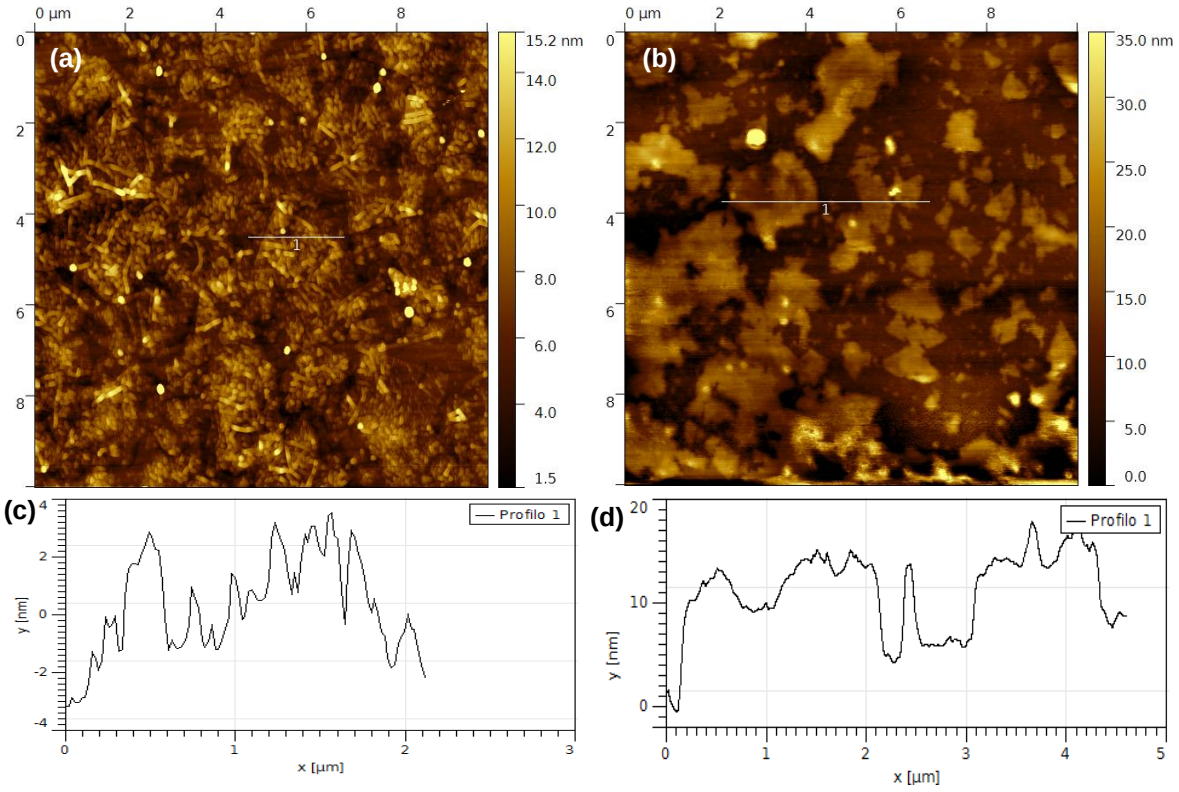

Figure 3.2.6 – a) AFM image of the thin film obtained with spincoating of 0.1mg/ml of GO on quartz substrate; b) AFM image of the thin film obtained with spincoating of 0.1mg/ml of GO, then rinsed with water; c) height profile of line in 6a; d) height profile of line in 6b.

The sheets are displaced in flakes ranging from 5 to 10nm in height and large from hundreds to few microns in side length, as can be seen by profile in Figure 3.2.6b and related height profile in 6d.

3.2.5 CMG optical characterization

The UV/Vis spectra of the chemically reduced graphene oxide (GN) and GO are compared in Figure 3.2.7. The reduction with excess of PPD causes modification in the optical properties of GO. The optical transition $\pi \rightarrow \pi^*$ moves from 224nm to 248nm implying the extension of the π conjugation in CMG sheets.

In addition, CMG shows an absorbance band at 550nm which is a signal of the presence of PPD on the sheets of GO, this is reflected in the pinkish shade of of the solution of CMG in Figure 3.2.7b.

This peak may be related to the grafting of the PPD on the graphene layers in form of dimers or oligomers [25] [26] , since it is associated to the excitonic transition of quinoid rings [25] of the dimers/oligomers of PPD.

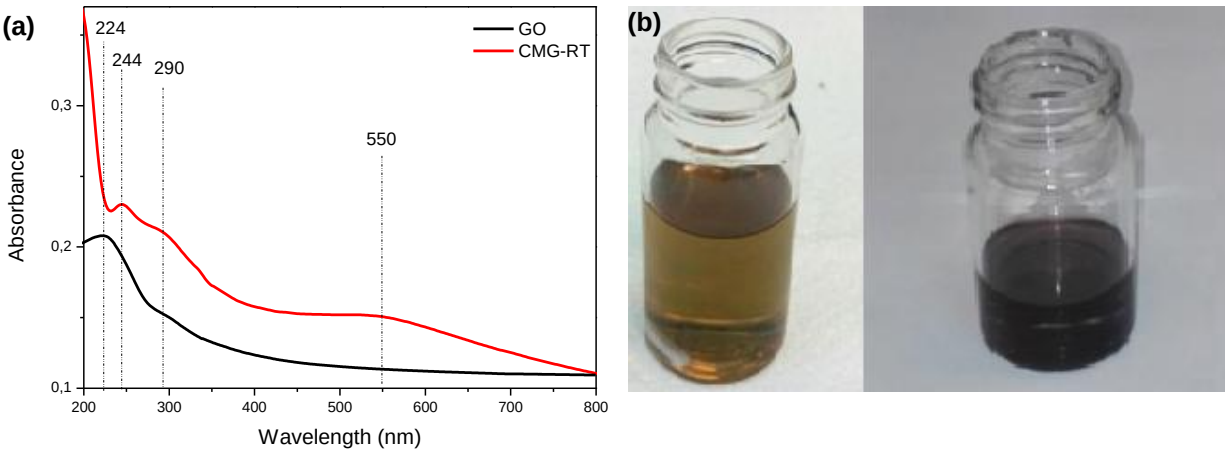

Figure 3.2.7 – a) UV/Vis absorbance plots of GO and CMG deposited on silica substrates; b)Pictures of a solution of 0.05mg/ml of GO at the left and a solution of 0.3mg/ml of CMG at right.

The FTIR plot of CMG is compared to GO in Figure 3.2.8. The chemical reduction leads to a sharp rise of the peak at 1510 cm^{-1}, and dramatic suppression of the peaks of hydroxyl and epoxy functionalities, which are visible in GO plot respectively at 1080 cm^{-1} and 1220 cm^{-1}. The peak related to aromatic carbon increased in intensity at ~1609 cm^{-1} .

Instead, the peaks relative to the carbonyls and carboxyls have been altered by the chemical reduction with PPD at 1737 cm^{-1} and 1630 cm^{-1} can be correlated to the C=O stretching

vibration of (C=O)NH-R groups [22] . This appear confirmed by the peaks at 1515 cm^{-1} and 730 cm^{-1} of the N-H stretching and swagging bond [22] . The peaks at ~1250 cm^{-1} and ~1300 cm^{-1} concern the C-N [17] [12] bond with aliphatic and aromatic carbon, suggesting a connection between the sp^3 carbon of the functional group of GO and the aromatic carbon of the PPD ring.

The presence of quinoid carbon and nitrogen is suggested by the shoulders at ~1480 cm^{-1} and ~1570 cm^{-1} [27] .

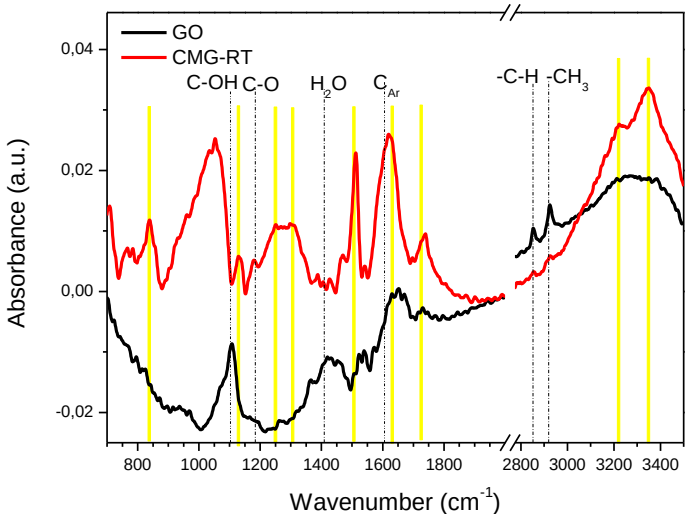

Figure 3.2.8 – FTIR spectrum of GO(black line and) and CMG(red line)

The synthesis conducted at room temperature for 24°C with a large excess of PPD (GO/PPD mass ratio 1/3) proved to be reliable in repeatability. The plots of the absorbance in UV/Vis (Figure 3.2.9a) and IR (Figure 3.2.9b) of two batches produced in the same condition are very similar and exhibited the same peaks.

The RT2 sample display pronounced slightly lower absorbance at 1000 cm^{-1} and 1050cm^{-1} corresponding to C-H vibration.

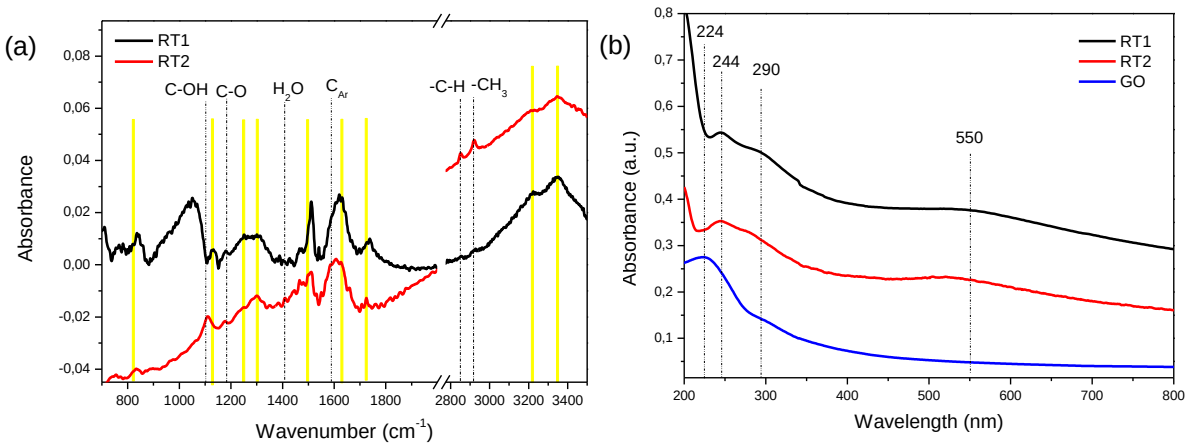

Figure 3.2.9 – a) FTIR absorbance plots of CMG synthesized at room temperature in excess of PPD in two different synthesis: RT1 has been produced with batch 1 and RT2 has been produced with batch 2; b) UV/Vis absorbance spectra of RT1 and RT2 and GO.

Three synthesis of 0.3CMG have been prepared, and the resulting material are labeled 0.3CMGB1, 0.3CMG B2, 0.3CMGB3. The FTIR plots of the material obtained with the three synthesis are reported in Figure 3.2.10. The scans of the material obtained by the different batches is heterogeneous, with a partial reduction, i.e.the peaks of hydroxyls and epoxy are predominant respectively in plot0.3CMG B2 and 0.3CMG B3. Moreover, the functionalization is not well expressed with a partial correspondence between the bands observed in CMG (stressed by vertical yellow lines) and the bands of 0.3CMG.

The trial of synthesis using a minor amount of PPD and rising the temperature to compensate the minor amount of reducing agent reveals to be unsatisfying and not reproducible.

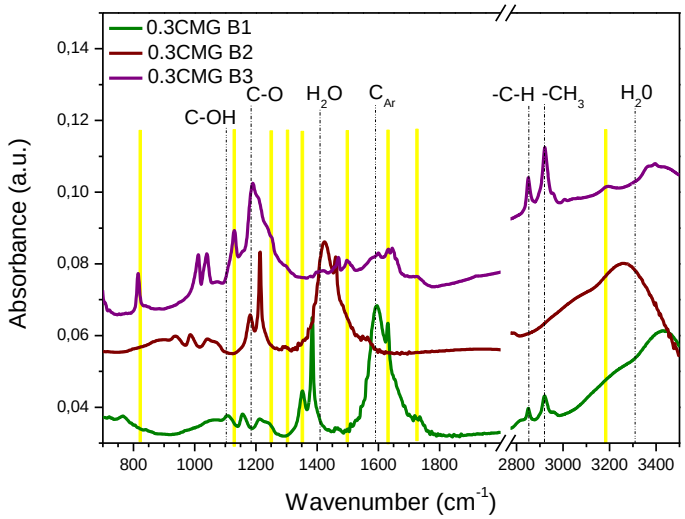

Figure 3.2.10 – FTIR absorbance plot of the 0.3CMGB1, 0.3CMG B2, 0.3CMGB3.

3.2.5.1 Morphological characterization of Chemically Modified Graphene

TEM images of the CMG have been acquired and the size of the sheets of CMG were evaluated. CMG ranges roughly from 500nm to 2µm per side. Corrugation and folding at the edges of the sheets can be recognized.

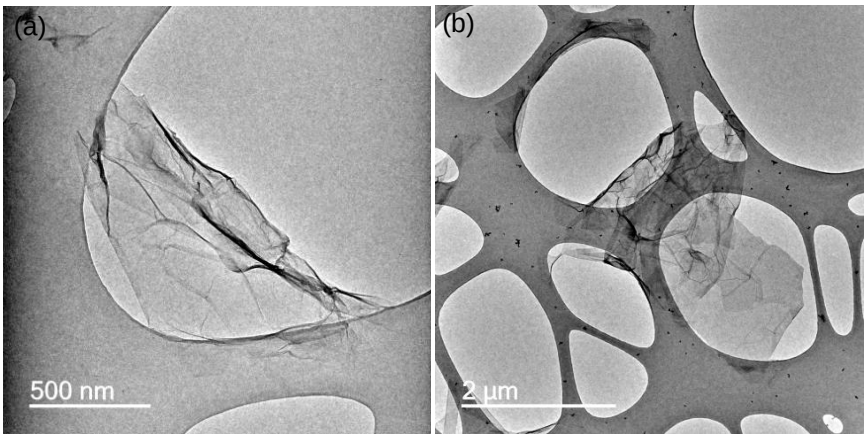

Figure 3.2.10 – TEM images of the sheeets of CMG at a) high and b) low resolution.

The morphology of the thin film of CMG is investigated in Figure 3.2.11.

A good coverage of the surface by CMG can be noted in Figure 3.2.11a. The film is not homogeneous. A close-up image (Figure 3.2.11b) displays the disposition of CMG in flakes of variables heights ranging from few nanometers to 100nm. Corrugated and scrolled sheets are present also in CMG thin films.

The average thickness of the thin film of CMG is 50nm.

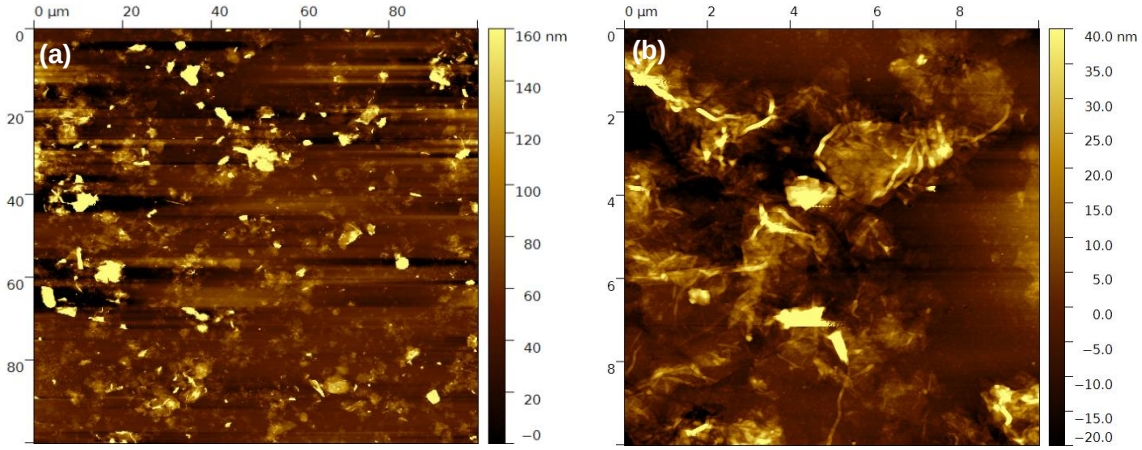

Figure 3.2.11 – a) AFM profile images of the CMG deposited by spincoating on quartz and b) close-up.

3.2.5.2 Optical gas sensing properties of CMG film

Figure 3.2.12 reports the UV/Vis spectra of CMG deposited on bare quartz and deposited on a monolayer of Au NPs. The spectrum of the Au NPs is showed for reference. The nanocomposites present the characteristic features of both the nanomaterials, the cromophore group of CMG is masked by the overlapping strong absorbance of the LSPR peak of Au NPs

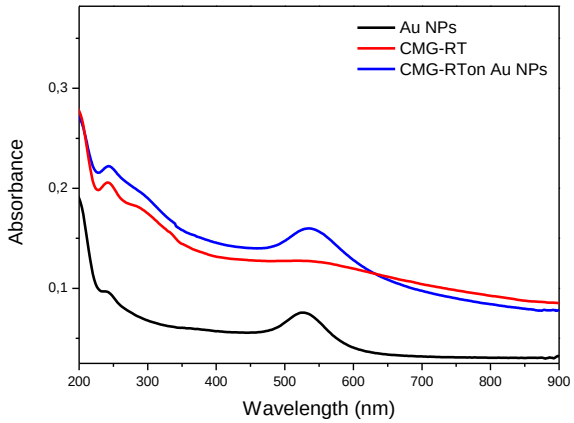

Figure 3.2.12 – UV/Vis plot of a Au NPs monolayer (black line) CMG deposited on bare quartz (red line) and deposited on a monolayer of Au NPs (blue line).

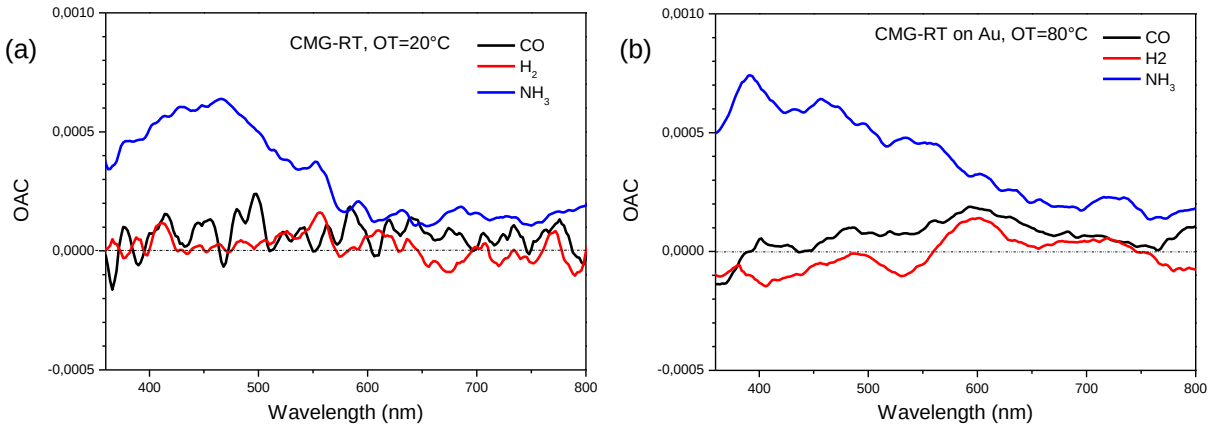

Figure 3.2.13 – OAC plot of a) CMG and b) CMG on Au NPs.

Both the films have been tested as optical gas sensor. The static tests produced the OAC plots toward H_2(1%), CO(1%), NH_3(1000ppm). The results of the static measures are reported in Figure 3.2.13.

NH_3 produces an appreciable variation of the optical properties of CMG. Similar variation is observed for CMG on Au NPs, the metal NPs are not necessary for the detection of gaseous NH3, suggesting that they are not involved in the sensing mechanism of ammonia.

The sensing mechanism toward NH_3 can be ascribed to the chromophore group at 550nm.

Previous studies described the polymer of PPD as an analogous of the conductive form of Polyaniline, emeraldine salt, with cationic N present in the polymer chain [27].

The presence of p-doped dimers/oligomers of PPD can be raised by the π-π interaction between the rings of the oligomers and the sp^2 domains of CMG, due to the p-doping effect of the π cloud toward the PPD abducts [28].

Hence, ammonia acts dedoping the PPD oligomers, with a acid/base reaction with the Pani-like strucutures [29] [30] [31] .

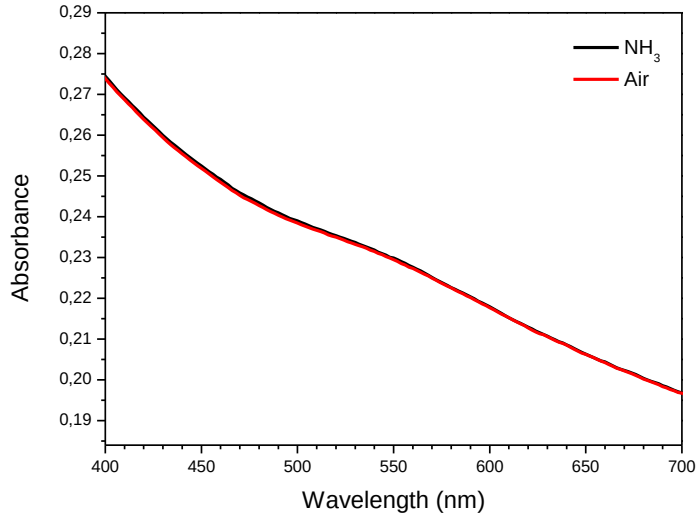

Figure 3.2.14 – Visible Absorbance of CMG in air and in NH_3(1000ppm) atmosphere.

Thus, the electronic band at 550nm of PPD can be considered the analogous of the band at 500-800nm of the PANI [30] . Such optical band is sensitive to the extension or diminishing of N cation in the polymer chain, i.e. doping and dedoping, of the polymer. The dedoping is manifested with a shift of the band to the blue (visible in Fig. 3.2.14) with an increase of absorbance intensity at shorter wavelength, alike to what is observed in the optical absorbance properties of CMG exposed to NH_3 [30] .

Besides the doping action, the interaction between CMG sheets and the PPD oligomers has a further function. Previous studies have demonstrated that the π-π interaction allows a charge transfer from the oligomer to the graphene sheets enhancing the response of the hybrid and accelerating the recovery step [32] [31] .

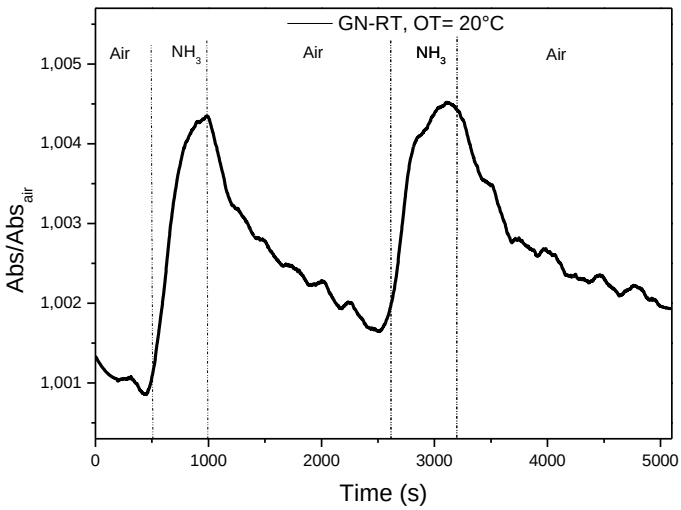

Figure 3.2.15 - Time resolved scan of CMG carried at room temperature and λ=510nm.

In Figure 3.2.15 the dynamic response of CMG toward NH_3 shows the encouraging results obtained with the tests at room temperature.

An appreciable variation in relative absorbance, in the order of $3*10^{-3}$, is obtained and is repeated in two cycles. The response take place in less than 5 minutes and the recovery is partial in 500s.

In Figure 3.2.13b a small variation in absorbance of CMG on Au NPs can be noted in atmosphere of CO(1%). The absorbance spectra in Figure 3.2.16 of the Au LSPR of the nanocomposite structure shows a weak blue-shift of the LSPR peak.

The interaction of CO with CMG appears different respect to the interaction with NH_3.

CO can interact with the oxygen adsorbed on the surface or directly with CMG sheets and inject electrons in CMG, without inducing the dedoping of PPD dimers/oligomers.

The ability of CO to donate electrons may result enhanced also by the interaction of CO with functional PPD groups [9] . The interaction of CMG with CO may be eased by the presence of polarized and charged groups that may have a stronger attracting action on the CO molecules than H_2 molecules.

The charge introduced to CMG are finally transferred to the Au NPs, thank to the strong electromagnetic coupling between reduced graphene oxide and Au NPs [33] causing a blue-shift of the LSPR peak noted in Figure 3.2.13b.

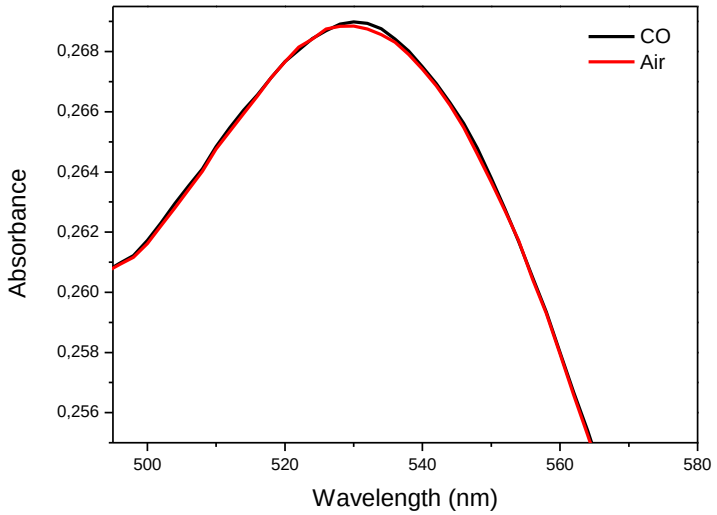

Figure 3.2.16 – Absorbance spectra of CMG on Au NPs acquired in air and in CO(1%).

3.2.5 Conclusion

Chemically reduced graphene was produced with reaction with PPD. The reaction of reduction decreases the presence of hydroxyl and epoxy groups and the grafting of oligomers of PPD to basal graphene sheets appear suggested by its optical properties in visible and IR range.

CMG was tested as optical sensor at room temperature and revealed a promising material for the development of optical sensors working at room temperature.

In fact, the thin films of bare CMG and CMG coupled with Au NPs produced positive results toward NH_3.

The addition of Au NPs appear to increase the range of gas detected and CO may be detected. The correlated OAC plots indicate a different mechanism of sensing for NH_3 and CO which may lead to the development of sensors capable of discriminating between them.

References

[1] Novoselov KS, Geim AK, Morozov SV, Jiang D, Zhang Y, Dubonos SV, Grtigorieva IV, Firsov AA. Electric field effect in atomically thin carbon films. Science 2004;306:666–669.

[2] Wang Y, Zheng Y, Xu X, Dubuisson E, Bao Q, Lu J,Loh KP. Electrochemical Delamination of CVD-Grown Graphene Film: Toward the Recyclable Use of Copper Catalyst. ACS Nano 2011;5:9927–9933.

[3] Berger, Song Z, Li X, Wu X, Brown N, Naud C, Mayou D, Li T, Hass J, Marchenkov A, Conrad E, First P, De Heer W. Electronic Confinement and Coherence in Patterned Epitaxial Graphene. Science 2006;312:1191–1196.

[4] Dreyer D, Park S, Bielawski C, Ruoff R. The chemistry of graphene oxide. Chemical Society Reviews 2009;39:228–240.

[5] Pei S, Cheng H-M. The reduction of graphene oxide. Carbon 2012;50:3210–3228.

[6] Li M, Liu C, Cao H, Pan J, Zhao H, Zhang Y. The determination of surface charge on nitrogen-containing reduced graphene oxides and its application to adsorb molybdate. Materials Chemistry and Physics 2015;152:77-84.

[7] Park S, An J, Piner R, Jung I, Yang D, Velamakanni A, Nguyen S, Ruoff R. Aqueous Suspension and Characterization of Chemically Modified Graphene Sheets. Chem Mater 2008;20 6592–6594.

[8] Liang Y, Wu D, Feng X, Müllen K. Dispersion of graphene sheets in organic solvent supported by ionic interactions. Advanced Materials 2009;21: 1679–1683..

[9] Yuan W, Liu A, Huang L, Li C, Shi G. High Performance NO2 Sensors Based on Chemically Modified Graphene. Advanced Materials 2013;25:766–771.

[10] Si Y, Samulski E. Synthesis of Water Soluble Graphene. Nano Letters 2008;8:1679–1682.

[11] Fowler J, Allen M, Tung V, Yang Y, Kaner R, Weiller B. Practical chemical sensors from chemically derived graphene. ACS Nano 2009;3:301–306.

[12] Wu Z, Chen X, Zhu S, Zhou Z, Yao Y, Quan W, Liu B. Enhanced sensitivity of ammonia sensor using graphene/polyaniline nanocomposite. Sensors and Actuators B: Chemical 2013;178:485-493.

[13] Hu N, Yang Z, Wang Y, Zhang L, Wang Y, Huang X, Wei H, Wei L, Zhang Y. Ultrafast and sensitive room temperature NH3 gas sensors based on chemically reduced graphene oxide. Nanotechnology 2014;25:025502.

[14] Park S, An J, Potts JR, Velamakanni A, Murali S, Ruoff R. Hydrazine-reduction of graphite-and graphene oxide. Carbon 2011;9:3019–3023.

[15] Eda G, Fanchini G, Chhowalla M. Large-area ultrathin films of reduced graphene oxide as a transparent and flexible electronic material. Nature Nanotechnology 2008;3:270–274.

[16] Robinson J, Perkins F, Snow E, Wei Z, Sheehan P. Reduced Graphene Oxide Molecular Sensors. Nano Lett 2008;8:3137–3140.

[17] Ma H-L, Zhang H-B, Hu Q-H, Li W-J, Jiang Z-G, Yu Z-Z, Dasari A. Functionalization and reduction of graphene oxide with p-phenylene diamine for electrically conductive and thermally stable polystyrene composites. ACS Applied Materials & Interfaces 2012;4:1948–1953.

[18] Wang B, Luo B, Liang M, Wang A, Wang J, Fang Y, Chang Y, Zhi L. Chemical amination of graphene oxides and their extraordinary properties in the detection of lead ions. Nanoscale 2011;3:5059–5066.

[19] Bingham JM, Anker JN, Kreno LE, van Duyne R. Gas sensing with high-resolution localized surface plasmon resonance spectroscopy. Journal of the American Chemical Society 2010;132:17358–17359.
[20] Hummers WS, Offeman RE. Preparation of Graphitic Oxide. Journal of the American Chemical Society 1958;80:1339–1339.
[21] Chen J, Yao B, Li C, Shi G. An improved Hummers method for eco-friendly synthesis of graphene oxide. Carbon 2013;64:225–229.
[22] Remyamol, John H, Gopinath P. Synthesis and nonlinear optical properties of reduced graphene oxide covalently functionalized with polyaniline. Carbon 2013;59:308–314.
[23] Marcano D, Kosynkin D, Berlin J, Sinitskii A, Sun Z, Slesarev A, Alemany L,Lu W, Tour J. Improved Synthesis of Graphene Oxide. ACS Nano 2010;4:4806–4814.
[24] Bragg WH, Bragg WL. The reflection of X-rays by crystals. Proceedings of the Royal Society of London Series A, Containing Papers of a Mathematical and Physical Character 1913:428–438.
[25] Wen T-C, Sivakumar C, Gopalan1 A. In situ, UV–Vis spectroelectrochemical studies on the initial stages of copolymerization of aniline with diphenylamine-4-sulphonic acid. Electrochim Acta 2001;46:1071–1085.
[26] Chen Y, Zhang X, Yu P, Ma Y. Stable dispersions of graphene and highly conducting graphene films: a new approach to creating colloids of graphene monolayers. Chemical Communications 2009;0:4527–4529.
[27] Sestrem R, Ferreira D, Landers R, Temperini M, Nascimento G. Structure of chemically prepared poly-(para-phenylenediamine) investigated by spectroscopic techniques. Polymer 2009;50:6043–6048.
[28] Zengin, Zhou, Jin, Czerw, Smith DW, Echegoyen, Carroll DL, Foulger SH, Ballato J. Carbon Nanotube Doped Polyaniline. Adv Mater 2002;14:1480–1483.
[29] Huang X, Hu N, Zhang L, Wei L, Wei H, Zhang Y. The NH3 sensing properties of gas sensors based on aniline reduced graphene oxide. Synthetic Metals 2013;185-186:25-30.
[30] Huang W, MacDiarmid A. Optical properties of polyaniline. Polymer 1993;34:1833–1845.
[31] Huang X, Hu N, Gao R, Yu Y, Wang Y, Yang Z, Kong E,Wei H, Zhang Y. Reduced graphene oxide–polyaniline hybrid: Preparation, characterization and its applications for ammonia gas sensing. Journal of Materials Chemistry 2012;22:22488–22495.
[32] Ding M, Tang Y, Gou P, Reber MJ, Star A. Chemical sensing with polyaniline coated single-walled carbon nanotubes. Advanced Materials 2011;23:536–40.
[33] Huang J, Zhang L, Chen B, Ji N, Chen F, Zhang Y, Zhang Z. Nanocomposites of size-controlled gold nanoparticles and graphene oxide: Formation and applications in SERS and catalysis. Nanoscale 2010;2: 2733-2738.

Chapter 4 - Optical gas sensors based on carbon nanotubes

4.1 Transparent carbon nanotube film as sensitive material for surface plasmon resonance based optical sensors

4.1.1 Introduction

Carbon nanotubes (CNTs) present properties that are unique with high electrical and thermal conductivity [1] elevated mechanical properties [2] . The high surface/volume ratio, the strong sensitivity of the electrical properties to the external ambient [3] make them ideal material for many kind of sensors such as strain sensors [4] , FET sensors [5] , electrochemical biosensors [6] and gas sensors [7] . Moreover CNTs are also interesting since they conserve their electrical properties also in thin transparent films [8] , suggesting the possible application for optically sensitive transparent films.

The CNTs can be divided in two categories: Single Wall Carbon Nanotubes (SWCNTs) and Multi Wall Carbon Nanotubes (MWCNTs). The former consist of a single tubular graphene sheet, the latter display a concentric arrangement of such tubes along the longitudinal axis with a interlayer spacing of 3.4 A [9] .

SWCNTs differentiate in two categories due to their electrical properties. The different chirality and diameter affects the behavior of the nanotube and they can be discriminated to semiconductor or metallic [10] . The chirality (n,m) rules the electrical behavior, if $|m–n|=3k$ is metallic, if $|m–n|=3k\pm1$ the tube is semiconductive [11] .

The properties of MWCNTs are ruled by the chirality and diameter of the outer tube because of the weak inter-shell interactions [12] . Hence, a mat of MWCNTs is usually composed of metallic and semiconductive MWCNTs [13] .

Previous studies suggest a different behavior of metallic SWCNTs (m-SWCNTs) and semiconductor (s-SWCNTs) toward gases [14] , [15] , [16] , meanwhile MWCNTs display a semiconductive behavior [17] [18] [17] . The s-SWCNTs and MWCNTs have been largely employed for their p-type conductance, meanwhile it is theorized that the molecule adsorption can induce a local charge fluctuation in the contact region of the nanotube [19] .

The addition of metallic nanoparticles (NPs) to CNTs is largely exploited to improve the sensitivity of CNTs toward a wider range of gases. In particular for hydrogen sensing, palladium [20] and platinum [21] [22] are largely employed, while the coupling with gold NPs is less exploited.

The gold NPs interact weakly with pristine SWCNTs [23] and tend to bond to the defective sites of the SWCNTs [24] . Theoretical [23] and experimental [14] studies of interaction of gases with gold nanoclusters demonstrate a weak interaction between Au clusters and CNTs, without a deep exploration of the specific gas sensing properties of the coupled nanomaterials. In addition, Au NPs play an amplification role of the interaction between the gas molecules with the sensitive material due to the Localized Surface Plasmon resonance (LSPR) [13] , increasing the interest in optical gas sensing properties of the nanocomposites.
In the following we demonstrate the possibility to develop transparent optical gas sensor based on CNTs coupled with Au NPs. The coupling between the CNTs and the Au NPs has the aim of combining the reactivity of the nanotubes towards hazardous gases, such as H_2, CO, NO_2 and aromatic Volatile Organic Compounds (VOC) with the LSPR of gold NPs. The LSPR is known to be extremely sensitive to the changes in the dielectric properties of the surrounding medium, a characteristic that has been widely exploited for the preparation of sensing devices.
While the use of SWCNTs and MWCNTs for gas sensing has been covered in multiple reports, little attention has been directed in exploring the different behavior of the metallic and semiconductive carbon nanotubes as optical sensing materials and, to the best of our knowledge, this is the first time that m-SWCNTs are used as sensing materials within optical sensors for the detection of reducing and oxidizing gases.

4.1.2 Experimental section

4.1.2.1 Preparation of gold monolayers

Au NPs were prepared with the procedure described in Appendice A2.1 and the monolayers were produced with the procedure illustrated in Appendice A2.14.
Then, a stabilization treatment at 400°C was accomplished to achieve structural stability at high temperature.

4.1.2.2 Deposition of carbon nanotubes by dropcasting

The preparation strategy for the CNTs layer is given in Figure 4.1.1. The substrates were first functionalized with Poly-L-Lysine. Then, dropcasting of a water solution of CNT is dropcasted and left to sediment for a period ranging from 3 to 24hours. Rinsing of the

samples with water and drying with air flow follow. The detailed description of the deposition technique is reported in A.2.15.

The deposition period was varied from 3 to 20 hours for the different solutions of CNTs in order to achieve a coverage of the surface homogeneous among all the samples prepared.

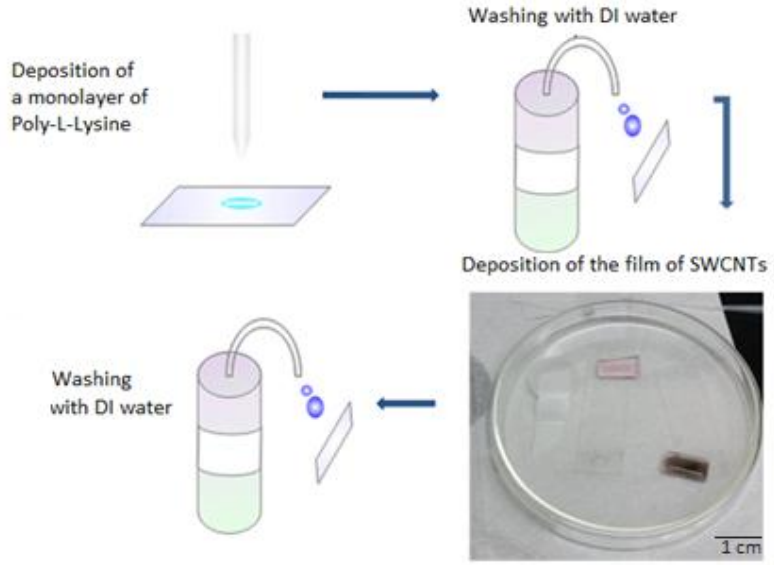

Figure 4.1.1 - Deposition procedure with dropcasting technique.

At first, the depositions were conducted on soda-lime substrates to draw the parameters for the deposition of the finals sensors. Hence, the concentration of the solutions and the deposition period were adjusted to achieve a uniform value of electrical resistance of the samples.

The material used for deposition were purchased from Nanointegris (IsoNanotube-S and IsoNanotube-M) and from NanoLab (Nink-1000).

The SWCNTs were deposited also by ink-jet printing using a SonoPlot Microplotter GIX II. The printing procedure is reported in ref. [25] .

The SWCNTs and MWCNTs films were heat treated in air at 300 °C for one hour.

4.1.2 Optical gas sensing measurements

Optical gas sensing measurements were carried at operating temperature (OT) of 150°C and 300°C. All the samples were tested with H_2(10000ppm), CO(10000ppm), NO_2(1ppm) in synthetic air.

The detailed description of the gas sensing apparatus is reported in appendix A.3.
The samples deposited by dropcasting were tested also toward the aromatic volatile organic compounds, such as toluene(10000ppm), xylene (10000ppm) and benzene(10000ppm) in nitrogen carrier at 150°C and 300°C OT.

4.1.3 Set-up of the parameters for dropcasting of SWCNTs

The first set of depositions was conducted for a period of 6h, with the solutions as purchased:

1. Semiconductive SWCNTs of 0,.01mg/ml
2. Metallic SWCNTs of 0.01 mg/ml
3. MWCNTs of 0.5 mg/ml

No conductivity was recorded from the films obtained. To increase the thickness of the film the starting solutions were diluted down with a solution of Sodium Dodecyl Benzen Sulfate, SDBS (10%v/v) in water. The SDBS acts as a surfactant for CNTs in water and enhances their affinity to the polylisine, allowing an increase in thickness of the final films [26].
As a rough measure of thickness of the samples the electrical resistance was measured with an electrical tester. The resistance obtained is in a short range of value for the samples, that can be considered of similar thickness.
The final sensors were prepared with the parameters presented in Table 1.

Solution	Concentration (µg/ml)	Time	Resistance (MΩ)
Semiconductive SWCNTs	3.3	20h	0.5
Metallic SWCNTs	3.3	20h	5-30
MWCNTs	170	5h	3

Table 4.1.1 – Parameters of deposition for the final sensors and resistance measured with a tester.

4.1.4 Optical characterization

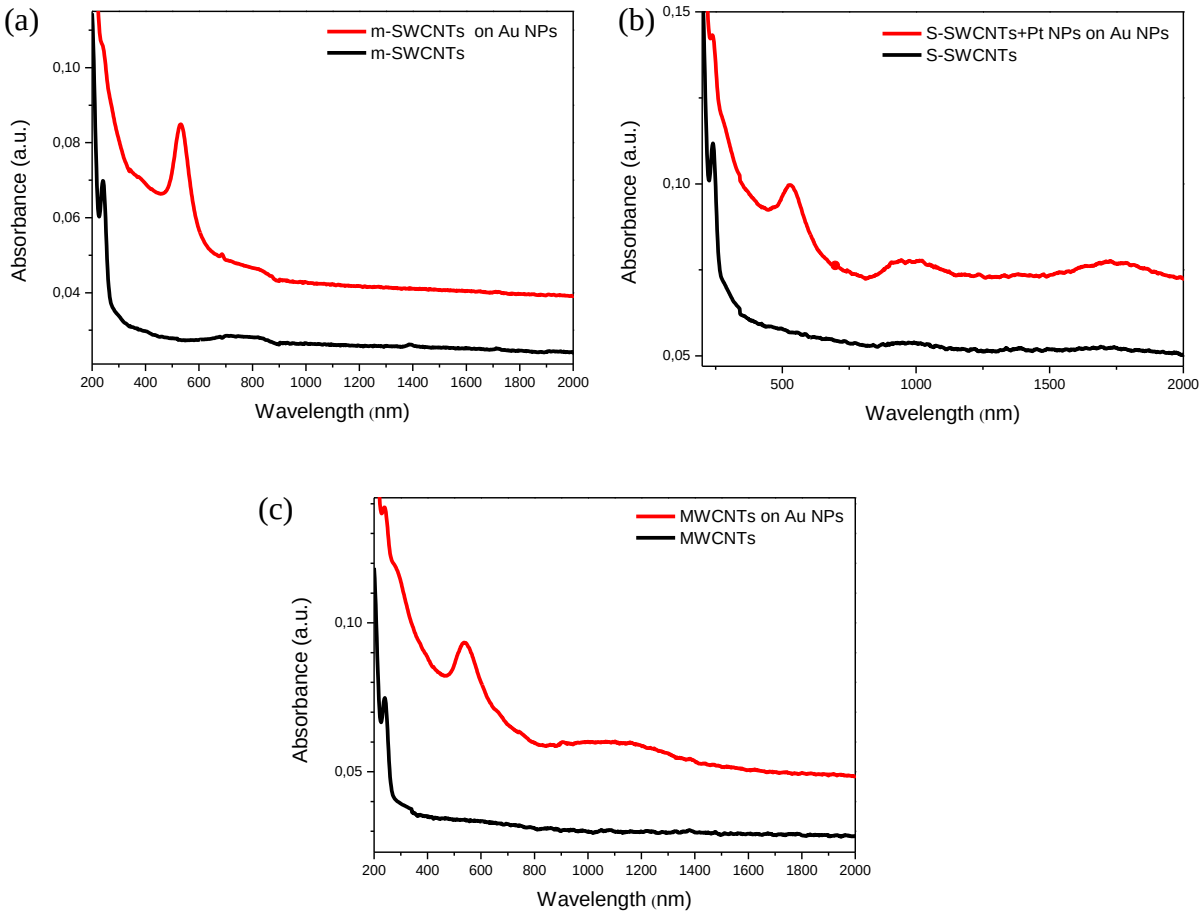

Figure 4.1.2 - a) UV/Vis absorbance spectra of a) m-SWCNTs; (b) s-SWCNTs; (c) MWCNTs on Au NPs and on bare silica substrates.

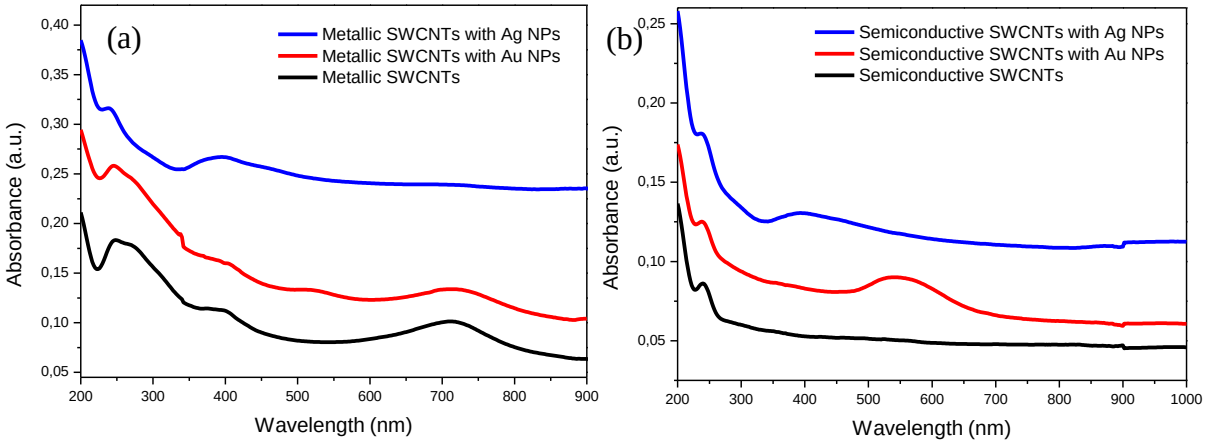

Figure 4.1.3 - a) UV/Vis absorbance spectra of printed m-SWCNTs: on Ag NPs, on Au NPs, on bare Silica; b) UV/Vis absorbance spectra of printed s-SWCNTs: on Ag NPs, on Au NPs, on bare Silica.

The samples prepared with dropcasting were characterized by UV/Vis/NIR absorption spectroscopy and reported results are reported in Figure 4.1.2. The M11 (~ 700nm) of metallic SWCNTs and S11 (~ 980nm) and S22(~ 1740nm) peak of the semiconductive carbon nanotubes are clearly present in the spectra 4.1.2a and 4.1.2b [27] . MWCNTs display a broad band at transition at ~ 1150nm of the S22 transition (see Figure 4.1.2c)..

The optical spectra of the sensors obtained with ink-jet printing are reported in Figure 4.1.3. The features of metallic SWCNTs, can be recognized in the spectra. The S11 and S22 peak of semiconductive SWCNTs are not visible since they lay in the NIR. The presence of Au and Ag NPs is confirmed by the presence of their characteristic LSPR absorbance peaks respectively at 530nm and 390nm.

The samples produced with the dropcasting method and with the ink-jet printing present a remarkable transparency in the visible range. In Figure 4.1.4 two samples of m-SWCNTs deposited on Au NPs are showed: the film on the left is obtained with dropcasting technique and that on the right with the ink-jet printing. The dropcasting method allows a facile and transparent covering of all the surface of the substrate, which is pink due to the absorption of the Au LSPR. The ink-jet printer permits the deposition of the film in a localized area as the slightly dark transparent square on the sample on the right side of Figure 4.1.4a. The slightly dark color of the area suggests the presence of a higher quantity of carbon nanotubes with respect to the sample on the left.

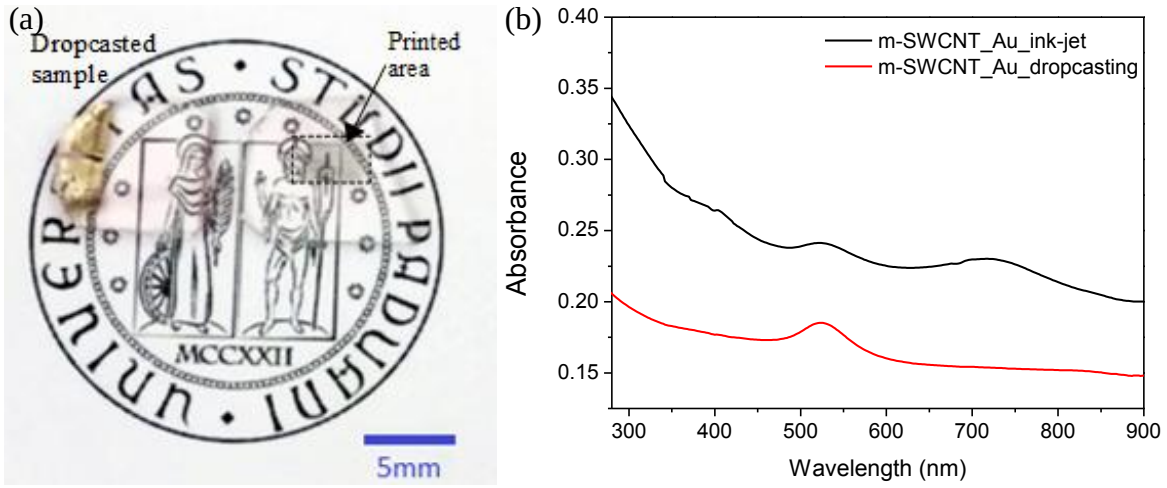

Figure 4.1.4 – a) image of m-SWCNTs on Au NPs: dropcasted on the left side and ink-jet printed on the right side. The printed area is highlighted by a dotted square. b) UV/Vis absorbance spectra of m-SWCNTs on Au NPs: ink-jet printed (black line) and dropcasted (red line).

Figure 4.1.4b shows the UV/Vis spectra of the two samples presented in Figure 4.1.4a. The sample with the printed film has a stronger absorbance in the whole range of analysis due to a larger cross section of the m-SWCNTs layer interacting with the incoming beam. In addition, the absorbance spectrum of the printed film displays evident characteristic features of the metallic SWCNTs with a more intense absorbance in the UV range and the peak due to the Van Hove transition at ~700 nm [28].

The presence of the gold NPs is confirmed by the presence of the LSPR peak at ~530 nm. The LSPR peak is less evident in the ink-jet printed sample due to the larger thickness of the carbon material above the Au NPs with respect to the drop casted film.

Figure 4.1.5 reports the absorbance spectra of the film of Au NPs alone, printed m-SWCNTs and m-SWCNTs printed on Au NPs. The spectrum of the sample with both the nanomaterials presents the characteristic features of both Au NPs, with the LSPR peak at 530nm and the UV/Vis peak of the π conjugation and the Van Hove transitions at 400 nm and 700 nm [28], [29], respectively.

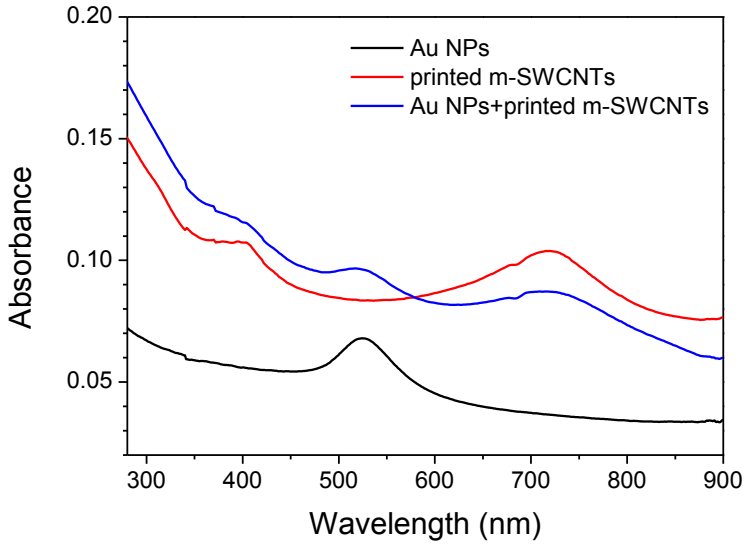

Figure 4.1.5 – UV/Vis absorbance spectra of the samples with Au NPs (black line), printed metallic SWCNTs (red line) and of printed metallic SWCNTs on Au NPs (blue line).

4.1.5 Morphological characterization

SEM image of the nanostructure of Au NPs with dropcasted s-SWCNTs is reported in Figure 4.1.6a. The film is composed of a monolayer of gold NPs with a high coverage of the substrate. The carbon nanotubes layer is thick and partially masks the quartz substrate below. The Au NPs stand out among the bundles of s-SWCNTs. This implies that the thickness of the layer of s-SWCNTs is lower of the dimension of the Au NPs. Similar image have been collected also for the Au monolayer coated with m-SWCNTs. From SEM images it is possible to note Au NPs with a diameter ranging from 20 up to 40 nm, in accordance with [30] . XRD measurements also confirmed the presence of crystalline Au NPs in the nanocomposites (see Figure 4.1.6b).

Spectroscopic ellipsometry was used to estimate the refractive index of both thickness s-SWCNTs and m-SWCNTs deposited by drop casting. Considering the SEM image reported in Figure 4.1.6b, we assumed a continuous film composed of a fraction of air and a fraction of carbon nanotubes. The thickness of both SWCNTs layers was estimated to be 8 nm and the refractive index at λ=630 nm was n=1.37, in agreement with [31] .

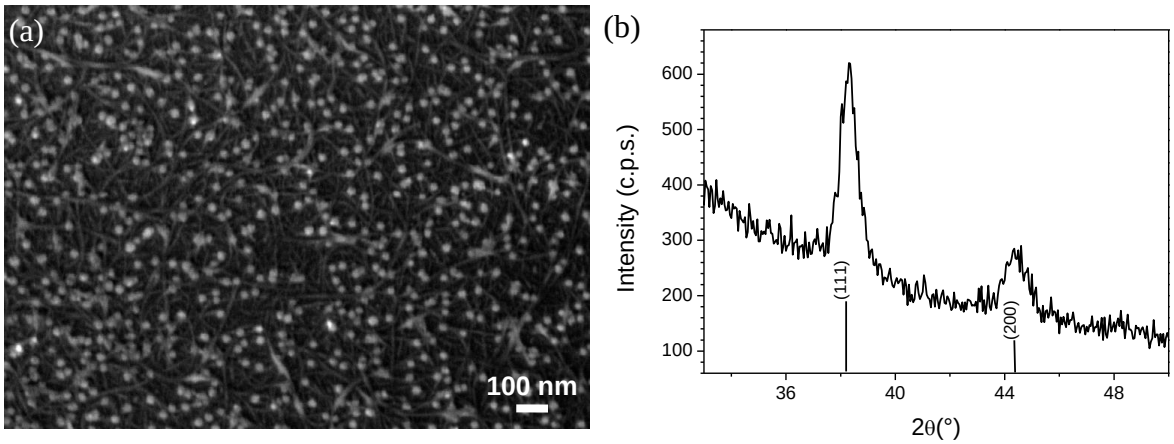

Figure 4.1.6 – a) SEM picture of s-SWCNTs on Au NPs obtained by drop casting. b) XRD pattern of Au monolayer coated with ink-jet printed s-SWCNTs.

AFM measurements were conducted to have a confirmation of the thickness evaluated by ellipsometry. In Figure 4.1.7 the printed metallic SWCNTs form bundles covering the whole surface. The carbon nanotubes appear not homogeneously distributed with areas of higher accumulation with a value of the average thickness of 29nm. Instead, the thickness of

the dropcasted films of m-SWCNTs is ~10 nm, confirming the data of the ellipsometric analysis.

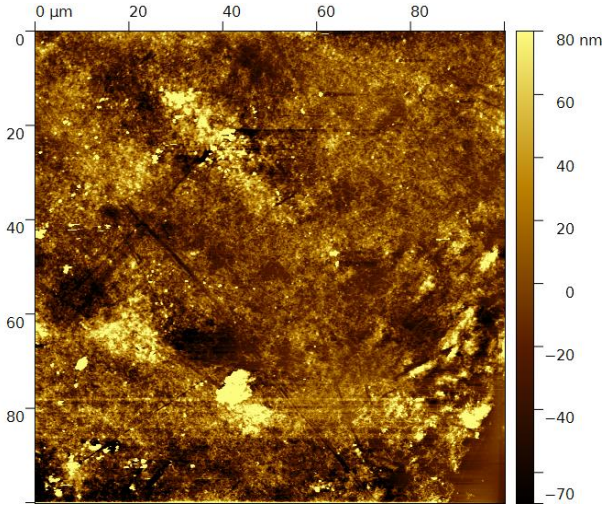

Figure 4.1.7 –a) AFM image of m-SWCNTs by ink-jet printing.

4.1.6 Optical gas sensing measurements

Optical gas sensing measurements were carried at operating temperature (OT) of 150°C and 300°C. All the samples were tested with H_2(10000ppm), CO(10000ppm), NO_2(1ppm) in synthetic air.

The detailed description of the gas sensing apparatus is reported in appendix A.3.

4.1.6 Gas sensing of dropcasted CNTs toward aromatic VOC

The samples obtained with dropcasting techniques have been tested toward aromatic volatile organic compounds, Benzene(10000ppm), Toluene(10000ppm), Xylene(10000ppm) balanced in N_2. The tests were carried at 150°C and 300°C and are showed in Figure 4.1.8, 4.1.9, 4.1.10.

All the films don't show any variation with the introduction of the aromatic VOC in the chamber.

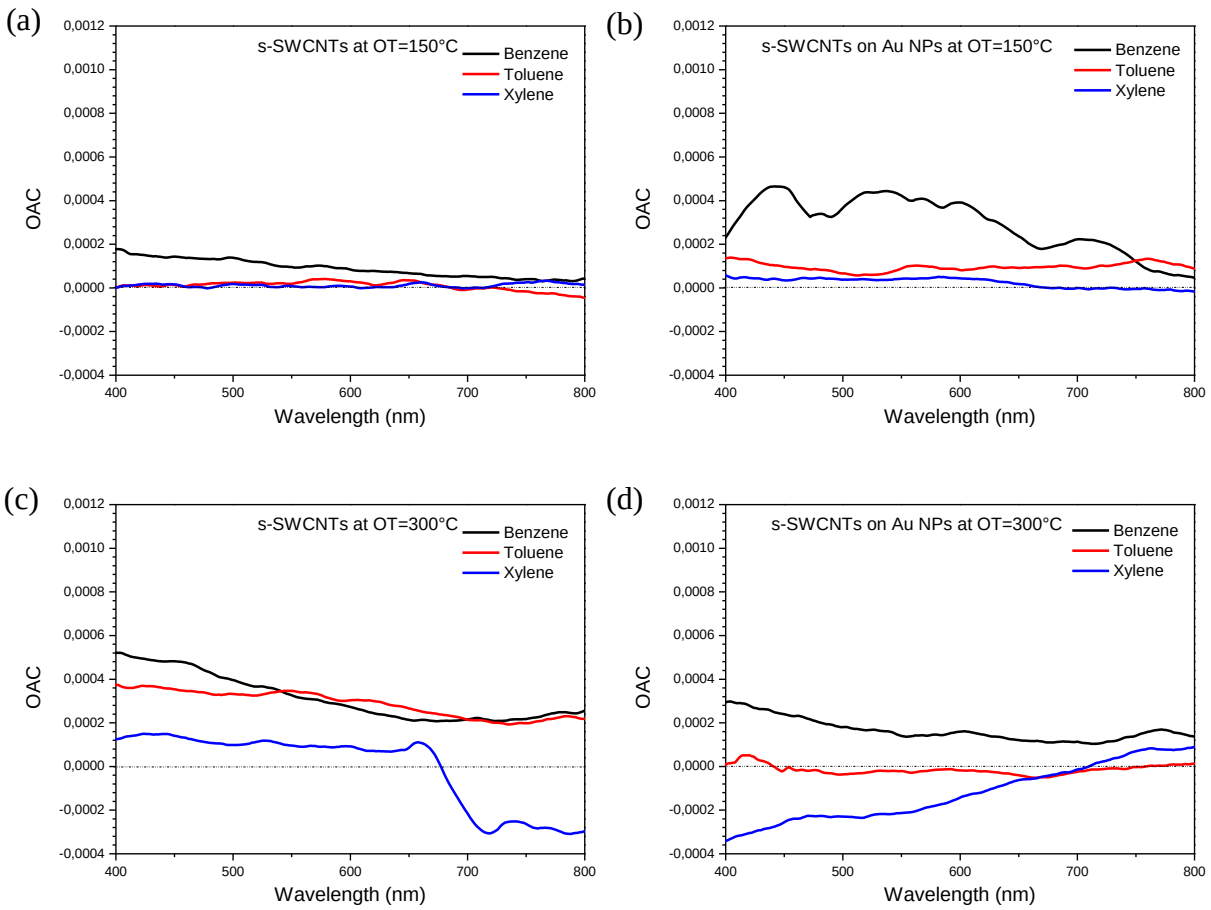

Figure 4.1.8 - OAC plots of dropcasted s-SWCNTs toward aromatic VOC compounds: a) on bare SiO_2 at OT=150°C; b) on Au NPs at OT=150°C; c) on bare SiO_2 at OT=300°C; c) on Au NPs at OT=300°C;

Aromatic VOC gases don't cause an appreciable variation in optical properties of the CNTs. CNTs have proved sensitive as chemoresistors with two mechanism, the adsorption on the surface and direct charge transfer, and the adsorption in intertube junctions enhancing the hopping mechanism of conduction [32] . These mechanisms significantly alter the conductivity of the mats of CNTs but appear to have low impact in the optical gas sensing of CNTs toward aromatic VOC.

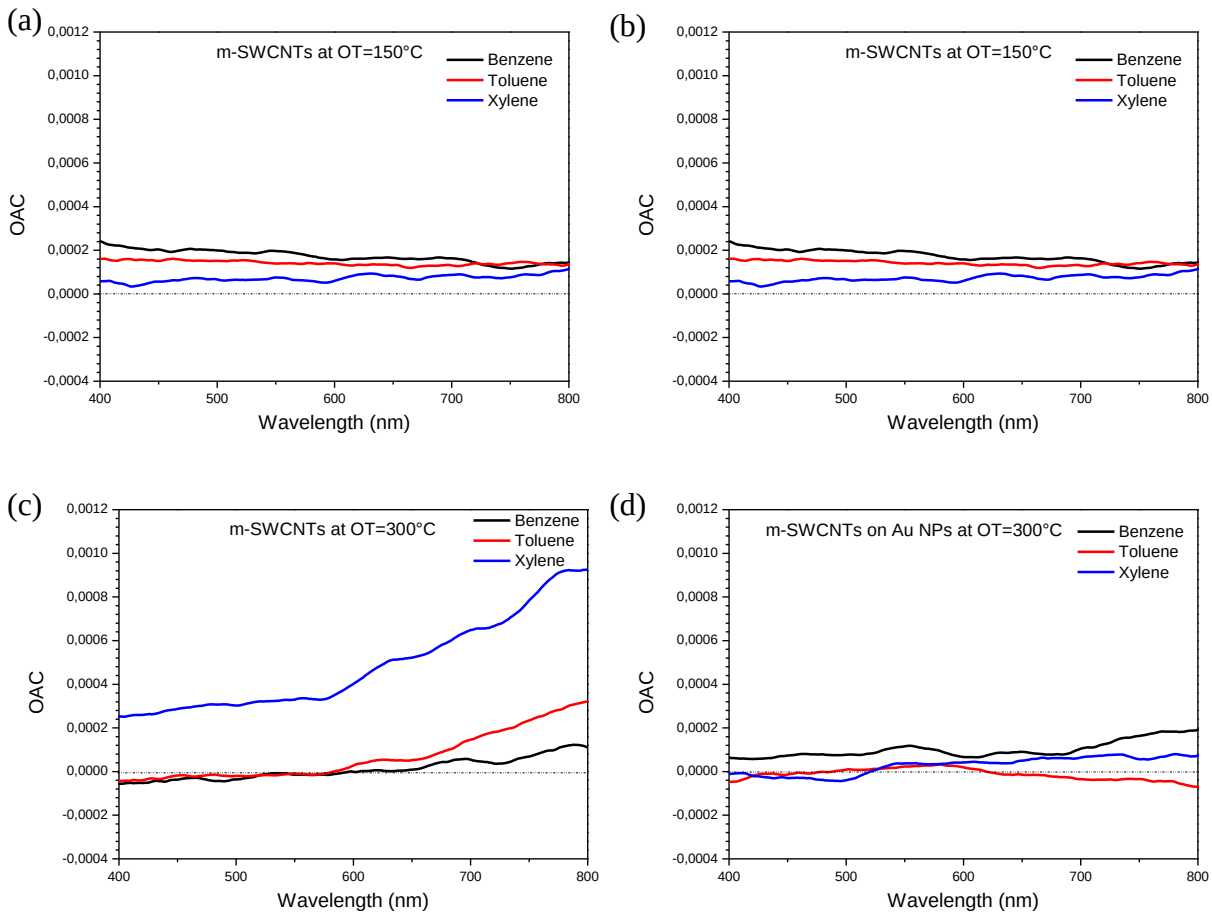

Figure 4.1.9 – OAC plots of dropcasted m-SWCNTs toward aromatic VOC compounds: a) on bare SiO_2 at OT=150°C; b) on Au NPs at OT=150°C; c) on bare SiO_2 at OT=300°C; c) on Au NPs at OT=300°C;

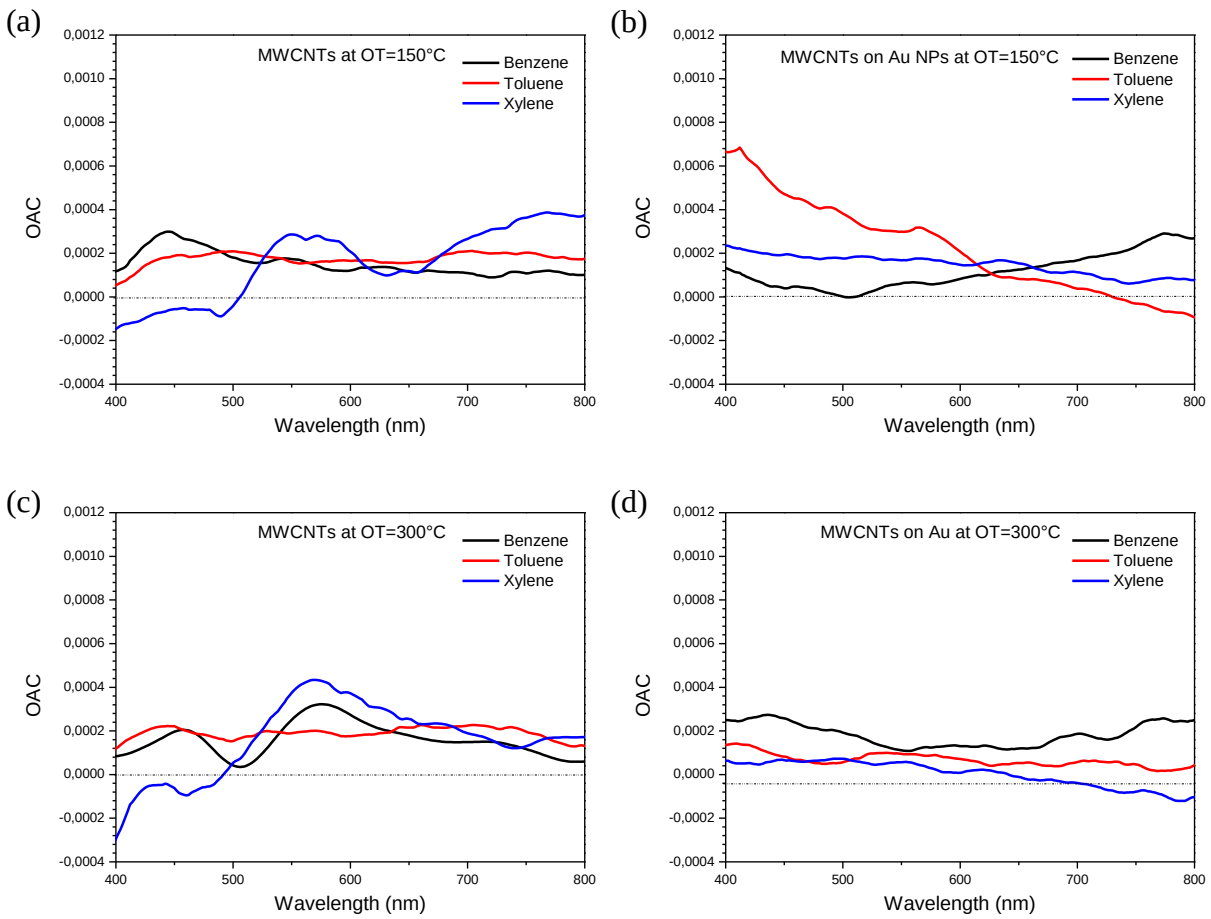

Figure 4.1.9 – OAC plots of dropcasted MWCNTs toward aromatic VOC compounds: a) on bare SiO_2 at OT=150°C; b) on Au NPs at OT=150°C; c) on bare SiO_2 at OT=300°C; c) on Au NPs at OT=300°C;

4.1.7 Gas sensing properties of CNTs toward oxidizing/reducing gases

4.1.7.1 Gas sensing tests at 150°C of printed SWCNTs.

The OAC plots of the films obtained by ink-jet printing are pictured in Figure 4.1.10.

The semiconductive SWCNTs alone don't display a remarkable variation of absorbance. The film of m-SWCNTs shows a slight increase in absorbance in correspondence of the M11 transition at ~700nm, when exposed to H_2(1%), visible in Figure 4.1.10b.

Metallic SWCNTs coupled with silver nanoparticles present poor variation in optical absorbance in proximity of the LSPR peak of the Ag NPs, as can be observed in Figure 4.1.10.d. In Figure 4.1.10.c, the s-SWNCTs on Ag NPs presents similar variations for oxidizing (NO_2) and reducing gases (H_2, CO).

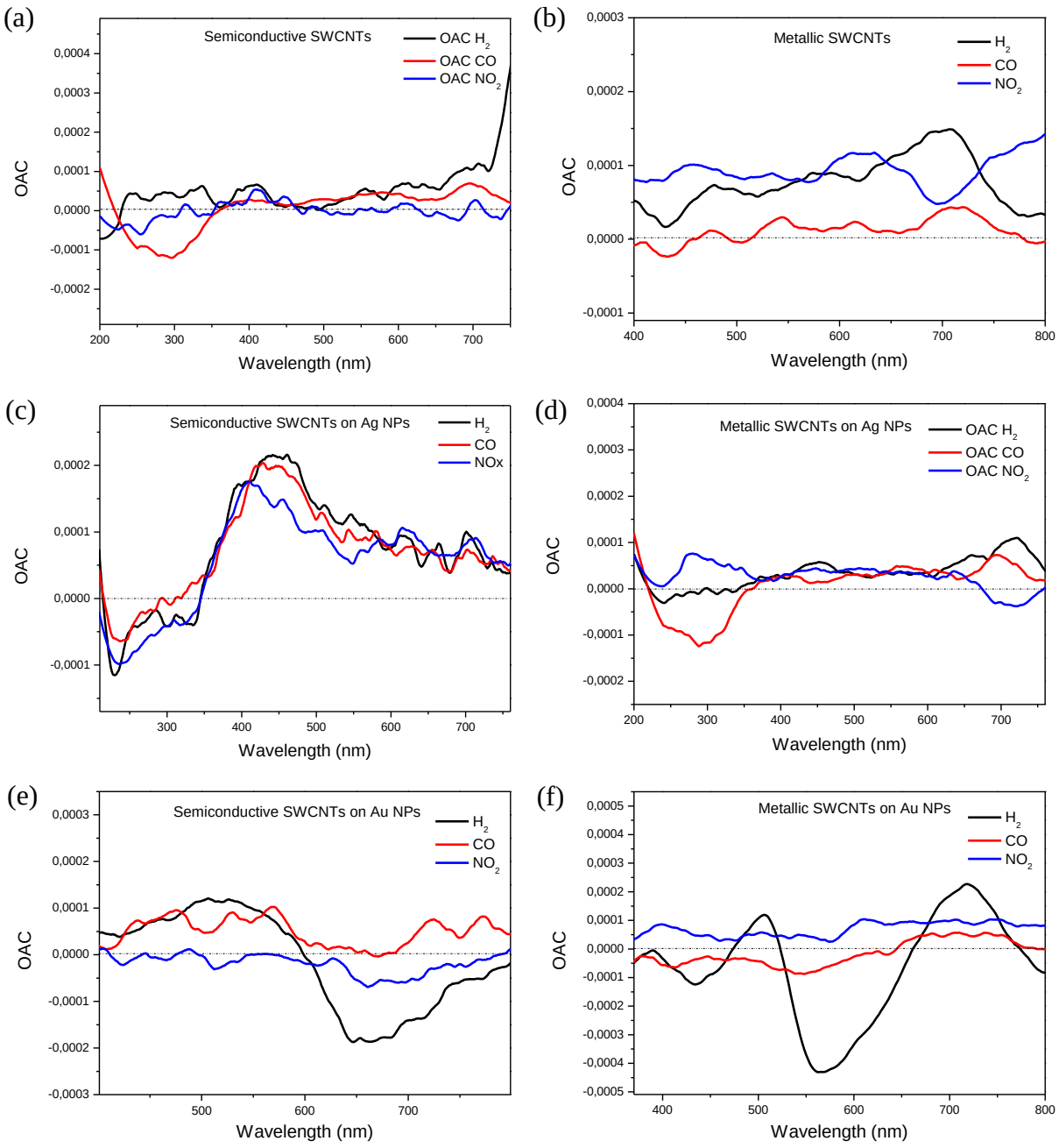

Figure 4.1.10 – OAC plots of printed SWCNTs recorded at the operating temperature of 150°C relative to a) s-SWCNTs; b) m-SWCNTs; c) s-SWCNTs on Ag NPs d) m-SWCNTs on Ag NPs; e) s-SWCNTs on Au NPs; f) m-SWCNTs on Au NPs.

Figures 4.1.10e and 4.1.10f display the improvement in sensitivity of the SWCNTs with the addition of Au NPs. Both the films display a variation in absorbance in the wavelength range of the LSPR peak of Au NPs in H_2(1%) atmosphere.

The OAC plot of m-SWCNTs on Au NPs present a more intense variation in the range of wavelength around 550nm. It is possible to recognize the increase in absorbance at ~700nm in Figure 4.1.10f analogous to what observed with bare m-SWCNTs in hydrogen atmosphere, in Figure 4.1.10b.

4.1.7.2 Gas sensing tests at 300°C of printed SWCNTs

The tests effectuated at 300°C highlight better what is observed at the lower operating temperature.

In Figure 4.1.11b we observe a variation in absorbance of the samples with Ag NPs during the exposure to different atmospheres. This is related to a lack of stabilization of the Ag NPs at high temperature and in particular at 300°C due to NPs oxidation and coalescence.

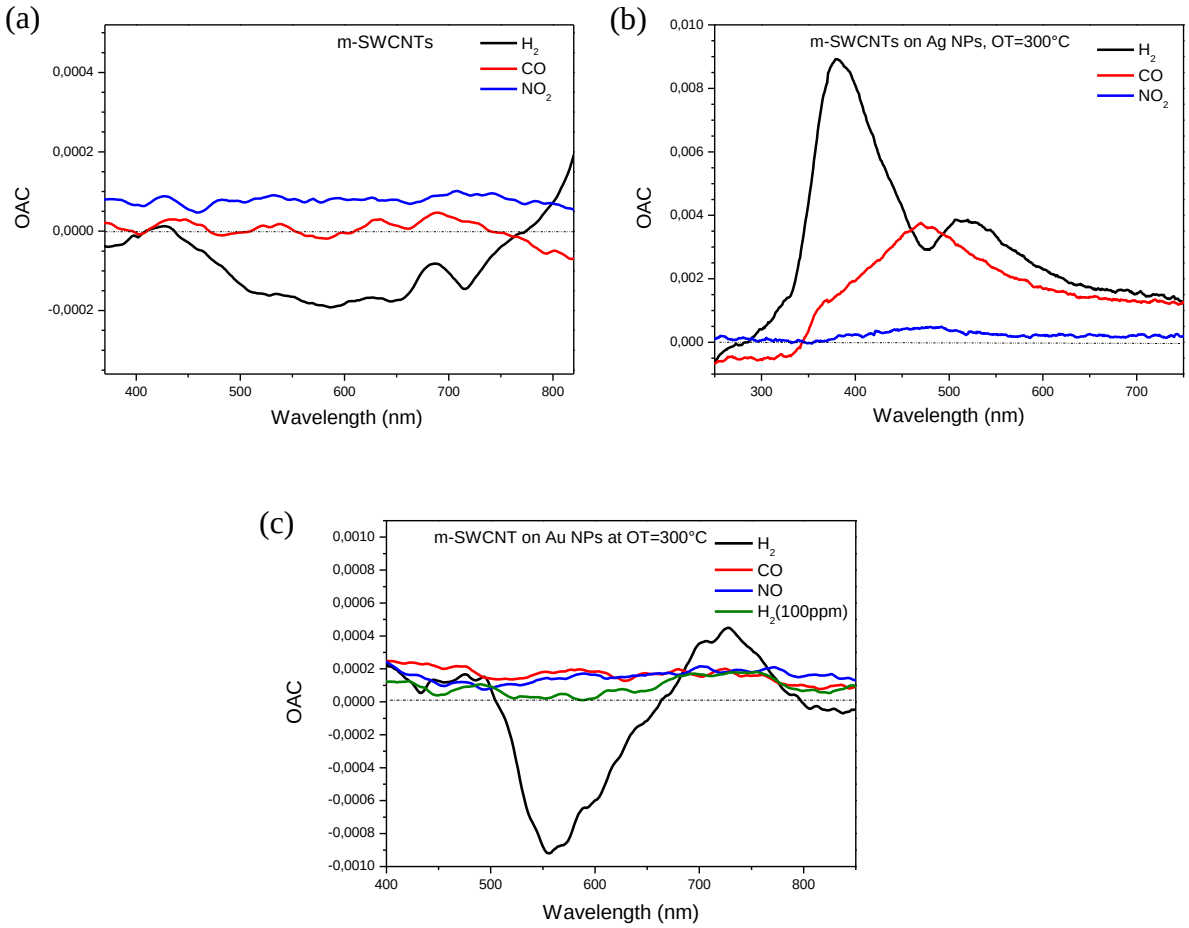

Figure 4.1.11 – OAC plots of printed SWCNTs tested at OT=300°C: a) m-SWCNTs; a) m-SWCNTs on Ag NPs; a) m-SWCNTs on Au NPs.

In Figure 4.1.11c, m-SWCNTs on Au NPs exhibit a remarkable change in absorbance when exposed to H_2(1%) .

Au NPs reveals to be necessary for the gas sensing response of the m-SWCNTs. The rising in operating temperature appear to increase the photoactivity of the nanostructure. Also at 300°C we can note an increase in absorbance at 700nm, where the electron transition of m-SWCNTs lays.

It was not possible to run measures on printed semiconductive SWCNTs at 300°C. Consequently, fresh thin films of SWCNTs were produced (as reported above in 4.1.22) to investigate the sensing properties of SWCNTs.

They were prepared with dropcasting method to investigate the effect of the deposition technique on the sensing properties and MWCNTs have been also taken into account.

4.1.7.3 Gas sensing tests at 150°C of dropcasted SWCNTs

The OAC plots of SWCNTs deposited by dropcasting obtained at 150°C are shown in Figure 4.1.12.

The thin films of only mats of s-SWCNTs, m- SWCNTs, and MWCNTs don't display a significant change in optical absorbance. The thin films of m- SWCNTs, in Figure 4.1.12c, don't display an increase in absorbance under H_2(1%) exposure, as observed with printed films.

Similar considerations can be drawn for the samples composed with Au NPs. The spectra have no alteration in the range of wavelength close to the LSPR peak of the metallic NPs.

The thickness of the films may not be thick enough to have an extensive interaction of the gas molecules with the carbon nanotubes to record an appreciable change of the optoelectonic properties of the CNTs mats.

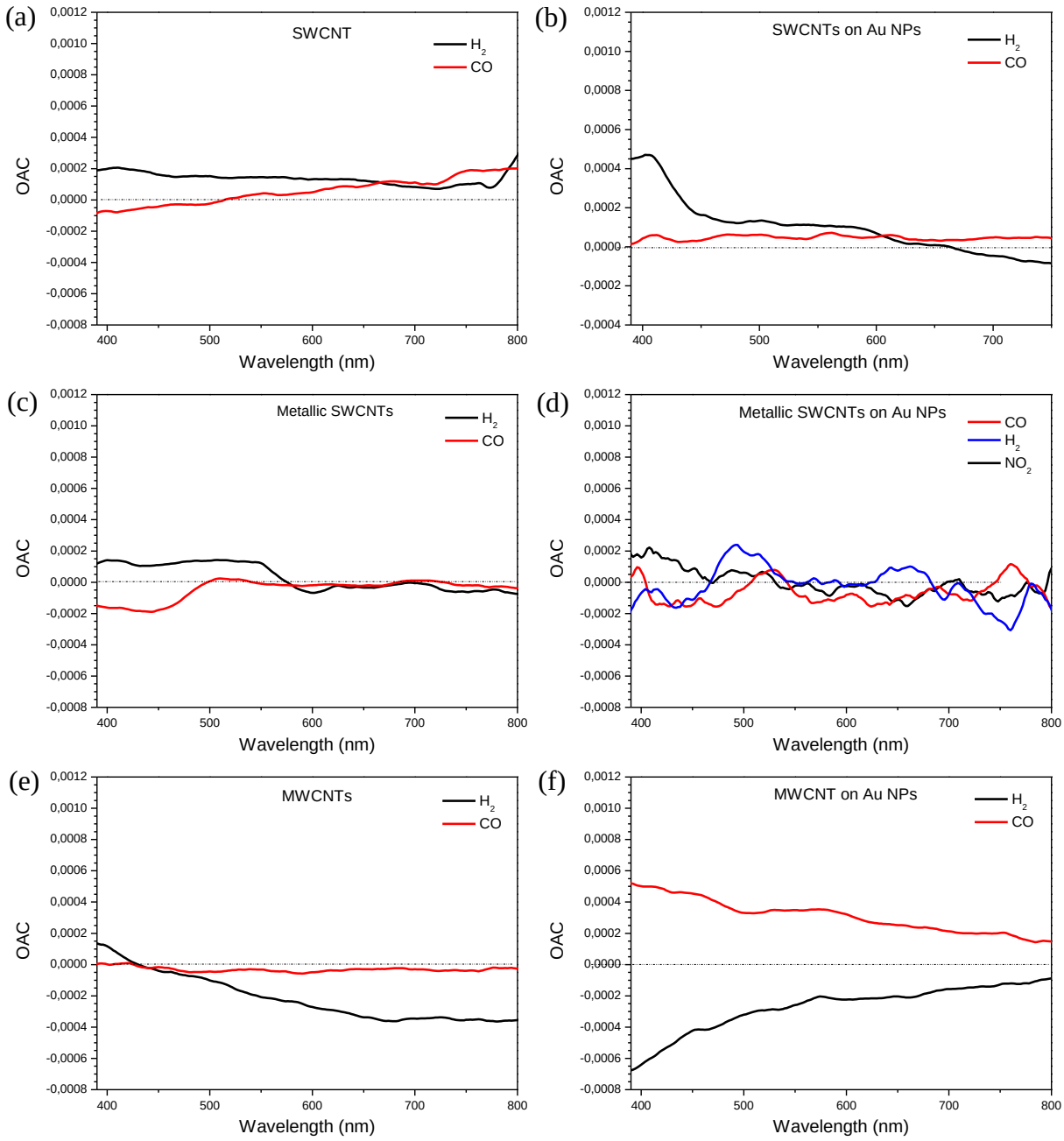

Figure 4.1.12 – OAC plots of dropcasted CNTs recorded at OT=150°C of: a) s-SWCNTs; b) s-SWCNTs on Au NPs; c) m-SWCNTs; d) m-SWCNTs on Au NPs; e) s-MWCNTs; f) MWCNTs on Au NPs.

4.1.7.3 **Gas sensing test**s at 300°C of dropcasted SWCNTs

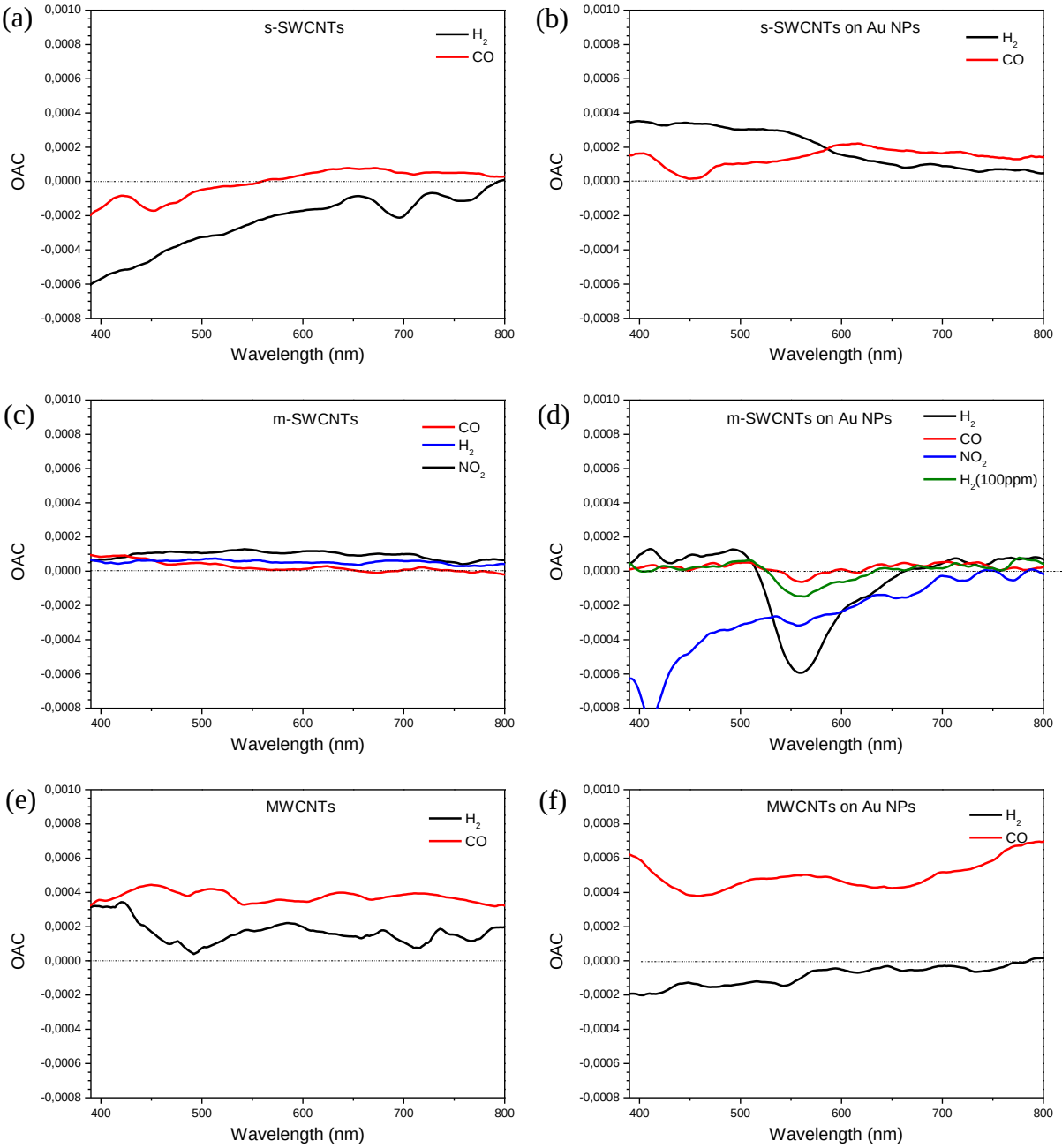

Figure 4.1.13 – OAC plots of dropcasted CNTs recorded at OT=300°C of: a) s-SWCNTs; b) s-SWCNTs on Au NPs; c) m-SWCNTs; d) m-SWCNTs on Au NPs; e) s-MWCNTs; f) MWCNTs on Au NPs.

Figure 4.1.13 displays the optical response of the CNTs to oxidizing and reducing gases at high temperature, OT=300°C.

The changes in absorbance observed for s-SWCNTs and MWCNTs alone or coupled with Au NPs are not significant and related to drift in optical absorbance at 300°C.

Figure 4.1.13c shows that m-SWCNTs are not affected in their optical properties when used alone, but after the addition of Au NPs they show a remarkable response to hydrogen gas, with an elevated variation to H_2(1%) and discrete change to H_2(100ppm) in optical property in the portion of visible light close to the LSPR peak of Au NPs. A variation smaller than the one related to the low concentration of H_2 can be noticed for CO(1%), as pictured in Fig. 4.1.13d.

As observed for printed samples the Au NPs activates the sensing properties of metallic SWCNTs and the high OT enhances the response of the nanocomposites in the static tests. Furthermore, the active role of Au NPs in H_2 detection, previously considered in section 3.1.4.5.1, has to be taken into account for a better understanding of the sensing mechanism at OT=300°C.

4.1.8 Gas sensing properties of the SWCNTs to hydrogen

To better understand the interplay between Au NPs and SWCNTs is necessary to focus on the gas sensing responses of the film at 150°C. The gas response provided relevant information about the gas sensing performances of the materials and about the two deposition techniques.

The best gas sensing response obtained was with the ink-jet printed samples and only those samples will be discussed.

Figure 4.1.15 shows the optical absorption spectra of m-SWCNTs and of s-SWCNTs on Au NPs acquired in dry air and in H_2. A blue-shift of the LSPR peak occurs for both the samples, and the variation is more accentuated in the case of m-SWCNTs.

The inset in Figure 4.1.15a displays the different behavior to H_2 of the bare Au NPs, the bare m-SWCNTs and the Au NPs covered with m-SWCNTs. Both bare Au NPs and bare m-SWCNTs did not show adequate sensing properties and the coupling of m-SWCNTs with Au NPs is fundamental to activate the optical sensing property of the material.

Figure 4.1.15b displays the results of similar tests with s-SWCNTs. Also in the case of s-SWCNTs the coupling with Au NPs is essential for getting a detectable variation of the

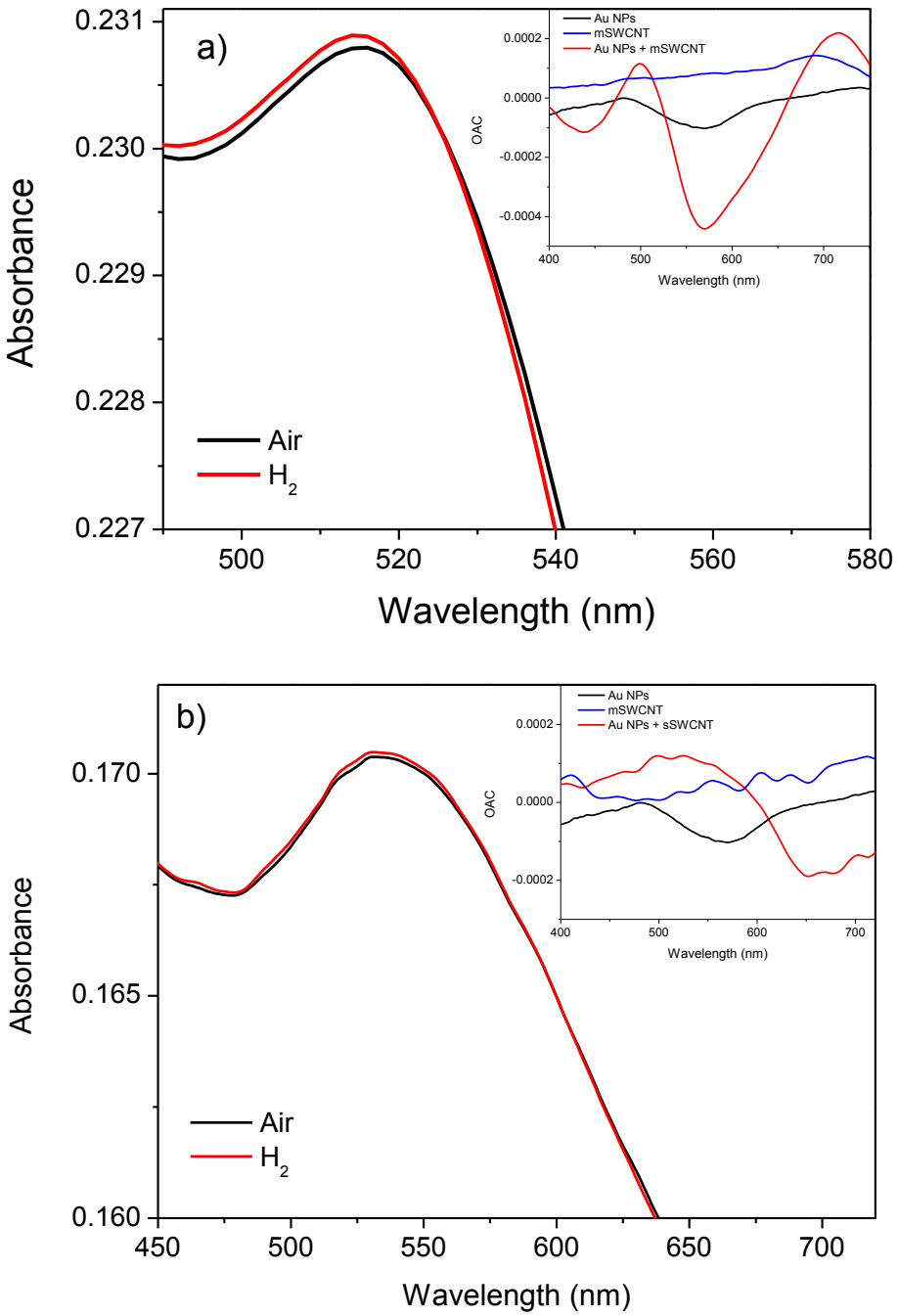

Figure 4.1.15 – a) Optical absorption spectra of m-SWCNTs on Au NPs deposited by ink-jet printer when exposed to air (black line) and H_2 (red line) at OT=150°C. The inset show the OAC of the bare Au NPs, bare m-SWCNTs and Au NPs covered with m-SWCNTs. b) Optical absorption spectra of s-SWCNTs on Au NPs deposited by ink-jet printer when exposed to air (black line) and H_2 (red line) at OT=150°C. The inset show the OAC of the bare Au NPs, bare s-SWCNTs and Au NPs covered with s-SWCNTs.

absorbance in the presence of H_2, but it is evident that the s-SWCNTs are less effective than the m-SWCNTs.

From the OAC spectra reported in the insets of Figure 4.1.15 it is possible to note that the maximum variation of the absorbance is obtained at λ=540 nm for s-SWCNTs and at λ=570nm and λ=700 nm for m-SWCNTs, which have been selected for the dynamic test.

The differences observed in the optical absorbance and OAC spectra are reflected in a sharper and faster variation in absorbance for the m-SWCNTs sample (see Figure 4.1.16) with respect to the s-SWCNTs sample (see Figure 4.1.17). Moreover the s-SWCNTs sample displays an evident drift (see Figure 4.1.17). Both s-SWCNTs and m-SWCNTs samples are almost insensitive to NO_2 and CO, while for the m-SWCNTs it was possible to detect a variation in absorbance also for 100 ppm of H_2 (see Figure 4.1.16).

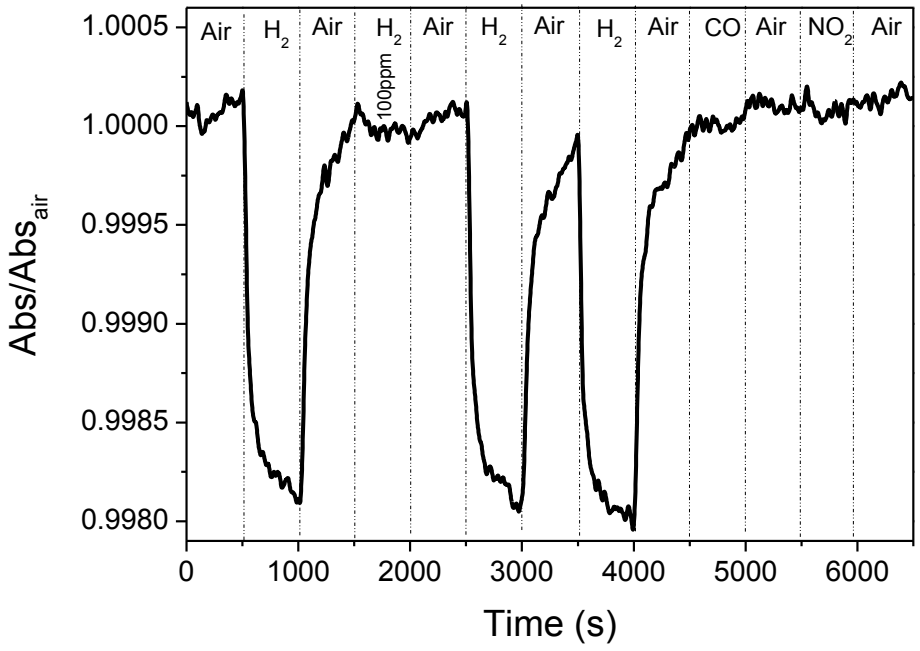

Figure 4.1.16 – Dynamic response of m-SWCNT deposited on Au NPs at λ = 570 nm and OT=150°C exposed to different air/gas cycles.

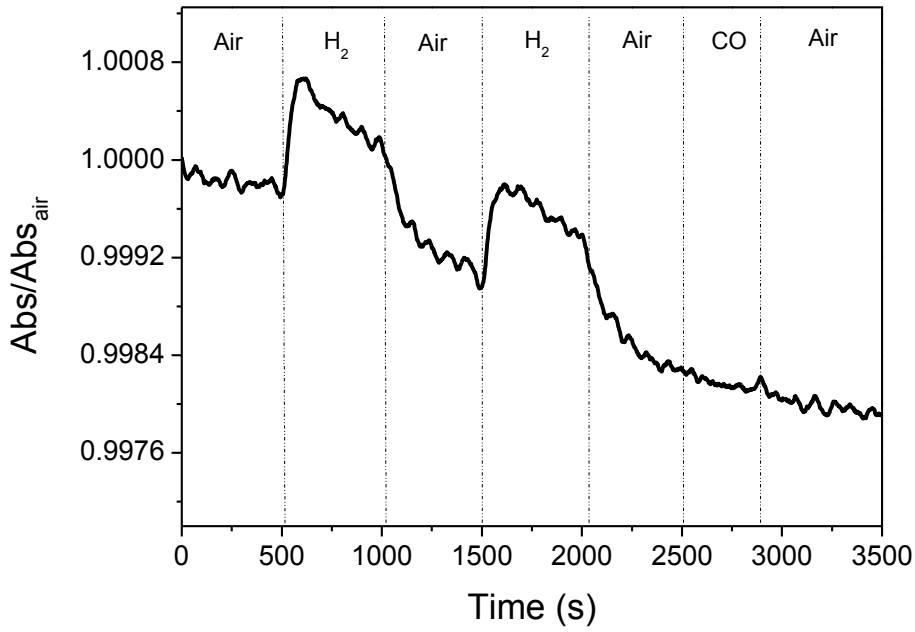

Figure 4.1.17 – Dynamic response of s-SWCNT deposited on Au NPs at λ=540 nm and OT=150°C exposed to different air/gas cycles.

The interaction of hydrogen in principle can occur directly on Au NPs, at the interface between them and the SWCNTs and on the SWCNTs itself. The first hypothesis implies a response to hydrogen of the lone Au NPs monolayer. However the response is negligible compared to the one observed for the sample made of Au NPs coated with SWCNTs, as reported in the insets of Figure 4.1.15. This implies a direct interaction of hydrogen with the SWCNTs. On the other hand, the bare SWCNTs did not show any relevant variation in absorbance when exposed to H_2, so we can suppose that the interaction between H_2 and the SWCNTs is probed by the Au NPs. In particular such interaction is more effective in the case of m-SWCNTs for which it is evident a blue shift of the Au LSPR peak (see Figure 4.1.15). Such blue shift can be due to a decrease of the refractive index of the medium surrounding the Au NPs or to an increase of the oscillating electrons in the Au NPs [34] . Spectroscopic ellipsometry measurements on SWCNTs film under H_2 exposure did not show any variation of the refractive index, so the charge transfer appears as the most plausible mechanism behind the blue-shift of the Au NPs. This is also confirmed by the increase of the peak related to the M11 transition at 700 nm that can be related to an increase in density of electron in the SWCNTs [35] , [36] .

As already reported in literature, hydrogen molecules can be split on CNTs [37] , [38] [39] and atomic hydrogen can also spillover allowing charge transfer from hydrogen to carbon nanotubes [38]' [40] . In addition, atomic hydrogen can react with oxygens that are adsorbed on the surface of SWCNTs when exposed to air [41] . In the case of SWCNTs in contact with Au NPs, electrons exchange can occur, as already reported for conductometric gas sensors [42] .

It is plausible to suppose a more efficient transfer with m-SWCNTs due to the ohmic contact at the interface between m-SWCNTs and the Au NPs. The s-SWCNTs present a localized Schottky barrier at the interface with the Au NPs that may hinder the charge transfer and the coupling with the Au NPs [23] . This phenomena may be the cause of the negligibly low sensing efficiency of the s-SWCNTs.

The interaction with CO and NO_2 was ineffective. The chemisorptions of NO_2 is favored in carbon nanotube but the low concentration (1ppm) can present a severe limit to the detection [43] , on the other hand CO interacts weakly with carbon nanotubes [44] . Moreover the heat treatment at 300 °C could remove the preferential adsorption sites for CO, such as defects or functional groups [44] .

The results obtained at 300°C OT are now considered. As for the tests at OT=150°C, the Au NPs activate the sensing response to H_2(1%), see Figure 4.1.20.

The time resolved scans of the films of SWCNTs on Au NPs, in Figure 4.1.18 and 4.1.19, exhibit strong variation in the entity and period of the signal of the relative absorbance variation, when exposed to H_2(1%).

In addition, 300°C OT allows the sensitization of the films deposited by dropcasting as reported in Figure 4.1.19. The performance achieved by the thin film of SWCNTs on Au NPs are inferior than those relative to the analogous printed film in Figure 4.1.18. Both exhibit a fast and sharp response, but the lower thickness of the film appear to penalize the performance of the dropcasted nanostructures .

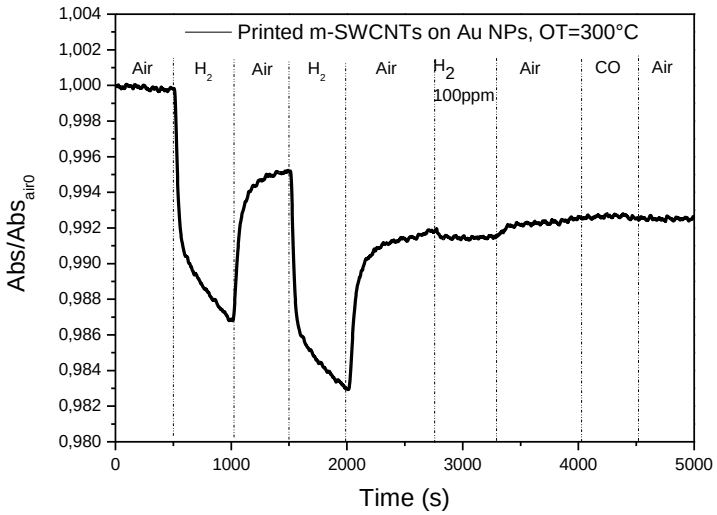

Figure 4.1.18 – Dynamic response of printed m-SWCNT deposited on Au NPs at λ = 570 nm OT=300°C.

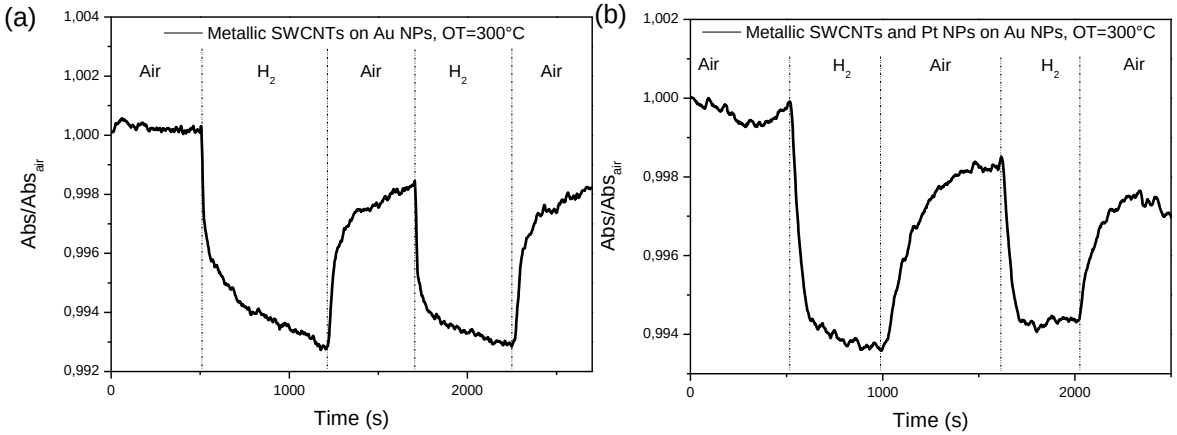

Figure 4.1.19 – Dynamic response of a) dropcasted m-SWCNT deposited on Au NPs at λ = 570 nm OT=300°C; b) dropcasted m-SWCNT and Pt NPs deposited on Au NPs at λ = 570 nm OT=300°C.

To increase the performance of the drop casted film, platinum nanoparticles (Pt NPs) were added to the sample. Pt NPs have been used with CNTs sensors because of their catalytic action toward H_2, increasing the gas sensing properties of the structures they are combined with [45] [17] .

The results of the dynamic tests of the film with Pt NPs are showed in Figure 4.1.19b. Pt nanoparticles don't lead to the expected improvement.

Both dropcasted and printed films have been proved sensitive also to H_2(100ppm), with a fast and noticeable response.

The absorbance plots of the films in air and H_2(1%) and the relative OAC plot are reported in Figure 4.1.20.

The films with metallic SWCNTs and Au NPs are characterized by a blue-shift of the LSPR peak under H_2(1%) atmosphere, as can be seen in Figure 4.1.10b and 10c. The films with semiconductive SWCNTs on Au NPs don't show such behavior.

The OAC plots of the nanocomposites of dropcasted and printed m-SWCNTs (Figure 4.1.20b and 4.1.20c) are compared to the OAC plot of Au NPs in Figure 4.1.10d.

The OAC plot of Au NPs shows that the Au NPs are responsive to H_2(1%) with a variation of absorbance higher in intensity than changes related to the films with printed and dropcasted SWCNTs.

The m-SWCNTs may mediate the interaction between the H_2 molecules and Au NPs, as happens at 150°C: with s-SWCNTs the charge transfer to Au NPs is limited and don't causes an appreciable blue-shift of the LSPR peak, m-SWCNTs transfer the electrons to Au NPs causing the blue-shift of the LSPR peak. The presence of SWCNTs film limit the direct interaction of H_2 with Au NPs, inhibiting the response mechanism based on the bare Au NPs, may act as a barrier to interaction of hydrogen molecules to gold nanoparticles.

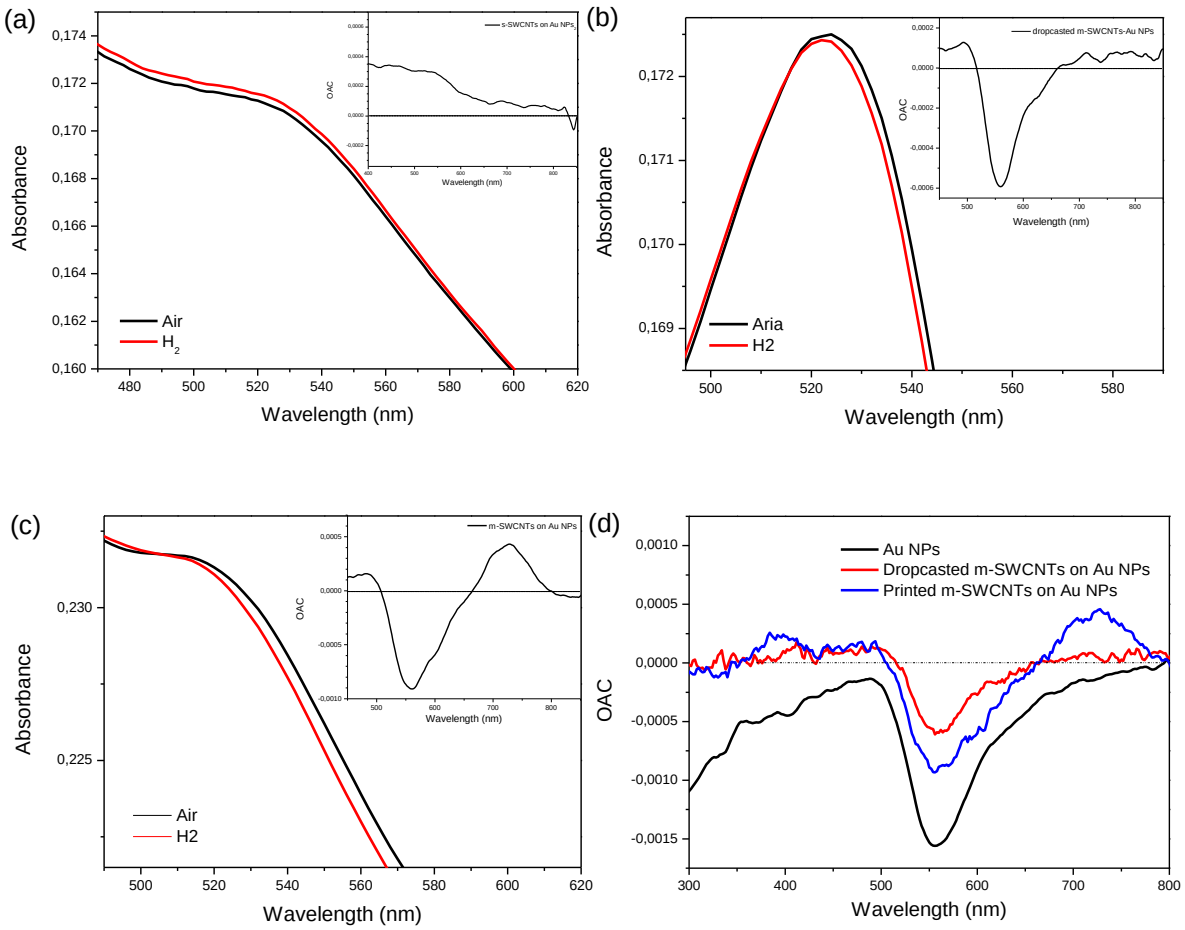

Figure 4.1.20 - Absorbance of SWCNTs on Au NPs in air and H_2(1%) at OT=300°C and for the sensors with a) dropcasted s-SWCNTs; b) dropcasted s-SWCNTs; c) printed s-SWCNTs; d) OAC plots toward H_2(1%) of printed m-SWCNTS on Au NPs, dropcasted m-SWCNTS on Au NPs and Au NPs alone.

4.1.9 Conclusions

Optical transparent SWCNTs films were obtained by ink-jet printing with good optical gas sensing properties.

The coupling between Au NPs and m-SWCNTs has been demonstrated to be essential for the devolvement of transparent optical sensor without the need of an elevated operative temperature. The s-SWCNTs displayed poor sensitivity to oxidizing/reducing gases, meanwhile the nanostructure composed of Au NPs and m-SWCNTs displayed very good performance toward hydrogen detection at 150 °C OT..

The thickness of the film plays a crucial role. The gas sensing performances of dropcasted films suffer of a limited cross section of active material to interact with the gas species, and require high operating temperatures to activate the gas sensing properties.

At 300°C the detection of H_2 of the films is enhanced in response, but the Au NPs alone are also sensitive toward $H_{2,,}$ as reported in detail in section 3.1.4.5.1.

References

[1] Tans SJ, Devoret MH, Dai H, Thess, Smalley A, Geerlicks LJ, Dekker C. A. Individual single-wall carbon nanotubes as quantum wires. Nature 1997:386:474-477..

[2] Lu JP. Elastic properties of carbon nanotubes and nanoropes. Physical Review Letters 1997;79:1297.

[3] Collins P, Bradley K, Ishigami M, Zettl A. Extreme Oxygen Sensitivity of Electronic Properties of Carbon Nanotubes. Science 2000;287:1801–1804.

[4] Dharap P, Li Z, Nagarajaiah S, Barrera EV. Nanotube film based on single-wall carbon nanotubes for strain sensing. Nanotechnology 2004;15:379-382.

[5] Zhang M, Brooks L, Chartuprayoon N, Bosze W, Choa Y, Myung N. Palladium/Single-Walled Carbon Nanotube Back-to-Back Schottky Contact-Based Hydrogen Sensors and Their Sensing Mechanism. Applied Material Interfaces 2013;6: 319–326

[6] Wang J. Carbon-nanotube based electrochemical biosensors: a review. Electroanalysis 2005;17:7-14.

[7] Zhao J, Buldum A, Han J, Lu JP. Gas molecule adsorption in carbon nanotubes and nanotube bundles. Nanotechnology 2002;13:195–200.

[8] Wu Z, Chen Z, Du X, Logan JM, Sippel J, Nikolou M, Kamaras K, Reynolds J,Tanner D, Hebard A, Rinzler A. Transparent, conductive carbon nanotube films. Science 2004;305:1273–1276.

[9] Andrews R, Jacques D, Qian D, Rantell T. Multiwall carbon nanotubes: synthesis and application. Accounts of Chemical Research 2002;35:1008-1017.

[10] Odom T, Huang J-L, Kim P, Lieber C. Atomic structure and electronic properties of single-walled carbon nanotubes. Nature 1998;391: 62-64.

[11] Wilder J, Venema LC, Rinzler AG, Smalley RE, Dekker C. Electronic structure of atomically resolved carbon nanotubes. Nature 1998;391:59-62.

[12] Frank S, Poncharal P, Wang ZL, Heer WA. Carbon nanotube quantum resistors. Science 1998;280:1744–1746.

[13] Bingham JM, Anker JN, Kreno LE, Van Duyne R. Gas sensing with high-resolution localized surface plasmon resonance spectroscopy. Journal of the American Society 2010;132: 17358–17359.

[14] Zanolli Z, Leghrib R, Felten A, Pireaux J-J, Llobet E, Charlier J-C. Gas sensing with Au-decorated carbon nanotubes. ACS Nano 2011;5:4592–4599.

[15] Khalap V, Sheps T, Kane A, Collins P. Hydrogen sensing and sensitivity of palladium-decorated single-walled carbon nanotubes with defects. Nano Letters 2010;10:896–901.

[16] Mubeen S, Zhang T, Yoo B, Deshusses M, Myung N. Palladium Nanoparticles Decorated Single-Walled Carbon Nanotube Hydrogen Sensor. Journal of Physical Chemistry C 2007;111:6321–6327.

[17] Dhall S, Jaggi N. Highly dispersed platinum sputtered multiwall carbon nanotubes based hydrogen gas sensor at room temperature. Sensors and Actuators A: Physical 2015;224:50-56.

[18] Randeniya L, Martin P, Bendavid A, McDonnell J. Ammonia sensing characteristics of carbon-nanotube yarns decorated with nanocrystalline gold. Carbon 2011;49:5265-5270.

[19] Zhao J, Buldum A, Han J, Lu JP. Gas molecule adsorption in carbon nanotubes and nanotube bundles. Nanotechnology 2002;13:195-200.

[20] Kong, Chapline, Dai. Functionalized Carbon Nanotubes for Molecular Hydrogen Sensors. Advanced Materials 2001;13:1384–1386.

[21] Star A, Joshi V, Skarupo S, Thomas D, Gabriel J-C. Gas Sensor Array Based on Metal-Decorated Carbon Nanotubes. Journal of Physical Chemistry B 2006;110:21014–21020.
[22] Dhall S, Jaggi N. Highly dispersed platinum sputtered multiwall carbon nanotubes based hydrogen gas sensor at room temperature. Sensors and Actuators A: Physical 2015;224:50–56.
[23] Quintana M, Ke X, Tendeloo G, Meneghetti M, Bittencourt C, Prato M. Light-induced selective deposition of Au nanoparticles on single-wall carbon nanotubes. ACS Nano 2010;4:6105–6113.
[24] Fan Y, Goldsmith B, Collins P. Identifying and counting point defects in carbon nanotubes. Nature Materials 2005;4:906–911.
[25] Sajed F, Rutherglen C. All-printed and transparent single walled carbon nanotube thin film transistor devices. Applied Physics Letters 2013;103:143303.
[26] Islam, Rojas, Bergey, Johnson, Yodh. High Weight Fraction Surfactant Solubilization of Single-Wall Carbon Nanotubes in Water. Nano Letters 2003;3:269–273.
[27] Kataura, Kumazawa, Maniwa, Umezu, Suzuki, Ohtsuka, Achiba Y. Optical properties of single-wall carbon nanotubes. Synthetic Metals 1999;103:2555–2558.
[28] Kauffman D, Sorescu D, Schofield D, Allen B, Jordan K, Star A. Understanding the sensor response of metal-decorated carbon nanotubes. Nano Letters 2010;10:958–963.
[29] Zhu J, Shim BS, Prima M Di, Kotov NA. Transparent conductors from carbon nanotubes LBL-assembled with polymer dopant with π-π electron transfer. Journal of the American Chemical Society 2011;133:7450–7460.
[30] Gaspera ED, Karg M, Baldauf J, Jasieniak J, Maggioni G, Martucci A. Au nanoparticle monolayers covered with sol–gel oxide thin films: optical and morphological study. Langmuir 2011;27:13739–13747.
[31] Soetedjo H, Mora M, Garcia C. Optical properties of single-wall carbon nanotube films deposited on Si/SiO2 wafers. Thin Solid Films 2010;518:3954–3959.
[32] Li J, Lu Y, Ye Q, Cinke M, Han J, Meyyappan. Carbon Nanotube Sensors for Gas and Organic Vapor Detection. Nano Letters 2003;3:929–933.
[33] Consalesa M, Campopianoa S, Cutoloa A, Penza M, Aversa P, Cassano G, Giordano M, Cusano A. Carbon nanotubes thin films fiber optic and acoustic. Sensors and Actuators B 2006;118232–242.
[34] Gaspera DE, Bersani M, Mattei G, Nguyen TL. Cooperative effect of Au and Pt inside TiO 2 matrix for optical hydrogen detection at room temperature using surface plasmon spectroscopy. Nanoscale 2012;4:5972-5979.
[35] Dettlaff-Weglikowska U, Skákalová V, Graupner R, Jhang SH, Kim BH, Lee HJ, Ley L , Park Y, Berber S, Tománek D, Roth S. Effect of SOCl2 treatment on electrical and mechanical properties of single-wall carbon nanotube networks. Journal of the American Chemical Society 2005;127:5125–5131.
[36] Lee† C, Baik‡ S, Zhang† J, Masel† R, Strano*† M. Charge Transfer from Metallic Single-Walled Carbon Nanotube Sensor Arrays. Journal of Physical Chemistry B 2006;110:11055–11061.
[37] Yang F, Yang R. Ab initio molecular orbital study of adsorption of atomic hydrogen on graphite: Carbon 2002;40:437–444.
[38] Yang F, Lachawiec A, Yang R. Adsorption of spillover hydrogen atoms on single-wall carbon nanotubes. Journal of Physical Chemistry B 2006;110:6236–6244.

[39] Browning DJ, Gerrard ML, Lakeman BJ, Mellor IM, Mortimer RJ, Turpin MC. Studies into the storage of hydrogen in carbon nanofibers: proposal of a possible reaction mechanism. Nano Letters 2002;2:201–205.
[40] Penza, Cassano, Rossi, Alvisi, Rizzo, Signore, Dikonimos T, Serra E, Giorgi R. Enhancement of sensitivity in gas chemiresistors based on carbon nanotube surface functionalized with noble metal (Au, Pt) nanoclusters. Applied Physical Letters 2007.
[41] Guo K, Jayatissa A. Hydrogen sensing properties of multi-walled carbon nanotubes. Materials Science and Engineering: C 2008;28:1556-1559.
[42] Mubeen S, Zhang T, Chartuprayoon N, Rheem Y, Mulchandani A, Myung N, Desuhusses M. Sensitive detection of H2S using gold nanoparticle decorated single-walled carbon nanotubes. Analitical Chemistry 2010;82:250–257.
[43] Yim W-L, Gong Xg, Liu Z-F. Chemisorption of NO2 on carbon nanotubes. The Journal of Physical Chemistry B 2003;107:9363–9369.
[44] Mittal M, Kumar A. Carbon nanotube (CNT) gas sensors for emissions from fossil fuel burning. Sensors and Actuators B: 2014;203:349–362.
[45] Kumar M, Ramaprabhu S. Nanostructured Pt Functionlized Multiwalled Carbon Nanotube Based Hydrogen Sensor. Journal of Physical Chemistry B 2006;110:11291-11298.

Chapter 4 - Gas sensing of carbon nanotubes-based nanostructures

4.2 Carbonaceous films as sensitive material for optical gas sensors

4.2.1 Introduction

The search for sensors relying on cheap materials and processing encourages the experimentation of new materials and new synthesis processes.

Nickel is a transition metal that possesses well-know catalytic activity[1] [2] and present a lower cost than Platinum or Palladium.

Its catalytic activity has been exploited for the production of Carbon Nanotubes (CNTs) [3] [4] and its interaction with gas species[5] [6] can be exploited for the design of new sensors[6] [7] .

Fullerene (C_{60}) and CNTs have proved to be endued with photocatalytic properties in combination with metal oxides[8] [9]. Nanostructures of carbon nanomaterial and Ni nanoparticles (Ni NPs) have been realized [10] [11] exploiting also the capability of Nickel to catalyze the synthesis of CNTs with Ni NPs particles encapsulated in CNTs[12] [13] .

The aim of this work is the study of the optical gas sensing film of CNTs with encapsulated Ni nanoparticles grown in a carbonaceous matrix of fullerenes with multistep synthesis process.

Finally, the influence of Palladium Nanoparticles (Pd NPs) has been considered on the gas sensing properties of the film. Palladium is a transition metal largely employed to confer or improve the sensitivity of nanomaterials to gaseous hydrogen[14][15].

The addition of Pd nanoparticles will be considered in terms of gas sensing performance of the composites nanostructures of fullerene and Ni NPs in CNTs.

4.2.2 Film deposition

The films were spplied by Department of Nanotechnology, Tele&Radio Research Institute from Warsaw.

The fullerenes, carbon nanotubes and metal particles were deposited in a multistep process here reported.

Step1. In the first step the Physical Vapor Deposition (PVD) of Nickel acetate and fullerite C_{60} was carried. In PVD deposition method, the parameters such as current flowing through

sources (I_{C60}, I_{Ni}), duration time (t) and the sources-substrates distances (d) affects the quality of structure and thickness of obtained films.

The parameters used are I_{C60}=1.9A and I_{Ni}=1.1 A , t =60s and d= 60mm. The sample produced with this method is referred as A. The sample produced with the same parameters except reaction period t=90s is referred as B.

Step2. Then Chemical Vapor Deposition (CVD) with Xylene followed. The feed of xylene was 0.05ml per minute and the reaction was carried at 650°C for 15 mintues under Argon flow of 0,67 liters per minute. The sample obtained are referred as A1 and B1.

Step3. Finally, a PVD deposition of Pd acetate was conducted in the same condition as Step1 for the two samples. The samples produced with this method are referred as A2 and B2.

4.2.3 Optical characterization of the films

The sample obtained with only the first step of deposition have been characterized with UV/Vis/NIR spectroscopy.

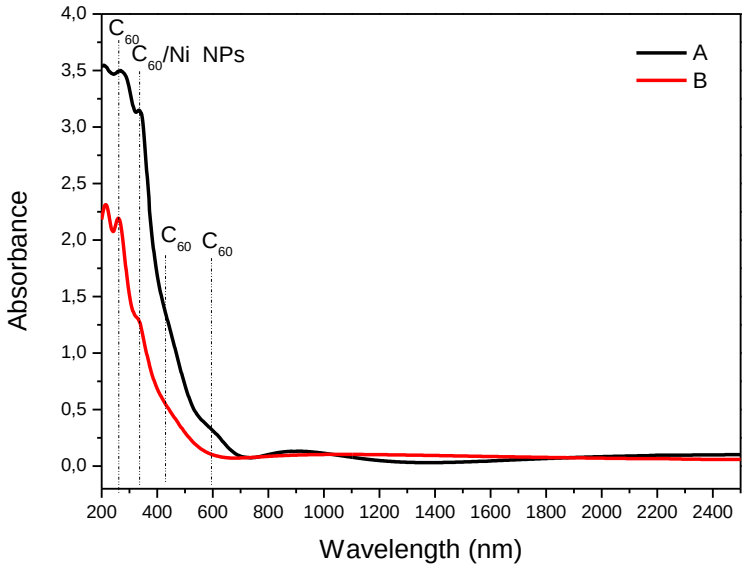

Figure 1 – Absorbance spectra of sample A and B.

The deposition of the first layer gives a thick film with high absorbance in the UV/Vis range. In the UV, the optical transitions of fullerenes at 210nm, 265nm, 350nm are related to the electronic transitions [16] and at 430nm the excitonic transition occurs[17] .

The shoulder at 350nm can be related to the LSPR of spherical Ni grains [18] .

Absorbance plot of sample A shows two broad band at 900nm and the second from 1600 till beyond 2500nm. For sample B a single broad band from 900nm to 2500nm is visible. This can be correlated to the elevated thickness of the films generating thin film interference and an estimate of the thickness to roughly 400nm can be drawn from the studies conducted on similar films in ref. [4].

The variation in optical absorbance consequent to the depositions of the layer of CNTs (A1 and B1) and the final layer of C_{60} and Pd NPs (A2 and B2) are reported in Figure 2.

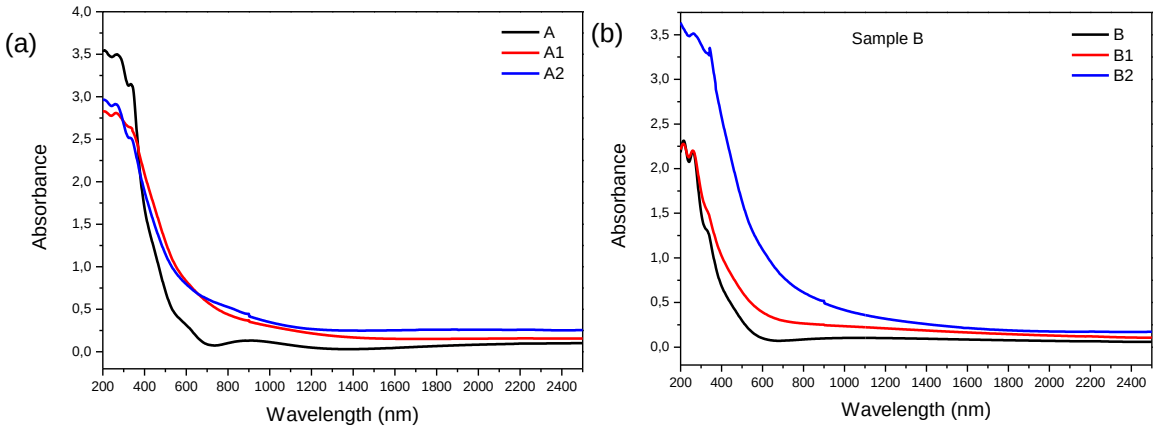

Figure 2 – a) Absorbance spectra of sample A, A1, A2. b) Absorbance spectra of sample B, B1, B2.

With the deposition of the second layer the fringes of interference disappear. The deposition of the third layer stresses the features of the fullerenes for the final film, indicating that further C_{60} is deposited during step 3 of the film production.

Pd spherical NPs have features in UV range and decaying absorbance in visible and NIR wavelengths[19], so they cannot be recognized with the spectroscopy in the range of analysis employed. No fringes of thin film interference are observed for sample A2 and B2, too.

4.2.4 Morphological characterization

The morphological characterization of the samples were carried with Scanning Electron Microscopy (SEM) after the steps of deposition 2 and 3.

The topography of the surface of the films was imaged using secondary electrons (SE) detector. Low angle backscattered electrons (LABE) detector enabled to define samples morphology by observing changes of the contrast composition. The contrast depends on the atomic number of elements of the observed microstructure.

No SEM images are present for sample A and B, but previous studies on these systems confirm the formation of a porous layer of fullerenes and no Ni particles are observed[20] .

Detail studies (in SE and LABE modes) of A1 sample showed that it is composed of short and broad nanotubes placed in carbonaceous matrix while the sample B1 contains longer and more defected nanotubes. Both the samples display high coverage of the surface with metallic grains, labeled in Fig. 3a and 3b by brighter emission electron for the higher Z than carbon.

Shapes characterized by smoother intensity can be recognized and are attributed to the CNTs. In their boundaries they show bright features of few tens of nm in size, visible in back scattered electrons SEM image, indicating that the Ni nanoparticles are incorporated in the carbon tubes.

The high temperature of the CVD process (650°C) leads to partial deterioration of the fullerenes present in the samples and to coalescence of Nickel forming the particles[4].

The SEM images of the samples A2 and B2 (respectively Figure 3c and 3d) shows that covering with palladium is accomplished and provokes the smoothing of the features of Ni NPs and CNTs visible in A1 and B1 films. The coverage with Pd grains is not as extensive as with Ni deposition. Figure3c shows large metallic particles, that may be caused by agglomeration of nanoparticles, meanwhile sample B2 shows a more homogenous distribution.

Generally, all four samples display heterogeneous size and shape distribution of the metallic particles.

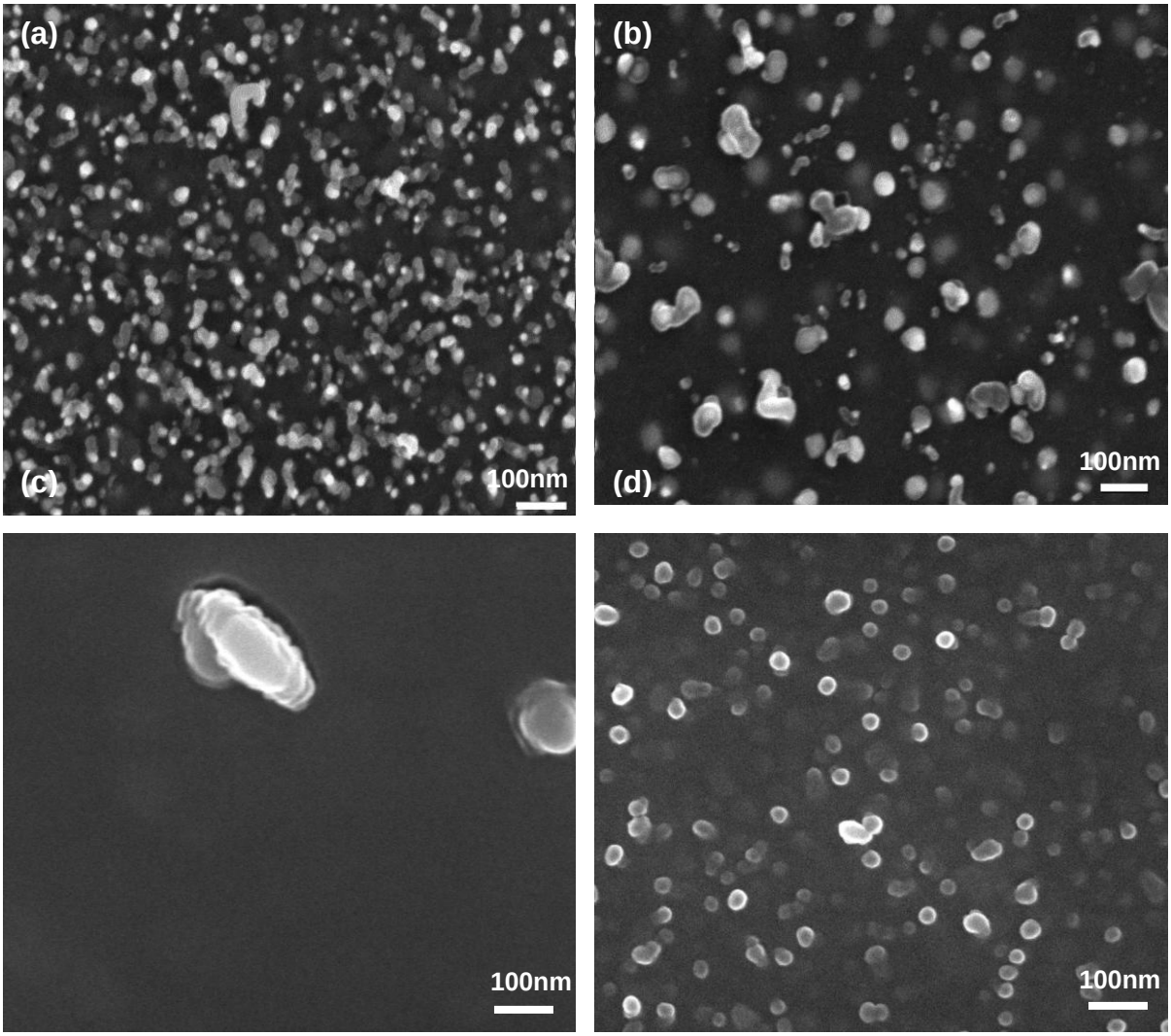

Figure 3 – SEM images of the samples a) A1; b)B1; a) A2; b)B2.

4.2.5 Gas sensing results

For all the samples it was first measured the transmittance in air and then in gas in order to determine the wavelengths at which the absorbance variation was larger. For such wavelengths, dynamic measurements have been performed in order to compare the response time for the different gases.

The films obtained after every step of deposition have been tested toward oxidizing/reducing gases. In particular, H_2(10000ppm), CO(10000ppm), NO_2(1000ppm) balanced in dry air have been used as gas target.

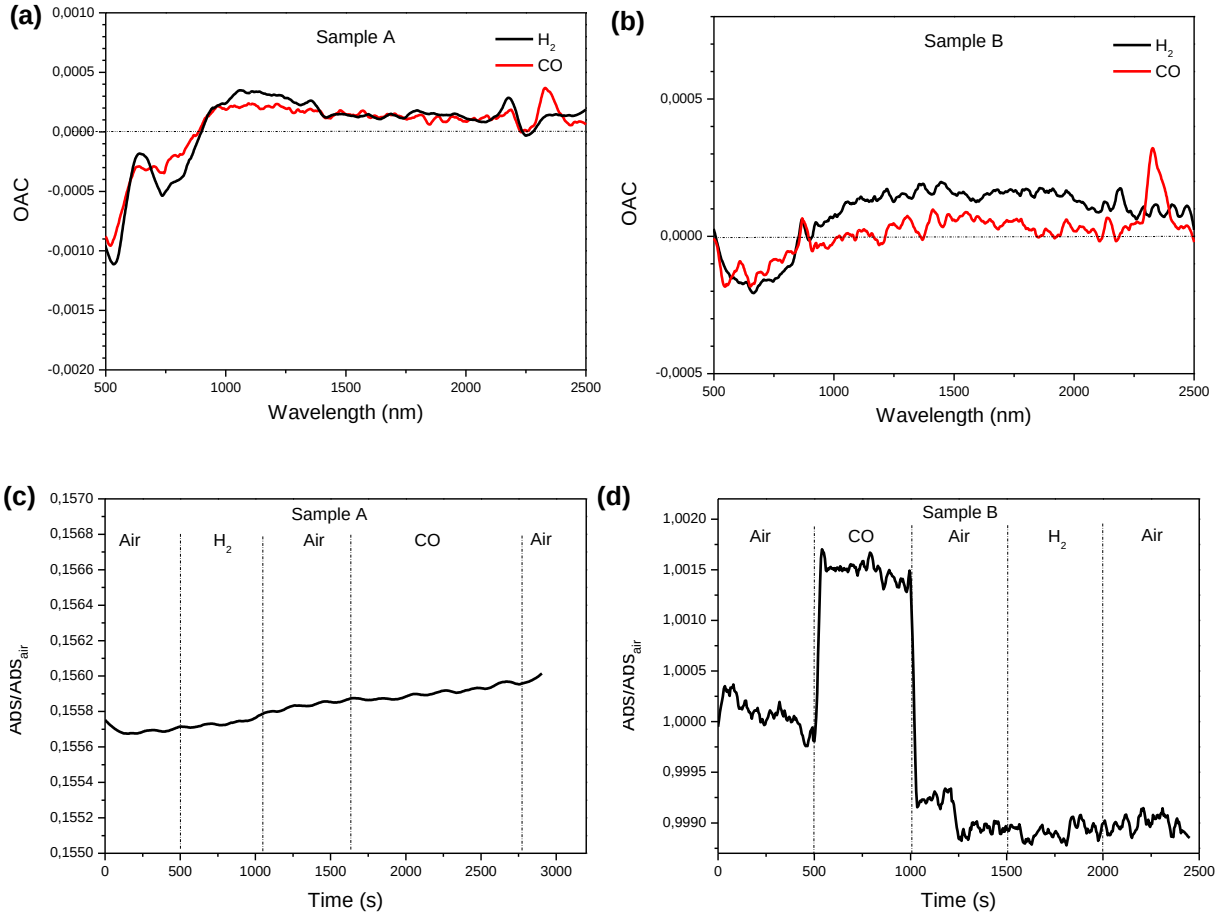

Figure 4 – OAC plots at OT=80°C of a) sample A and b) sample B; dynamic scans at OT=80°C of c)sample A at λ=750nm and d) sample B at λ=2325nm.

The samples deposited with the first step of deposition present broad peaks in the OAC plots at ~550nm and at 1100nm when exposed to H_2(1%) and CO(1%). CO shows an additional peak at 2325nm in the plots of both the films.

The increase in absorbance of the samples when exposed to reducing gases may be related to the interaction with fullerenes. The absorbance bands at 550nm is strengthened and at 1100nm have been observed in fullerene and are respectively strengthened and activated by the action of a doping agent[21] [22].

The increase in absorbance at 2325 may be related to the filling of the band gap with two bands located at ~0.5eVand ~1.3eV caused by the doping of the fullerene films[22].

The dynamic scans of sample has been run at λ=750nm, where a dip in the OAC plots appear. The samples is not sensitive to the gases at such wavelength.

Sample B is tested at λ=2325nm and proves a discrete response toward CO(1%), no variation is obtained under H_2 flow.

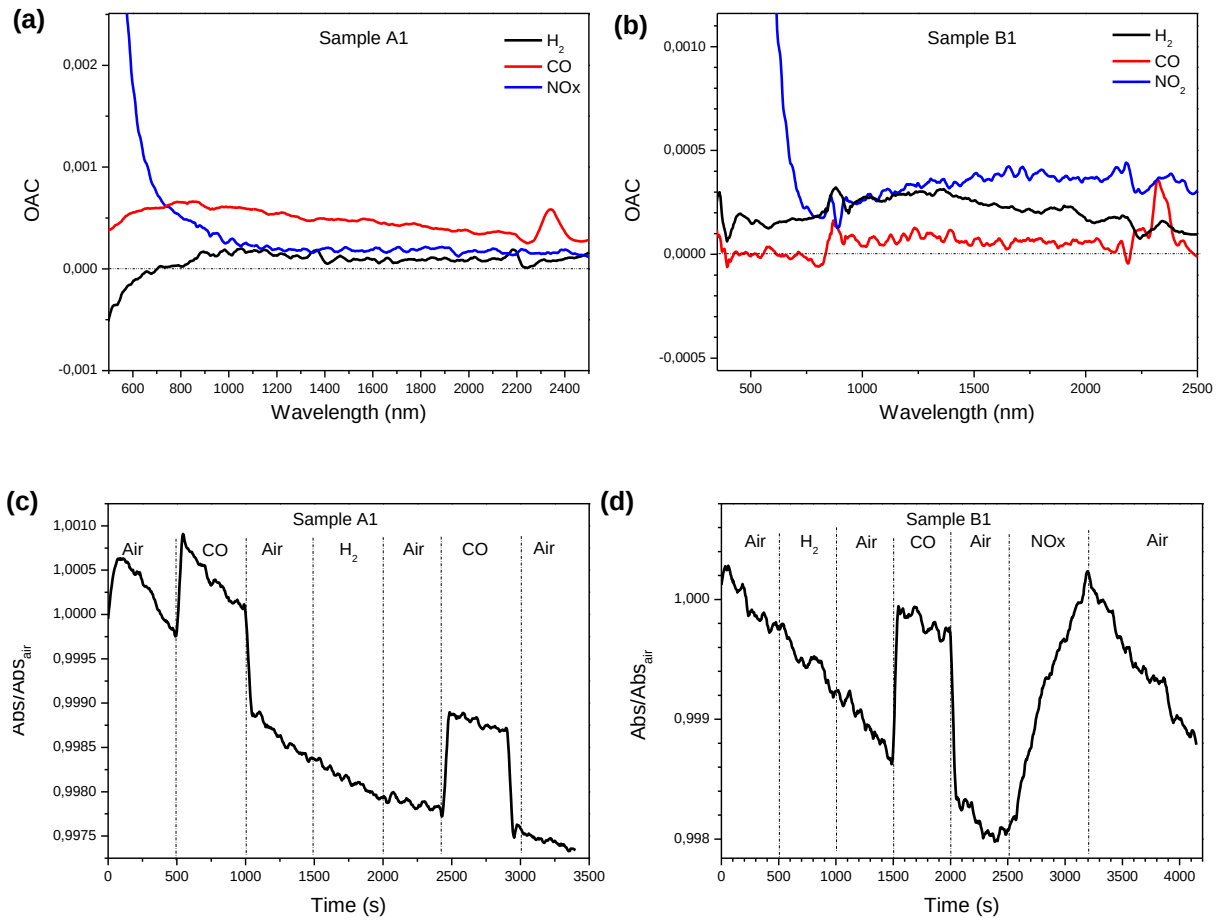

Figure 5 – OAC plots at OT=80°C of a) sample A1 and b) sample B1; dynamic scans at OT=80°C of c)sample A1 at λ=2325nm and d) sample B1 at λ=2325nm.

The gas sensing properties of the films obtained in the second step of deposition are pictured in Figure 5.

A rise in absorbance in the NIR is observed for sample B1 under exposure to the gases, in particular for H_2(1%) and NO_2(1000ppm).

The increase in absorbance can be related to the interaction of the gas molecules with carbon nanotubes.

The strong absorbance of OAC plot of NO_2 in the range of 400-700nm is caused by the characteristic absorbance properties of the gas itself.

Both the samples show a peak at λ=2325nm in CO(1%).

The dynamic test of samples B1 has been carried at λ=2325nm and exhibits the response of the film toward CO and a saw-tooth like response to NO_2(1000ppm).
The more damaged structure of CNTs in sample B1 can increase the response toward NO_2, but doesn't look effective enough to enable the dynamic response toward H_2.

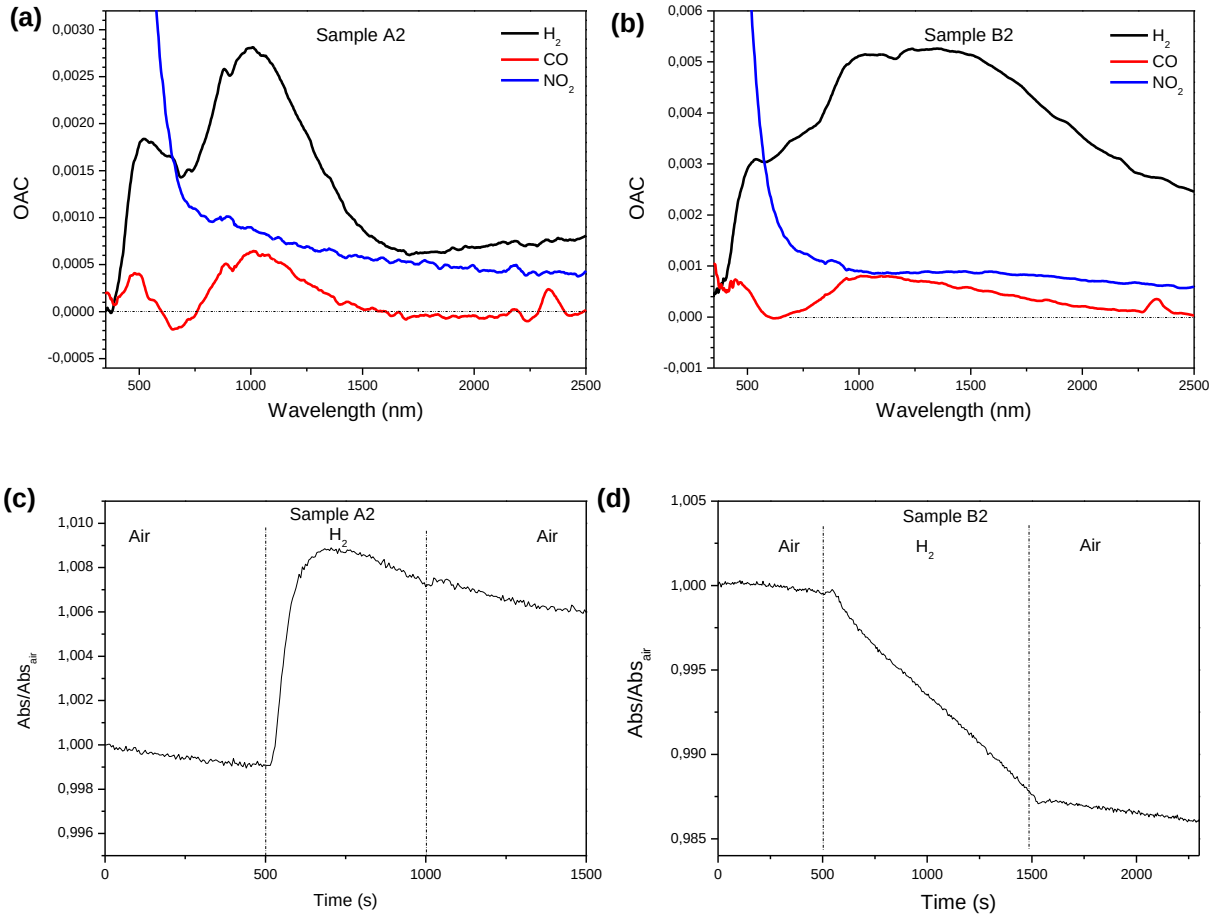

Figure 6 – OAC plots at OT=80°C of a) sample A2 and b) sample B2; dynamic scans at OT=80°C of c)sample A2 at λ=1000nm and d) sample B1 at λ=1050nm.

The final films present OAC plots similar to those obtained by the film A and B, with bands at ~500nm and ~1000nm. As expected, the response to H_2 is strongly enhanced by the presence of Pd NPs. No response was observed with CO and NO_2.
The OAC plots of samples A2 and B2 toward NO_2 are similar to the OAC of A1 and B1, implying the interaction of the gas is the same after the deposition of Pd.

Sample A2 presents a strong variation in relative absorbance in H_2(1%) atmosphere. The large size of the Pd NPs noted in Figure 3c may cause the slow recovery to H_2 observed in Figure 6c.

The reason of the opposite trend for sample B2 with a decrease in absorbance is not clear. CO and NO_2 don't lead to dynamic variations at the wavelength tested. The static variation observed for CO may be caused by the incomplete desorption 1 hour later the exposure to H_2(1%) and not be related to the variation of CO on the optical transitions of carbon nanotubes.

4.2.6 Discussion

The difference in response between samples A, B and the analogous sample A2 and B2 is related to the interaction of the gas molecules with the different nanomaterials.

The interaction of the films toward CO is already activated by fullerene and Ni NPs, but appear enhanced and extended in the IR range with the addition of carbon nanotubes and Pd NPs. The action of Pd is even stronger for H_2, as expected. Hence, Pd particles play a better catalytic effect on gas sensing properties toward H_2 than Ni NPs do, this was already observed for electrical sensors [23][24].

C_{60} is a n-type semiconductor and is subject to the formation of traps states due to interaction with the oxygen present in air[21] . H_2 and CO can remove adsorbed oxygen by chemical reaction and Ni may play a stronger catalytic action on CO[25][26], leading to the presence of the dynamic response observed in Figure 4d, 5c, 5d.

The stronger catalytic action of Nickel toward CO may lead to a n-doping effect on C60, with the appearance of absorbance bands at 2350nm and 1100nm[22].

The interaction with Pd increases the charge transfer from the gas molecules to the metal particles and then to the CNTs/C_{60} nanostructures [23][27], reflected in the emergence of absorbance bands in the NIR, due to improved electronic transitions (S11 and S22) of nanotubes and optical transition of C_{60} [28] [22].

The addition of Pd NPs in carbon matrix enhances the static optical response to H_2, but the kinetics of gas desorption and recovery appear extremely long.

NO_2 is electron-acceptor specie and the charge transfer occurs in the opposite direction, from carbon nanomaterial to Nickel particles and is finally to NO_2 molecules [7]. The oxidation action of NO_2 may cause a heavy p-doping of the carbon nanotubes with the effect

of a general increase in optical absorbance accompanied by the rise of a new peak at 1.07eV(1160nm) [29] .

4.2.7 Conclusion

A method for the production of a sensing element has been proposed and the evolution of its sensing properties has been followed.

The layer of fullerene and Ni particles prove sensitive to CO and the successive progressive stratification of the samples modifies the sensing properties of the nanostructures improving the response to the oxidizing/reducing gases.

The CNT-Ni-Pd system reveals an effective film for sensing application and the understanding of the gas sensing mechanism of the nanostructures may lead in the future to a careful design of thin films provided with finer performances in gas detection.

References

[1] Goodman DW, Kelley RD, Madey TE, Yates JT. Kinetics of the hydrogenation of CO over a single crystal nickel catalyst. Journal of Catalysis 1980;63:226–234.

[2] Yamazaki O, Tomishige K, Fujimoto K. Development of highly stable nickel catalyst for methane-steam reaction under low steam to carbon ratio 1996;136:49–56.

[3] Ren ZF. Synthesis of Large Arrays of Well-Aligned Carbon Nanotubes on Glass. Science 1998;282:1105–1107.

[4] Belka R, PBaza M, SuchaDska M, Ferrari M. Optical properties of C-Pd films prepared on silica substrate studied by UV-VIS-NIR spectroscopy. Proc of SPIE Vol 2014;9290:1–7.

[5] Blyholder G, Neff LD. Infrared study of the adsorption of methanol, ethanol, ether, and water and the interaction of carbon monoxide and hydrogen on a nickel surface Journal of Catalysis 1963;2:138–144.

[6] Lu J, Zhang X, Wu X, Dai Z, Zhang J. A Ni-Doped Carbon Nanotube Sensor for Detecting Oil-Dissolved Gases in Transformers. Sensors 2015;15:1352213532.

[7] Lü R, Shi K, Zhou W, Wang L, Tian C, Pan K, Sun L, Fu H. Highly dispersed Ni-decorated porous hollow carbon nanofibers: fabrication, characterization, and NO x gas sensors at room temperature. Journal of Materials Chemistry 2012;22:24814–24820.

[8] Zhang Y, Tang Z-R, Fu X, Xu Y-J. Engineering the Unique 2D Mat of Graphene to Achieve Graphene-TiO 2 Nanocomposite for Photocatalytic Selective Transformation: What Advantage does Graphene Have over Its Forebear Carbon Nanotube? ACS Nano 2011;5:7426–7435.

[9] Yang MQ, Zhang N, Xu YJ. Synthesis of fullerene–, carbon nanotube–, and graphene–TiO2 nanocomposite photocatalysts for selective oxidation: a comparative study. Applied Material Interfaces 2013;5:1156−1164.

[10] Vijayakrishnan V, Santra AK, Seshadri R, Nagarajan R. A comparative study of the interaction of nickel clusters with buckminsterfullerene, C 60, and graphite. Surface Science1992;262:L87–L90.

[11] Li J, Ko JW, Ko WB. Photocatalytic activities of carbon nanocapsules encircled by nickel nanoparticle composites to organic dyes degradation. Journal of Ceramic Processing Research 2015;16 :457-461.

[12] Mel EA, Gautron E, Angleraud B, Granier A. Synthesis of nickel-filled carbon nanotubes at 350° C. Carbon 2011;49:4595–4598.

[13] Pradhan BK, Kyotani T, Tomita A. Nickel nanowires of 4 nm diameter in the cavity of carbon nanotubes. Chemical Communications 1999:1317–1318.

[14] Mubeen S, Zhang T, Yoo B, Deshusses M, Myung N. Palladium Nanoparticles Decorated Single-Walled Carbon Nanotube Hydrogen Sensor. Journal of Physical Chemistry 2007;111:6321–6327.

[15] Favier F, Walter EC, Zach MP, Benter T, Penner RM. Hydrogen sensors and switches from electrodeposited palladium mesowire arrays. Science 2001;293:2227–2231.

[16] Zhang K, Zhang Y, Wang S. Enhancing thermoelectric properties of organic composites through hierarchical nanostructures. Scientific Reports 2013;3:1–7.

[17] Makarova TL, Sundqvist B, Scharff P, Gaevski ME, Olsson E, Davydov VA, et al. Electrical properties of two-dimensional fullerene matrices. Carbon 2001;39:2203–2209.

[18] Yeshchenko OA, Dmitruk IM, Alexeenko AA, Dmytruk AM. Optical properties of sol–gel fabricated Ni/SiO 2 glass nanocomposites. Journal of Physics and Chemistry of Solids 2008;69:1615–1622.

[19] Langhammer* C, Yuan Z, Zorić I, Kasemo B. Plasmonic Properties of Supported Pt and Pd Nanostructures. Nano Letters 2006;6:833–838.
[20] Czerwosz E, Dłużewski P, Nowakowski R, Wronka H. Topography and structure of C60/C70+Ni film containing carbon nanotubes grown perpendicularly to the substrate. Vacuum 1999;54:57–62.
[21] Saran R, Stolojan V, Curry RJ. Ultrahigh Performance C60 Nanorod Large Area Flexible Photoconductor Devices via Ultralow Organic and Inorganic Photodoping. Scientific Reports 2014;4:5041
[22] Sohmen E, Fink J, Krätschmer W. Electronic structure studies of undoped and n-type doped fullerene C60 1992;17 :51–55.
[23] Lin T-C, Huang B-R. Palladium nanoparticles modified carbon nanotube/nickel composite rods (Pd/CNT/Ni) for hydrogen sensing. Sensors and Actuators B: Chemical 2012;162:108–113.
[24] García-Aguilar J, Miguel-García I, Berenguer-Murcia Á, Cazorla-Amorós D. Single wall carbon nanotubes loaded with Pd and NiPd nanoparticles for H2 sensing at room temperature. Carbon 2014;66:599611.
[25] Lauterbach J, Wittmann M, Küppers J. Adsorption of CO at Ni (100) surfaces: a FTIRAS-TDS study 1992;279:287–296.
[26] Conrad H, Ertl G, Küppers J, Latta EE. Adsorption of CO on clean and oxygen covered Ni (111) surfaces 1976;57:475–484.
[27] Kong J, Chapline MG, Dai H. Functionalized Carbon Nanotubes for Molecular Hydrogen Sensors. Advanced Materials 2001;13:1384–1386.
[28] Kauffman D, Sorescu D, Schofield D, Allen B, Jordan K, Star A. Understanding the sensor response of metal-decorated carbon nanotubes. Nano Letters 2010;10:958–63.
[29] Kazaoui S, Minami N, Jacquemin R, Kataura H. Amphoteric doping of single-wall carbon-nanotube thin films as probed by optical absorption spectroscopy. Physical Review B 1999;60:13339–1342.

Chapter 5 - Conclusions

In the following, a general comprehensive look is taken on the data and results discussed so far. The scope of this doctoral project is the study of gas sensing properties of carbon nanomaterial through the production of thin films and the monitoring of their optical properties when exposed to dangerous gas species

The work is divided in two main chapters. In the first part, optical sensors based on graphene oxide are evaluated. In section 3.1, the influence of the chemical structure of graphene oxide is related to the gas sensing properties of the material. The GO is coupled with Au NPs as optical probe and is progressively reduced in H_2(5%v/v Argon) in cycles of reduction of 15', 30', 45' at 150°c, 250°C, 350°C and 500°C. An appreciable reduction of the structure is obtained with a recovery of the sp^2 lattice at 350°C. The treatments at 500°C don't lead to a remarkable variation in structure than the treatments at 350°C. The GO don't display sensing properties and the reducing treatments are fundamental to activate the response to the gases. The increase in reduction enhances the performances toward H_2(1%) and lower the limit of detection allowing the detection of H_2(100ppm).Weak response to CO and NO_2 is observed with a mild reduction, leading to a partial recovery of the graphitic lattice, but with consistent presence of oxidized groups, yet. The sensors were responsive at 150°C and 300°C. The higher OT leads to faster and sharper sensing performance toward H_2. However, the Au NPs play an active role as sensing elements above 250°C and the response to the H_2 may be not caused by the interaction of the gas with the only rGO layer.

In section 3.2, GO is chemically reduced with excess of PPD in a solution of water and ethanol. The FTIR spectroscopy confirms the reduction of the material and suggests the grafting of dimers/oligomers of PPD on the sheets of chemically modified graphene (CMG). The synthesis at high temperature with minor concentration of PPD, respectively 95°C and weight ratio GO:PPD of 1:0.3 don't appear reproducible, with different chemical structures of the reaction products.

CMG was tested at room temperature alone and with Au NPs. The material alone shows promising results toward NH_3, thanks to the interaction of the gas molecules with the grafted PPD oligomers. The CMG coupled with Au NPs displays a variation in absorbance also toward CO, suggesting the versatility of this material for optical gas sensing.

In Chapter 4 the attention is directed to the optical gas sensing properties nanocomposites of CNTs. In 4.1 a systematic study is conducted to evaluate the differences in optical gas

sensing of MWCNTs, metallic SWCNTs, semiconductive SWCNTs. Thin films of CNTs have been produced by ink-jet printing and dropcasting on bare silica and Au NPs monolayer on silica substrates. The samples were prepared in collaboration with the group of prof. Kos Galatsis in UCLA.

The two deposition techniques produced films with different thickness that have been tested at 150°C and 300°C as optical sensor. The film deposited by dropcasting presents low thickness, which hinders the gas sensing properties of the nanostructures. As a consequence, the best results are achieved with the printed films. At 150°C OT, the gas sensing properties of CNTs are activated by Au NPs through a synergic behavior with CNTs and in particular with the metallic SWCNTs. These last exhibit the best results toward H_2. Also the film composed of semiconductive SWCNTs on Au NPs showed to be responsive toward H_2. The rise in operating temperature to 300°C leads to an increase in gas sensing performance in terms of time and variation of analysis property for metallic SWCNTs.

The films were produced in three consecutive steps allowing to distinguish the effect of the different nanomaterials. The detection of CO is preserved after each steps of deposition and has been related to the interaction of the gas molecules with fullerenes and Ni nanoparticles. Besides to CO, Ni@CNTs in fullerene matrix are sensitive to NO_2. The last step of the production of the films trigger the sensing response of the film toward H_2, with the deposition of Pd NPs in fullerene matrix.

The optical gas sensing mechanism of the materials used have been investigated and this work may be a valuable starting point for the implementation of the nanocomposites in commercial sensor devices.

The optical properties of GO and CNTs and the low thickness of the films confer high transparency to the deposited films. The development of transparent sensors may lead to the development of non-invasive sensors integrated on transparent surfaces.

Concluding, different functionalization of GO and CNTs have been conducted and they showed the possibility of tuning the sensing properties of the carbon nanomaterials. This work has considered just a small part of the wide range of possibilities of the physical and chemical functionalization for both CNTs and GO and future work may explore further this argument, leading to a deeper knowledge and comprehension of the gas sensing properties of these nanomaterials.

Appendix: Materials and Methods

A.1 Instrumentation

A.1.1 X-Ray diffraction

The crystalline phases of the thin films were characterized by X-Ray diffraction (XRD) using a Philips PW1710 diffractometer equipped with grazing incidence X-Ray optics. The analyses were performed at 0.5° incidence, using CuKα Ni filtered radiation at 30 kV and 40 mA. The thin films were deposited on Silicon substrates for this type of investigation.
The average crystallite size Δw, as calculated from the Scherrer equation:

$$D = \frac{K\lambda}{cos\theta \Delta \mathrm{w}}$$

after fitting the experimental profiles with Lorentzian functions: in this relationship, λ=1.54 Å is the Cu kα wavelength, θ the diffraction angle, Δw the full width at half maximum (FWHM) of the diffraction peak, and K=0.9 is the shape factor.

A.1.2 Electron Microscopy

Scanning Electron Microscope (SEM) was used to evaluate the surface morphology of the nanocomposites using different microscopes: low resolution images were taken on a Philips SEM equipped with Energy Dispersive X-ray (EDX) spectroscopy for elemental analysis. High resolution images were taken on a JSM-7500F Field Emission Scanning Electron Microscope (SEM) at 2kV and on a xT Nova NanoLab SEM operating at 5kV and 0.4nA.
Transmission Electron Microscopy (TEM) analysis on films deposited from colloidal solutions deposited on carbon-coated copper grids were performed with a JEOL 100keV system.

A.1.3 Spectroscopic Ellipsometry

Ellipsometry quantities Ψ and Δ have been measured using a J.A. Woollam V-VASE Spectroscopic Ellipsometer in vertical configuration, at two different angles of incidence (60°, 70°) in the wavelength range 300-1700 nm. Optical constants n and k of CNTs film

have been evaluated from Ψ, Δ and transmittance data using WVASE32 ellipsometry data analysis software, fitting the experimental data with Cauchy dispersion.

A.1.5 X-ray photoelectron spectroscopy

The surface composition of thin films deposited on a Si wafer was analyzed by X-ray Photoelectron Spectroscopy (XPS) using a modified VG ESCALAB MK II (Vacuum generators, Hastings, England) where a twin (Mg/Al) anode x-ray source, a sputter gun, and a hemispherical electrostatic analyzer with a five channel detector are mounted. The XPS data reported were obtained using Al-Kα radiation (1486.6 eV) as an excitation source.

A.1.6 Atomic Force Microscopy

Atomic Force Microscopy (AFM) was exploited to investigate the thickness and morphology of the samples. The measures were acquired with a Veeco Digital D5000 with a silicon tip in air.

The recorded images were analyzed using Gwyddion 2.41 image analysis software.

A.1.7 Optical Spectroscopy

Optical absorption spectra of samples were measured in the 200-900 nm range using a Jasco V-570 spectrophotometer. UV-Vis-NIR absorption spectra were taken using a JASCO V-570 spectrometer.

Absorption measurements of liquid samples was performed with quartz cuvettes (1 cm optical path), while thin films on quartz substrates were analyzed placing the substrate perpendicularly to the light beam.

Fourier transform infrared spectroscopy (FTIR) measurementshave been performed in the 400–4000 cm^{-1} range using a Jasco FTIR 6300 instrument using a resolution of $4cm^{-1}$ on thin films deposited on a silicon substrate.

A.2 Materials Recipes

A.2.1 Recipe for the synthesis of 15 nm Au nanoparticles

280 mg trisodium citrate in 24 ml Milli-Q water preheated at 70 °C was quickly added to a 400 mL boiling aqueous solution containing 80 mg $HAuCl_4$. After the solution turned red-

wine colored, it was stirred at boiling point for an additional 15 minutes and then was cooled down to room temperature.

If the particles were to be redispersed in ethanol, PVP-10K was dissolved in water (200 mg in 4 mL) and this solution was mixed with aqueous gold colloids under constant stirring. After 2 hours the solution was concentrated in a rotary evaporator to about 100- 150 mL and Au NPs were precipitated with excess acetone, centrifuged at 4000 rpm for 5 minutes and re-dispersed in ethanol leading to a 30 mM concentrated solution.

A.2.6 Recipe for the synthesis of 10 nm Pt nanoparticles

In a typical synthesis, 67 mg of H_2 $PtCl_6$ and 18.7 mg of NaCl were dissolved in 3 mL ethylene glycol, degassed and kept under inert atmosphere (nitrogen). Separately, 150 mg NaNO3 and 55 mg PVP were dissolved into 13 mL ethylene glycol, degassed, and brought at 160 °C under intert atmosphere. After 20 minutes, the former solution was quickly injected into the latter: a change in color from pale orange to black was observed within few minutes. The Pt colloidal solution was kept at 160 °C under nitrogen for 30 minutes, then cooled down to room temperature, precipitated 168 with excess acetone, centrifuged at 4000 rpm for 5 minutes and redispersed in ethanol leading to a 30 mM nominal concentration.

A.2.7 Recipe for the synthesis of 15 nm Ag nanoparticles nanoparticles

In a typical synthesis 17mg of AgNO3 were dissolved in 100ml of ethanol. Two solutions of 103mg of aminopenthanol in 25ml of ethanol and of 100mg PVP in 25ml of ethanol are poured in the solution of $AgNO_3$. After homogenization, the solution is progressively heated to the boiling point. After the solution becomes bright yellow, the reaction is quenched by cooling down to room temperature.

A.2.8 Recipe for the synthesis of GO

0.5g of graphite flakes were mixed with 3g of $KMnO_4$ in a round flask in ice-cold bath, resulting in a dark green powder.

Then,30ml of concentrated H_2SO_4 (98%) were slowly added in the flask. The solution is stirred in ice-cold solution and turns dark red after 40minutes.

After a good homogenization of the solution, in 2,5h the temperature of the solution is raised to 40°C.

After 24h and the material in the round bottom flask is a dark brown paste-like compound, the reaction is quenched by dilution. At first,60ml of water are added slowly in 25minutes, than a solution 5ml H_2O_2 (30%) in 70ml water is added to the batch, causing a change in color from dark brown to yellow.

Batch is transferred to a becher and twice the volume of water is added and the compound is sedimented night long, and the separation of a water phase on the top and a slurry on the bottom takes place. The top is removed and slurry of GO goes toward purification.

The solution is washed with HCl(37%) in water in ratio 1:9 and centrifugated to remove the metal ions. GO was then further centrifugated with water till pH 7 was reached.

A.2.9 Recipe for the synthesis of CMG

A solution of 10ml of 3mg/ml of para-Phenylene Diamine in ethanol is added to a solution of 10ml of 1mg/ml of GO in water. The resulting solution is kept at room temperature under stirring and the reaction occurs in 24 hours.

The CMG is purified by mild sonication and centrifugation at 4000rpm for 1h. This treatment was reapeated till the removal of adsorbed para-Phenylene Diamine was achieved.

The CMG is dispersed in ethanol in a solution of 0,3 mg/ml.

A.2.14 Recipe for the synthesis of Au NPs monolayers

Au monolayers have been prepared on fused silica slides. The substrate was first functionalized with (3-aminopropyl) trimethoxysilane (APTMS) via immersion into a solution composed of 0.3 mL APTMS in 30 mL toluene at 60 °C for 5 minutes in a controlled environment (R.H. < 20 %). Alternatively to APTMS, 1ml of 3-amminopropyl triethoxysilane (APTES) in 30ml of benzene solution can be employed.

Substrates were then extracted and immediately washed thoroughly with fresh toluene, dried in a nitrogen stream and then placed on a hot plate at 70 °C for 5 minute to remove adsorbed toluene molecules. These substrates were used within the day, in order to prevent amines oxidation.

Au NPs monolayer was obtained by spincoating of a solution 30mM of Au NPs PVP capped on the substrates functionalized as described above. The parameter of deposition used are

3000rpm and 30s. The substrates were than stabilized at 100 °C for 15 minutes, and subsequently used as substrates themselves.

A.2.15 Recipe for preparation of dropcasted CNT films

The preparation strategy for the CNTs layer is given in Figure 1. The substrates were first functionalized with Poly-L-Lysine. A solution 0.1%(w/v) of Poly-L-Lysine is dropcasted on the substrate and kept 10 minutes to sediment on the surface. Then, the substrate is washed with distilled water and dried with air. After that the CNTs solution is dropcasted on the substrate and the sedimentation occurs in a closed box with a water supply to avoid the drying of the SWCNTs solution. The period of deposition ranges from 3 to 24h according to the desired thickness. Then, the exceeding liquid is removed by washing with distillated water and the sample is dried.

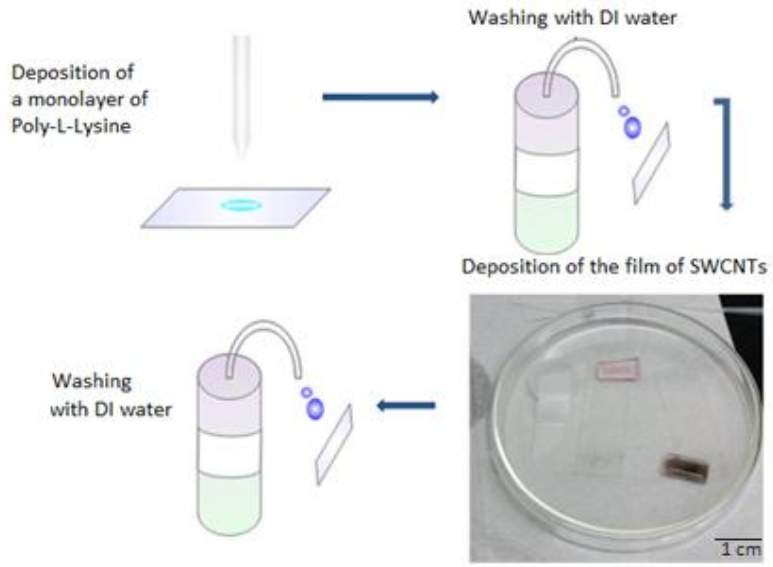

Figure A.1 - Deposition procedure with dropcasting technique.

A.3 Gas sensing set up

Optical gas sensing tests were performed by conducting optical absorption measurements in the 200-900 nm and in the 200-2500nm wavelength ranges on films deposited on SiO_2 substrates using a Harrick gas flow cell (with 5.5 cm path length) coupled with a Jasco V-650 and Jasco V-570 spectrophotometers used respectively for tests in UV/Vis and

UV/Vis/NIR range. The tests conducted in the UV/Vis/NIR range were performed with a spectrophotometer. Different operating temperature profiles have used (OT) ranging from 20°C to 300°C. The sensor was tested for both reducing and oxidant gases, (H_2, CO, NO_2) all balanced with synthetic air, with a flow rate of 0.4 L/min. In particular, the concentration of H_2 was set at 10000 and 100 ppm; the concentration of CO was set at 10000 ppm; the concentration of NO_2 was set at 1000ppm for the tests in the NIR range and at 1 ppm order to minimize the effects related to its optical absorption in the visible range. Tests with the aromatic Volatile Organic Compounds (benzene, toluene, xylene) in concentration of 10000ppm in nitrogen carrier have been also conducted.

The substrate size was approximately 1 × 2 cm and the incident spectrophotometer beam was normal to the film surface and covered a 9 × 1.5 mm area of the film.

The time spent by the sensor on achieving 90% of the total absorbance change is defined as the response time in the case of gas adsorption or as the recovery time in the case of gas desorption.

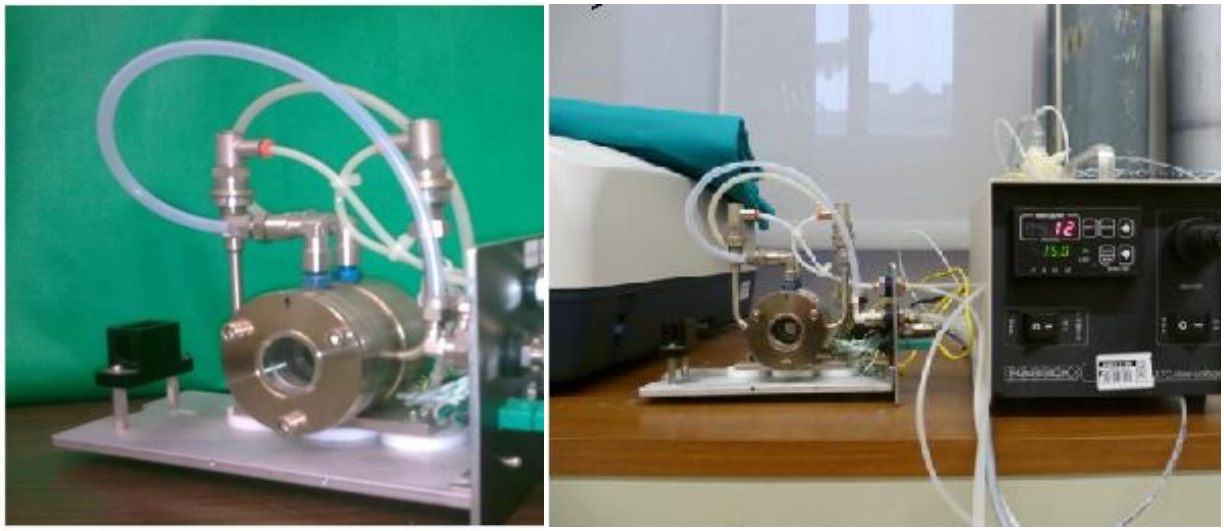

Figure A2 – Pictures of the set up employed for optical gas sensing.